

# Modeling of diffraction patterns based on microstructural properties

**Gábor Ribárik**

Physics Doctorate School  
School Leader: Prof. Zalán Horváth

Material Science and Solid State Physics Program  
Program Leader: Prof. János Lendvai

Eötvös Loránd University  
Institute of Physics  
Department of Materials Physics

Adviser:  
**Prof. Tamás Ungár, DSc**

Ph.D. Thesis  
2008.

# Contents

<b>1</b>	<b>Introduction</b>	<b>1</b>
<b>2</b>	<b>Theoretical aspects of X-ray line broadening</b>	<b>4</b>
2.1	Line profile parameters . . . . .	4
2.2	Size broadening of diffraction profiles . . . . .	5
2.2.1	Size parameters . . . . .	5
2.2.2	Size distribution functions . . . . .	8
2.2.3	Determination of the size profile [S1, S4, S6] . . . . .	10
2.2.4	Anisotropic size broadening [S1, S4, S6] . . . . .	15
2.3	Strain broadening . . . . .	18
2.3.1	The Krivoglaz–Wilkins model of dislocations . . . . .	20
2.3.2	Strain anisotropy: the concept of contrast factors . . . . .	25
2.3.3	The Groma-Csikor strain function . . . . .	27
2.4	Planar faults [S18] . . . . .	29
<b>3</b>	<b>The classical methods of X-ray line profile analysis</b>	<b>31</b>
3.1	Breadth methods . . . . .	31
3.2	Fourier methods . . . . .	35
3.3	Full profile fitting methods . . . . .	38
3.4	Pattern fitting methods . . . . .	38
3.5	Methods analysing the moments of the profiles . . . . .	39
<b>4</b>	<b>Determining microstructure by the Multiple Whole Profile fitting method</b>	<b>42</b>
4.1	The MWP method [S4, S6] . . . . .	42
4.1.1	The principles of the method . . . . .	42
4.1.2	Data preparation: profile separation using the MKDAT program . . . . .	42
4.1.3	Data preparation: instrumental deconvolution using the MKDAT program . . . . .	43
4.1.4	Evaluation of X-ray diffraction profiles using the MWP program . . . . .	44
4.1.5	The steps of the MWP evaluation procedure . . . . .	45
4.1.6	The MWP frontend . . . . .	47
4.2	MWP application to deformed Cu [S4, S6] and ball milled PbS [S9] . . . . .	48
4.3	MWP application to Al-Mg alloys [S13, S14] . . . . .	51

4.4	MWP application to Ti [S12, S21] and Si <sub>3</sub> N <sub>4</sub> [S1, S6] . . . . .	54
4.5	MWP evaluation of carbon black samples by assuming ellipsoidal crystallite shape [S4, S5, S6, S8] . . . . .	57
<b>5</b>	<b>Determining microstructure by the Convolutional Multiple Whole Profile fitting method</b>	<b>58</b>
5.1	The CMWP method [S14] . . . . .	58
5.1.1	The principles of the method . . . . .	58
5.1.2	The JAVA frontend of CMWP . . . . .	60
5.1.3	The WEB frontend of CMWP . . . . .	63
5.1.4	The CMWP evaluation procedure . . . . .	64
5.1.5	Determining the background . . . . .	65
5.1.6	Sampling of the Fourier transforms . . . . .	67
5.1.7	Sampling of the intensity patterns . . . . .	68
5.1.8	The profile cutting parameter . . . . .	69
5.1.9	Instrumental profiles . . . . .	69
5.1.10	Weighting algorithms . . . . .	71
5.1.11	Interpretation of the errors of the fitting parameters . . . . .	71
5.1.12	Convergence and numerical stability . . . . .	72
5.2	Modeling asymmetric diffraction profiles . . . . .	75
5.3	CMWP application to Al-Mg alloys [S14, S16] . . . . .	77
5.4	CMWP application to nanocrystalline Cu containing planar faults [S18] . . . . .	79
5.5	CMWP application to ball milled fluorides [S17] . . . . .	79
5.5.1	The interference effect . . . . .	81
5.5.2	Correcting for the interference effect . . . . .	86
5.5.3	The microstructure of the fluorides . . . . .	89
<b>6</b>	<b>Summary and Conclusions</b>	<b>93</b>
	<b>Own Publications</b>	<b>96</b>
	<b>Bibliography</b>	<b>99</b>

# Chapter 1

## Introduction

Macroscopic properties of materials are strongly affected by the microstructure. Microstructure, on the other hand, is a complex feature with very different aspects which often depend even on the method of investigation. The most common and most effective microstructure testing is based on electron probing. Transmission electron microscopy (TEM) provides direct images of the microstructure of almost any kind of materials including hard crystalline, hard amorphous or soft materials. Scanning electron microscopy (SEM) can test bulk materials, however, only the surface or surface near regions. The focussed ion beam (FIB) technology combined with SEM and TEM offers new perspectives for extremely sophisticated microstructure testing opportunities. Still, there are numerous important features, especially residual internal stresses, microstresses, or different kinds of size distributions which easily escape the observation facilities of electron microscopy methods. X-ray line broadening was one of the first promising methods of microstructure testing, long before electron microscopy, emerged in the early twenties. However, the first promising results faded away when it turned out that experimental uncertainties and interpretation difficulties did not allow straightforward conclusions. As a result, in the sixties and seventies electron microscopy was thought to be the only reliable method for characterising the microstructure and X-ray line profile analysis was almost forgotten. From the seventies onward, the appearance of dedicated synchrotron X-ray sources, better laboratory X-ray generators, improved X-ray detectors and new, more appropriate fundamental theories of diffraction by crystals containing defects, gave a new impetus to X-ray line profile analysis. Today, the fast computer technology and greatly enhanced experimental possibilities brought back X-ray line profile analysis as one of the most effective alternative methods to electron microscopy for the characterisation of the microstructure of crystalline materials. The aim of the present dissertation is to provide a comprehensive summary of the theoretical considerations, experimental and numerical methods which were developed for the evaluation of X-ray diffraction patterns in terms of dislocation density, dislocation character, crystalite size and size distributions, and planar defects (especially stacking fault and twin boundary frequency). A computer software package has been developed which allows to evaluate different diffraction patterns measured on different crystalline materials: powders, bulk polycrystals, single crystalline samples or textured specimens. The different parts of the software package offer different ways of the evaluation which can be optimally adapted to the particular

problem. For example, in the case of single crystals, the individual diffraction profiles of different Bragg reflections can be analysed in terms of individual dislocation contrast (or orientation) factors. Or, in the case of an ideally random powder specimen, the whole measured powder pattern can be evaluated with the same philosophy as the structure refinement by the Rietveld method. In this case the whole measured pattern is fitted by a theoretically constructed diffraction pattern which is expressed in terms of dislocation structures by average dislocation contrast factors and a crystallite size distribution function. In the entire software package the evaluation is based on microstructural models in which strain is assumed to be caused by dislocations, size broadening is caused by coherently scattering domains and planar defects are included on the basis of simulated diffraction profiles. The software package was applied successfully to more than a dozen cases of completely different materials which have been evaluated for the microstructure, cf. [S1-S23]. The most important facilities provided by the software package are the following.

- (i) It allows the fitting of the separated diffraction profiles or their Fourier transforms by theoretical intensity profiles or Fourier coefficients calculated for the concomitant size and strain effect (where strain is considered to be produced by dislocations). This part of the package is the Multiple Whole Profile (MWP) fitting procedure [S4, S6]. The dislocation densities, the character of dislocations and the subgrain size distribution in copper deformed by equal channel angular pressing (ECAP) [S4, S6] and ball milled PbS (galena) [S9] was evaluated by the MWP procedure. Shape anisotropy in carbon-black [S4, S5, S6, S8] and crystallite size distribution and the dislocation density in hexagonal  $\text{Si}_3\text{N}_4$  were also evaluated by the MWP method [S1].
- (ii) Measured diffraction patterns can be fitted by numerically constructed diffraction patterns in which the size and strain effects are theoretically calculated and can be convoluted with the measured instrumental profiles. In this procedure all the different profile functions, i.e. the size, the strain and the instrumental profiles are convoluted, therefore the method is called: Convolutional Multiple Whole Profile (CMWP) fitting procedure [S14].
- (iii) In both, the MWP and CMWP methods, the strain profiles can either be scaled by average dislocation contrast factors,  $\bar{C}$ , or by individual dislocation contrast factors,  $C_{hkl}$ . Former corresponds to the case when averaging over the permutations of the  $hkl$  indices is appropriate, whereas latter applies when the specimen is either a single crystal or strongly textured. When strain anisotropy is treated by using the individual dislocation contrast factors, it means that the strain part of each diffraction profile is scaled by a separate individual scaling parameter.
- (iv) Balogh and coworkers have systematically analysed the effect of planar defects in cubic [S18] and hexagonal crystals (Balogh et al., 2008). It was found that the planar faults profile can be given as the linear combination of a delta function and one or more Lorentzian functions. The systematic analysis provides the correlation between the planar fault densities and the different parameters of the Lorentzian functions. The profile functions and the parameter files were incorporated into the CMWP method [S18].

In a mechanically alloyed Al base Al-Mg alloys the subgrain size distribution, or coherently scattering domain size distribution and the dislocation densities and character were determined by the CMWP method [S14]. These microstructural parameters were evaluated and analysed as a function of the Mg concentration. The diffraction patterns were also evaluated by the MWP method. The results provided by the MWP and CMWP methods are critically discussed (see in section 5.3).

The diffraction patterns of different ball milled states of the  $\text{CaF}_2$ ,  $\text{SrF}_2$ ,  $\text{BaF}_2$  and  $\text{CdF}_2$  fluorides have been analysed by the CMWP procedure in terms of dislocation densities and types, and crystallite size and size distributions [S17]. An unusual X-ray optical interference effect of line broadening, similar to what was observed earlier by Rafaja et al. (2004) is found in particular states of the ball milled fluorides. The interference effect has been successfully corrected (see in section 5.5).

# Chapter 2

## Theoretical aspects of X-ray line broadening

In this chapter the different fundamental theoretical models of size and strain broadening and planar faults are reviewed. The size profile and its Fourier transform corresponding to spherical domains or crystallites with lognormal size distribution is calculated. The same is also determined for anisotropic crystallite shape. The model of strain broadening is briefly presented for different dislocation distributions. Strain anisotropy is discussed and described in terms of the anisotropic strain effect of dislocations. The concept of dislocation contrast factors is presented for different crystal systems. The broadening caused by planar defects is briefly discussed. The models described here are the theoretical background of the two microstructural methods of line profile analysis described in detail in Chapters 4 and 5.

### 2.1 Line profile parameters

The X-ray diffraction measurements usually provide the  $I(2\theta)$  intensity profiles of the different reflections. In order to compare this with theory, it is practical to convert the variable  $2\theta$  to  $g$ , the variable of the reciprocal space, where  $g = \frac{2 \sin \theta}{\lambda}$  is the absolute value of the diffraction vector. The value of  $g$  at  $2\theta_B$ , the exact Bragg position, is denoted by  $g_B$  and it is expressed as:  $g_B = \frac{2 \sin \theta_B}{\lambda}$ . In the following often  $g$  will be denoted also by  $K$ .

The variable of the intensity profiles can be expressed as:

$$s = g - g_B \approx \frac{2 \cos \theta_B}{\lambda} \Delta\theta. \quad (2.1)$$

The most important characteristic parameters of an  $I(s)$  intensity function corresponding to the Bragg peak at  $2\theta_B$  are:

- *the maximum intensity:*

$$I_0 = \max\{I(s) | s \in \mathbb{R}\}. \quad (2.2)$$

- *the Full Width at Half Maximum (FWHM):*

$$\text{FWHM}\{I(s)\} = s_2 - s_1, \text{ where } s_1 < s_2 \text{ and } I(s_1) = I(s_2) = \frac{I_0}{2}. \quad (2.3)$$

- *the integral breadth* (equivalent to the area of the normalised intensity curve):

$$\beta = \frac{\int_{-\infty}^{\infty} I(s) ds}{I_0}. \quad (2.4)$$

In X-ray diffraction the relation  $\text{FWHM} < \beta$  is usually satisfied.

## 2.2 Size broadening of diffraction profiles

With decreasing scattering volume the diffraction profiles broaden. This is called size broadening. The X-ray measurements provide the coherently scattering domain size (crystallite size). This is often smaller than the grain or subgrain size obtained by transmission electron microscopy (TEM), however, Hansen and coworkers claim that when TEM micrographs are evaluated correctly then the X-ray and TEM sizes correlate well (Winther et al., 2004). In Ungár et al. (2005) it was shown that the coherently scattering domain size given by X-ray line profile analysis provides the subgrain or cell size bounded by small angle grain boundaries or dipolar walls. In the present section the effect of the coherently scattering domain size on the diffraction profiles is discussed.

### 2.2.1 Size parameters

The definition of the commonly used different size parameters (2.12), (2.13) and (2.16) is presented through a simple case study (Warren, 1969). Let's assume an infinite plane crystallite with the thickness of  $N$  atoms. According to the theory of kinematical X-ray scattering, the line profile of this special crystallite (Warren, 1969):

$$I(s) \sim \frac{\sin^2(Nx)}{\sin^2(x)}, \quad (2.5)$$

where  $x = \pi \mathbf{G} \mathbf{a}$ ,  $\mathbf{G} = \mathbf{g} + \Delta \mathbf{g}$ ,  $\mathbf{g}$  is the diffraction vector,  $\Delta \mathbf{g}$  is a small vector, and  $\mathbf{a}$  is the unit cell vector chosen to be perpendicular to the plane of the crystallite. The function  $\frac{\sin^2(Nx)}{\sin^2(x)}$  describes the shape and position of the peaks in this special case. This function is plotted for different values of  $N$  in Fig. 2.1. It has a maximum value at positions:  $x = n\pi$ ,  $n \in \mathbb{Z}$ . This condition is equivalent to the Laue equations. The maximum value of this function is  $\lim_{x \rightarrow 0} \frac{\sin^2(Nx)}{\sin^2(x)} = N^2$ .

For large values of  $N$  this profile function can be approximated by the following simple function:

$$\frac{\sin^2(Nx)}{\sin^2 x} = N^2 \left( \frac{\sin(Nx)}{Nx} \right)^2. \quad (2.6)$$

The FWHM value of this function is given by:

$$\frac{\sin(Nx)}{Nx} = \frac{1}{\sqrt{2}}. \quad (2.7)$$

This transcendental equation can be numerically solved for  $Nx$ : the solution is  $Nx = 1.39$ , consequently, the FWHM ( $2x$ ) is reciprocally proportional to the number of lattice points perpendicular to the diffracting plane:

$$\text{FWHM} = 2.78 \frac{1}{N}. \quad (2.8)$$

This means that the profile function becomes narrower as the crystallite becomes thicker. The integral breadth of this curve is:

$$\beta = \frac{\int_{-\infty}^{\infty} \frac{\sin^2(Nx)}{x^2} dx}{N^2} = \pi \frac{1}{N}. \quad (2.9)$$

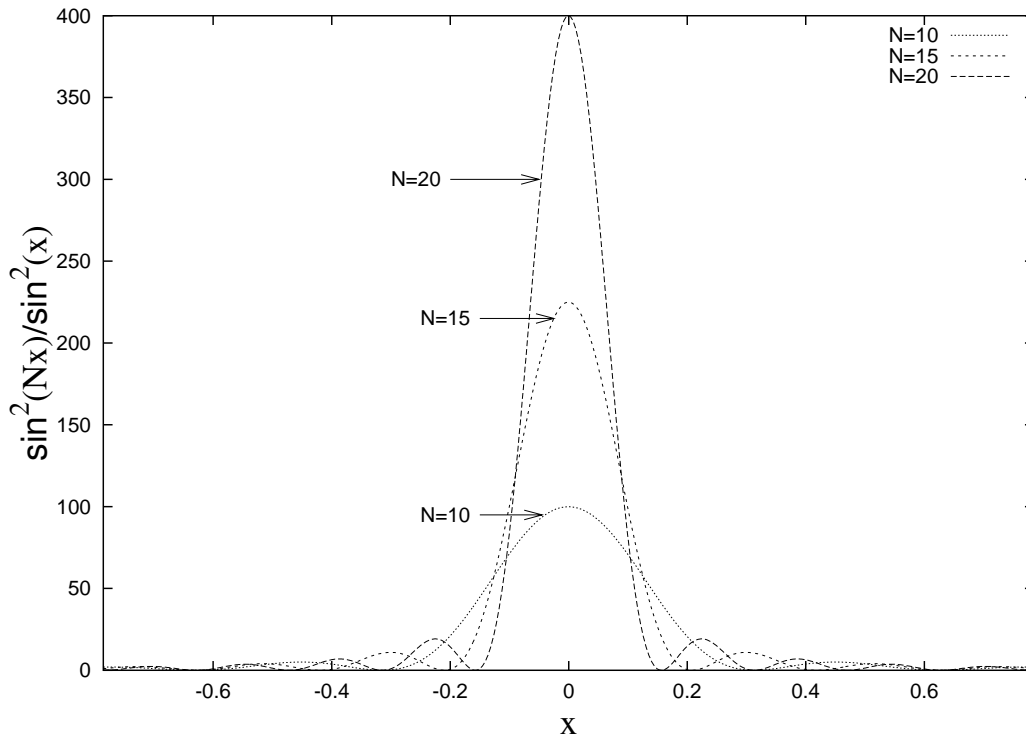


Figure 2.1: The function  $\frac{\sin^2(Nx)}{\sin^2(x)}$  plotted close to its first maximum for different values of  $N$ . As  $N$  tends to infinity, the curve becomes a delta function.

A conventional  $\theta - 2\theta$  diffractometer measures the intensity parallel to the direction of the  $\mathbf{g}$  diffraction vector as a function of  $s = |\Delta\mathbf{g}|$ . The FWHM and integral breadth value of the  $I(s)$  intensity function

as a function of  $s$  can be expressed as:

$$\text{FWHM} = \frac{2.78}{\pi} \frac{1}{N a \cos((\mathbf{G}, \mathbf{a}) \angle)} = \frac{0.9}{L_{\mathbf{G}, \mathbf{a}}}, \quad (2.10)$$

$$\beta = \frac{1}{N a \cos((\mathbf{G}, \mathbf{a}) \angle)} = \frac{1}{L_{\mathbf{G}, \mathbf{a}}}, \quad (2.11)$$

where  $L_{\mathbf{G}, \mathbf{a}} = N a \cos((\mathbf{G}, \mathbf{a}) \angle)$  is the projection of the crystallite width in the direction of the diffraction vector. This means that by measuring the widths of the peak profiles, only the crystallite size parallel to the diffraction vector can be determined.

For the reflection  $h00$ ,  $L_{\mathbf{G}, \mathbf{a}}$  is equal to the thickness of the crystal, i.e. either to  $\frac{0.9}{\text{FWHM}}$  or to  $\frac{1}{\beta}$ . The following two size parameters can be defined generally for an arbitrary  $I(s)$  intensity profile:

$$D = \frac{0.9}{\text{FWHM}}, \quad (2.12)$$

$$d = \frac{1}{\beta}. \quad (2.13)$$

Eq. (2.12) is the Scherrer (1918) equation. The theoretical description requires the Fourier transform of the intensity profile too. The Fourier transform of the function  $\frac{\sin^2(Nx)}{x^2}$  is:

$$\begin{cases} \pi(N - \pi|L|), & \text{if } |L| \leq \frac{N}{\pi} \\ 0, & \text{if } |L| > \frac{N}{\pi}. \end{cases} \quad (2.14)$$

Fig. 2.2 shows this function.

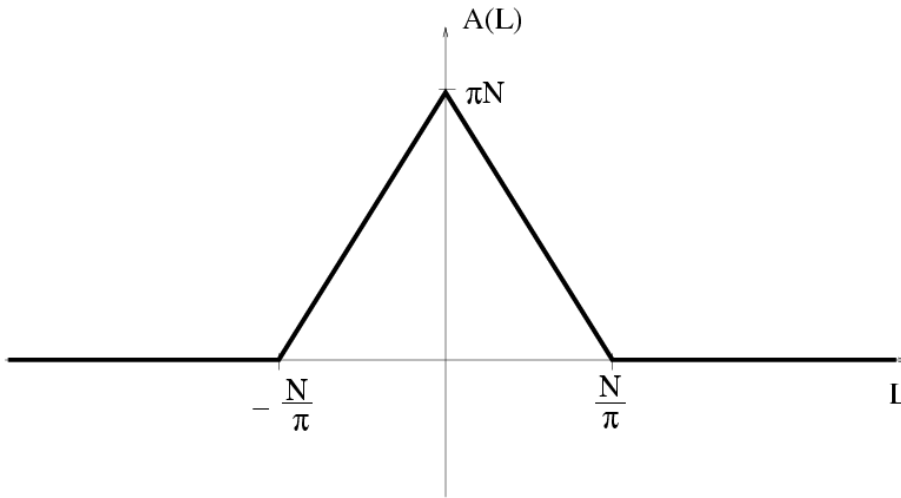


Figure 2.2: The Fourier transform of the function  $\frac{\sin^2(Nx)}{x^2}$ .

For the infinite plane crystallite with the thickness of  $N$  atoms, the Fourier transform of the  $I(s)$  size function is:

$$\begin{cases} \frac{N}{L_{G,a}} \left( N - \frac{N}{L_{G,a}} |L| \right), & \text{if } |L| \leq L_{G,a} \\ 0, & \text{if } |L| > L_{G,a}. \end{cases} \quad (2.15)$$

This means that  $L_{G,a}$  can be determined from the initial slope of the Fourier transform. The size parameter  $L_0$  is generally defined for an arbitrary  $I(s)$  intensity profile as the initial slope of the  $A_S(L)$  Fourier transform (Warren & Averbach, 1952):

$$-\frac{A_S(0)}{L_0} = \left. \frac{d}{dL} A_S(L) \right|_{L=0}. \quad (2.16)$$

The definition of  $L_0$  is illustrated in Fig. 2.6 for the case of spherical crystallites with lognormal size distribution.

In general the different size parameters satisfy the following relation:  $D \geq d \geq L_0$  (Langford & Wilson, 1978).

For spherical crystallites  $d$  and  $L_0$  are proportional to the volume and area weighted average crystallite size, respectively (Langford & Wilson, 1978):

$$\langle x \rangle_{vol} = \frac{\sum_i V_i d_i}{\sum_i V_i} = \frac{4}{3} d, \quad (2.17)$$

$$\langle x \rangle_{area} = \frac{\sum_i A_i d_i}{\sum_i A_i} = \frac{3}{2} L_0. \quad (2.18)$$

## 2.2.2 Size distribution functions

In the previous section the size broadening of a single crystallite has been discussed. A polycrystalline or fine powder sample consists of many crystallites with different sizes which can be characterised by a size distribution function. By selecting the proper size distribution and assuming a realistic crystallite shape, the size broadened profile can be calculated on a theoretical basis. Several distribution functions can be used to describe the size distribution of crystallites (Langford et al., 2000; Scardi & Leoni, 2002). Among these, one of the most flexible is the lognormal size distribution (Aitchison & Brown, 1957), which was confirmed by several observations and successful applications (Valiev et al., 1994; Terwilliger & Chiang, 1995; Krill & Birringer, 1998, Ungár et al., 1999; Langford et al., 2000). The Gamma distribution (Arley & Buch, 1950) is also suitable to describe the experimen-

tal size distributions. York (1999) proposed another distribution. These distributions are discussed below.

- i) *The lognormal distribution*: this is the most commonly used size distribution of particle size in a fine powder according to TEM observations (Aitchison & Brown, 1957). It can be shown that a milling procedure leads to a lognormal size distribution (Hinds, 1982), therefore the lognormal distribution is widely used in microstructural investigations. It is obtained by substituting the variable of a normal distribution with its logarithm. When one applies the lognormal distribution to describe the size distribution of crystallites, this means that the logarithm of the crystallite size follows a normal distribution. The density function of the lognormal size distribution has the following form:

$$f(x) = \frac{1}{\sqrt{2\pi}\sigma} \frac{1}{x} \exp \left[ -\frac{\left( \log \left( \frac{x}{m} \right) \right)^2}{2\sigma^2} \right]. \quad (2.19)$$

where  $m$  and  $\sigma$  are the parameters of the distribution,  $\log m$  is the median and  $\sigma$  is the variance of the *normal* distribution.

The parameters  $m$  and  $\sigma$  are called “median” and “variance” of the lognormal size distribution. In the MWP and CMWP procedures [S4, S6, S14] the  $b = \log m$  and  $c = \sqrt{2}\sigma$  parameters are used for the fitting procedure.

- ii) *The Gamma distribution*:

The Gamma distribution (Arley & Buch, 1950) is also flexible and can be widely used for describing observed crystallite size distributions. Its density function has the form:

$$f(x) = \frac{a}{b\Gamma(a)} \left( \frac{ax}{b} \right)^{a-1} \exp \left( -\frac{ax}{b} \right), \quad (2.20)$$

where  $a$  and  $b$  are the parameters of the distribution and  $\Gamma(x)$  is the Gamma function.

- ii) *York’s distribution*: The York distribution (York, 1999) was obtained by assuming a normal growth phenomena. The density function of the York distribution has a form similar to the Gamma distribution:

$$f(x) = \frac{1}{b\Gamma(a)} \left( \frac{ax}{b} \right)^a \exp \left( -\frac{ax}{b} \right), \quad (2.21)$$

where  $a$  and  $b$  are the parameters of the distribution and  $\Gamma(x)$  is the Gamma function.

It should be noted here that Leoni & Scardi(2004) proposed a bar-diagram for the size distribution density function and each individual column height of this diagram is fitted independently in their pattern-refining procedure. Since this is an ad-hoc, experimental distribution its discussion is not subject of this theoretical section. Langford et al. (2000) have shown that most of the above discussed

size distribution functions correlate well with experimental X-ray diffraction profiles and, that it is difficult, if not impossible, to distinguish between size distribution functions on an experimental basis.

### 2.2.3 Determination of the size profile [S1, S4, S6]

By assuming a particular crystallite shape and crystallite size distribution, one can determine the theoretical size profile. Bertaut (1949) and Guinier (1963) have shown, that the size profile of a powder specimen consisting of crystallites with arbitrary size and shape can be determined as follows:

- i) the crystallites should be divided into columns parallel to the diffraction vector  $\mathbf{g}$ ,
- ii) the “size intensity profile” is obtained as the volume-weighted sum of the intensity profiles normalized by their integral intensities corresponding to each column.

The intensity profile normalized by its integral intensity of a column with area  $A_i$  and height  $M_i$  is:

$$\frac{\sin^2(M_i \pi s)}{M_i (\pi s)^2}. \quad (2.22)$$

By summing up the contributions from all columns of all crystallites using the volume of the column as weight, the intensity distribution becomes:

$$I(s) \sim \sum_i \frac{\sin^2(M_i \pi s)}{M_i (\pi s)^2} A_i M_i. \quad (2.23)$$

Let us introduce  $g(M) dM$  as the sum of the volumes of the columns with height between  $M$  and  $M + dM$  from all crystallites:

$$g(M) dM = \sum_j dV_j(M, dM). \quad (2.24)$$

Using this quantity, the intensity distribution can be expressed as:

$$I(s) \sim \int_0^{\infty} \frac{\sin^2(M \pi s)}{M (\pi s)^2} g(M) dM, \quad (2.25)$$

In this way, the size profile can be obtained by determining  $g(M) dM$ , which depends on the crystallite shape and the size distribution of the crystallites. In the following, the size profile is calculated according to the lognormal size distribution, and for spherical (i) and ellipsoidal (ii) crystallite shapes [S4, S6]. Latter is a simple and general description of deviations from spherical shape. It also accounts for anisotropic size broadening as a function of  $hkl$ .

For a particular crystallite shape  $g(M) dM$  is determined first for one crystallite. This calculation is based on the geometrical properties of the crystallite shape. The size profile is obtained by summing up for all crystallites using the crystallite size distribution function. In the case of *spherical* crystallites and *lognormal* size distribution,  $g(M) dM$  is obtained as follows:

Using the notations of Fig. 2.3 the following geometrical equation can be written:

$$x^2 = y^2 + \left(\frac{M}{2}\right)^2, \quad (2.26)$$

For one crystallite  $g(M) dM$  is equal to the volume of the part of the sphere with column length between  $M$  and  $M + dM$ :

$$g(M) dM \approx -2\pi y dy M. \quad (2.27)$$

By differentiating eq. (2.26) the following is obtained:  $2y dy = -\frac{M dM}{2}$ . Therefore for *one* crystallite:

$$g(M) dM \sim M^2 dM. \quad (2.28)$$

Since  $f(x) dx$  is proportional to the number of the crystallites with diameter between  $x$  and  $x + dx$  and all the crystallites with diameter  $x \geq M$  contain the column length  $M$ :

$$g(M) dM \sim \left( \int_M^\infty f(x) dx \right) M^2 dM. \quad (2.29)$$

Using the distribution density function in (2.19), this integral can be expressed as:

$$\int_M^\infty f(x) dx = \frac{1}{2} \operatorname{erfc} \left[ \frac{\log \left( \frac{M}{m} \right)}{\sqrt{2}\sigma} \right], \quad (2.30)$$

where  $\operatorname{erfc}$  is the complementary error function, defined as:

$$\operatorname{erfc}(x) = \frac{2}{\sqrt{\pi}} \int_x^\infty e^{-t^2} dt. \quad (2.31)$$

Thus for *all* crystallites  $g(M) dM$  can be written as:

$$g(M) dM \sim M^2 \operatorname{erfc} \left[ \frac{\log \left( \frac{M}{m} \right)}{\sqrt{2}\sigma} \right] dM. \quad (2.32)$$

Using eq. (2.25) the following size function is obtained [S1]:

$$I^S(s) = \int_0^\infty M \frac{\sin^2(M\pi s)}{(\pi s)^2} \operatorname{erfc} \left[ \frac{\log \left( \frac{M}{m} \right)}{\sqrt{2}\sigma} \right] dM. \quad (2.33)$$

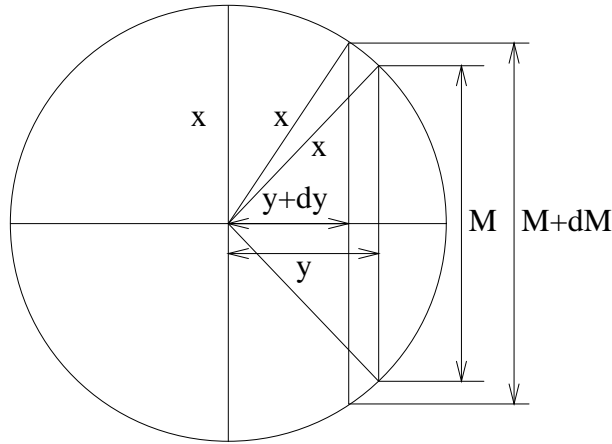


Figure 2.3: Determination of  $g(M) dM$  in the case of a spherical crystallite with radius  $x$ . The goal is to calculate the volume of the part of the sphere with column length between  $M$  and  $M + dM$ . This part of the sphere is approximated by an annulus based prism and it is expressed with  $M$ ,  $x$  and  $y$ , where  $y$  is the radius of the annulus.

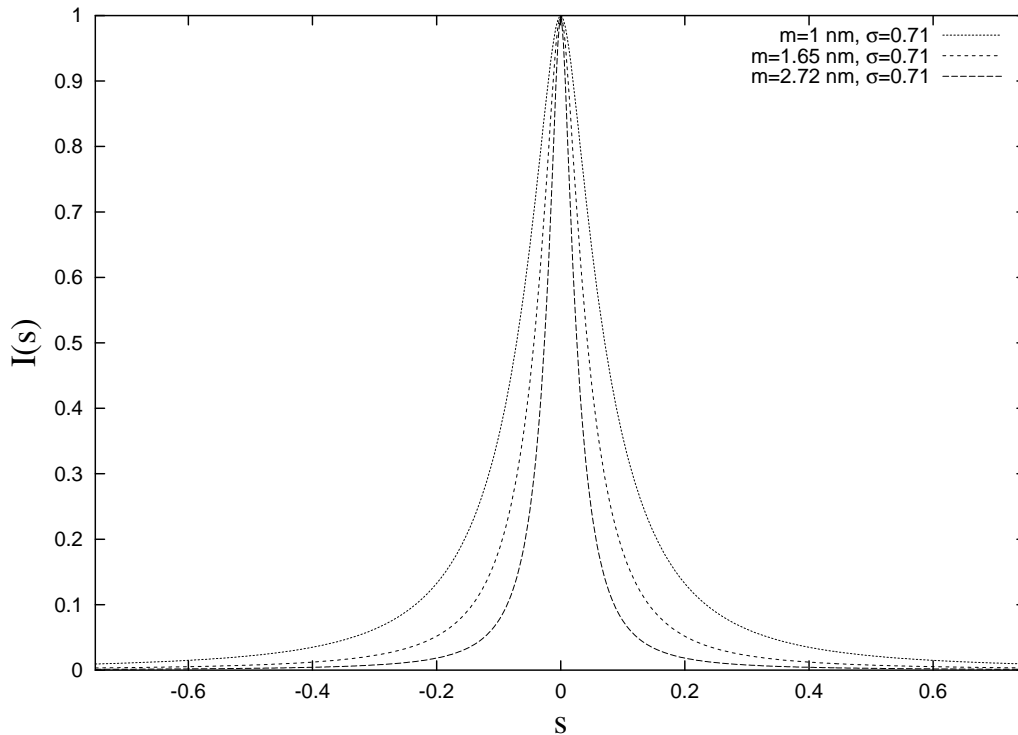


Figure 2.4: The size function for spherical crystallites with lognormal distribution with fixed value of  $\sigma = 0.71$ , as a function of  $s$ . The value of  $m$  varies for the different curves. The value of  $m$  is indicated in the upper right corner of the figure.

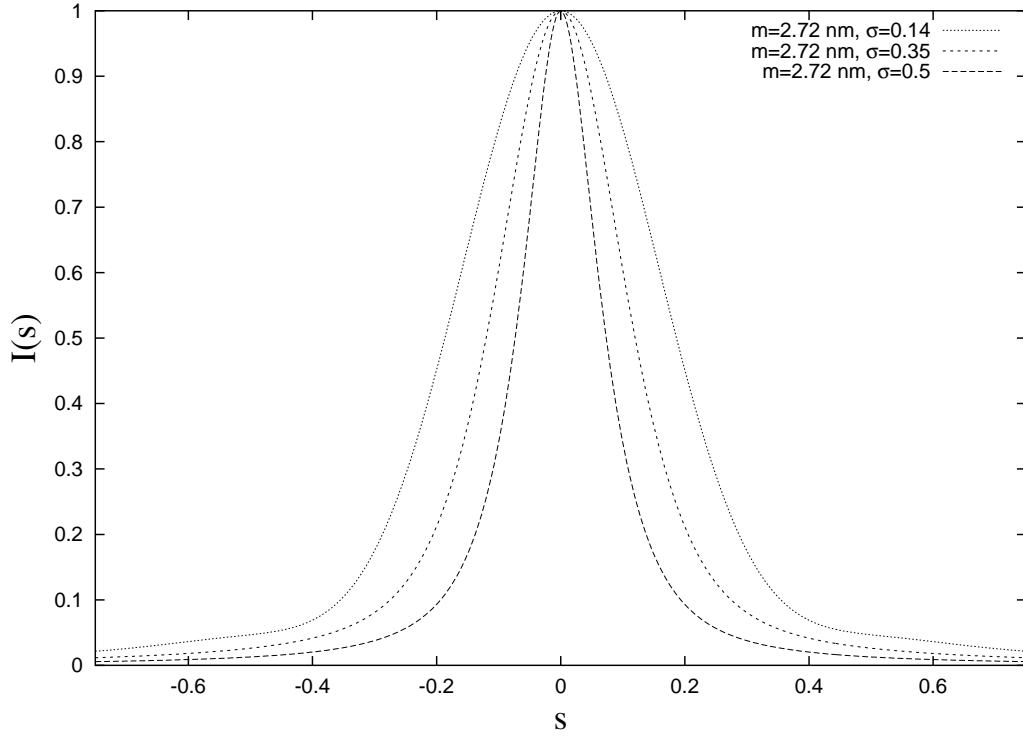


Figure 2.5: The size function for spherical crystallites with lognormal distribution with fixed value of  $m = 2.72$  nm, as a function of  $s$ . The value of  $\sigma$  varies for the different curves. The value of  $\sigma$  is indicated in the upper right corner of the figure.

This size function is plotted for different values of  $m$  and  $\sigma$  in Figs. 2.4 and 2.5.

In order to speed-up the numerical calculations in the MWP and CMWP methods [S4, S6], the explicit form of the Fourier transform of the size profile is required. In the following, the Fourier transform of the theoretical size profile is determined [S4, S6].

According to eq. (2.14), the Fourier transform of the function  $\frac{\sin^2(M\pi s)}{(\pi s)^2}$  is:

$$\begin{cases} M - |L|, & \text{if } |L| \leq M \\ 0, & \text{if } |L| > M. \end{cases} \quad (2.34)$$

Using this equation, the Fourier transform of the size function (2.33) can be expressed as:

$$\begin{aligned}
A^S(L) &= 2 \int_0^{\infty} I^S(s) \cos(2\pi s L) ds = \\
&= 2 \int_0^{\infty} \left( \int_0^{\infty} M \frac{\sin^2(M\pi s)}{(\pi s)^2} \operatorname{erfc} \left[ \frac{\log\left(\frac{M}{m}\right)}{\sqrt{2}\sigma} \right] dM \right) \cos(2\pi s L) ds = \\
&= \int_0^{\infty} M \left( 2 \int_0^{\infty} \frac{\sin^2(M\pi s)}{(\pi s)^2} \cos(2\pi s L) ds \right) \operatorname{erfc} \left[ \frac{\log\left(\frac{M}{m}\right)}{\sqrt{2}\sigma} \right] dM = \\
&= \int_{|L|}^{\infty} (M^2 - |L|M) \operatorname{erfc} \left[ \frac{\log\left(\frac{M}{m}\right)}{\sqrt{2}\sigma} \right] dM.
\end{aligned} \tag{2.35}$$

By using substitutions and partial integration this integral can be further simplified:

$$\begin{aligned}
A^S(L) &= \frac{m^3 \exp\left(\frac{9}{4}(\sqrt{2}\sigma)^2\right)}{3} \operatorname{erfc} \left[ \frac{\log\left(\frac{|L|}{m}\right)}{\sqrt{2}\sigma} - \frac{3}{2}\sqrt{2}\sigma \right] - \\
&\frac{m^2 \exp(\sqrt{2}\sigma)^2}{2} |L| \operatorname{erfc} \left[ \frac{\log\left(\frac{|L|}{m}\right)}{\sqrt{2}\sigma} - \sqrt{2}\sigma \right] + \\
&\frac{|L|^3}{6} \operatorname{erfc} \left[ \frac{\log\left(\frac{|L|}{m}\right)}{\sqrt{2}\sigma} \right].
\end{aligned} \tag{2.36}$$

Dividing  $A^S(L)$  by the maximum value, the normalised size Fourier transform is obtained. The maximum value of  $A^S(L)$  is:

$$A^S(0) = \frac{2m^3 \exp\left(\frac{9}{4}(\sqrt{2}\sigma)^2\right)}{3}. \tag{2.37}$$

An example for the plot of the size Fourier transform is shown in Fig. 2.6. It is noted that instead of calculating the Fourier transform of eq. 2.23, Dr. Gubicza calculated the size Fourier transform (Ungár et al., 2001) according to the following direct equation for  $A^S(L)$  given in Guinier (1963):

$$A^S(\mathbf{L}) = \frac{1}{V} \int \sigma(\mathbf{r})\sigma(\mathbf{r} + \mathbf{L}) d^3\mathbf{r}, \tag{2.38}$$

where  $\sigma(\mathbf{r})=1$  if  $\mathbf{r} \in$  “scattering object” otherwise  $\sigma(\mathbf{r})=0$ . The two different calculations are leading exactly to the same result for  $A(L)$  [S4, S6].

The formulae of  $I^S(s)$  and its Fourier transform  $A^S(L)$  enable to express the size parameters as a function of the parameters of the distribution. The derivation of  $A^S(L)$  gives the  $L_0$  size parameter:

$$L_0 = -\frac{A^S(0)}{\left(\frac{dA^S(L)}{dL}\right)_{L=0}} = \frac{2m \exp\left(\frac{5}{4}(\sqrt{2}\sigma)^2\right)}{3}. \quad (2.39)$$

The maximum value of the size profile is:

$$I^S(0) = \int_0^{\infty} M^3 \operatorname{erfc}\left[\frac{\log\left(\frac{M}{m}\right)}{\sqrt{2}\sigma}\right] dM. \quad (2.40)$$

The integral of the normalized size profile leads to the size parameter  $d$ :

$$d = \frac{1}{\beta} = \frac{I^S(0)}{\int_{-\infty}^{\infty} I^S(s) ds} = \frac{I^S(0)}{A^S(0)} = \frac{3m \exp\left(\frac{7}{4}(\sqrt{2}\sigma)^2\right)}{4}. \quad (2.41)$$

According to eqs. (2.17) and (2.18), the following is obtained for the volume and area averaged crystallite size:

$$\langle x \rangle_{vol} = m \exp(3.5\sigma^2) \quad (2.42)$$

$$\langle x \rangle_{area} = m \exp(2.5\sigma^2) \quad (2.43)$$

It is noted that these expressions for the volume and area averaged mean crystallite size are identical to those given by Hinds (1982) and Langford et al. (2000).

## 2.2.4 Anisotropic size broadening [S1, S4, S6]

If the crystallite shape is spherical, the size function is isotropic and thus independent of the  $hkl$  indices. If a non-spherical crystallite shape is supposed, the size function becomes anisotropic and it depends on the  $hkl$  indices. In the following the size function is calculated for crystallites with *spherically ellipsoidal* shape and *lognormal* size distribution [S4, S6].

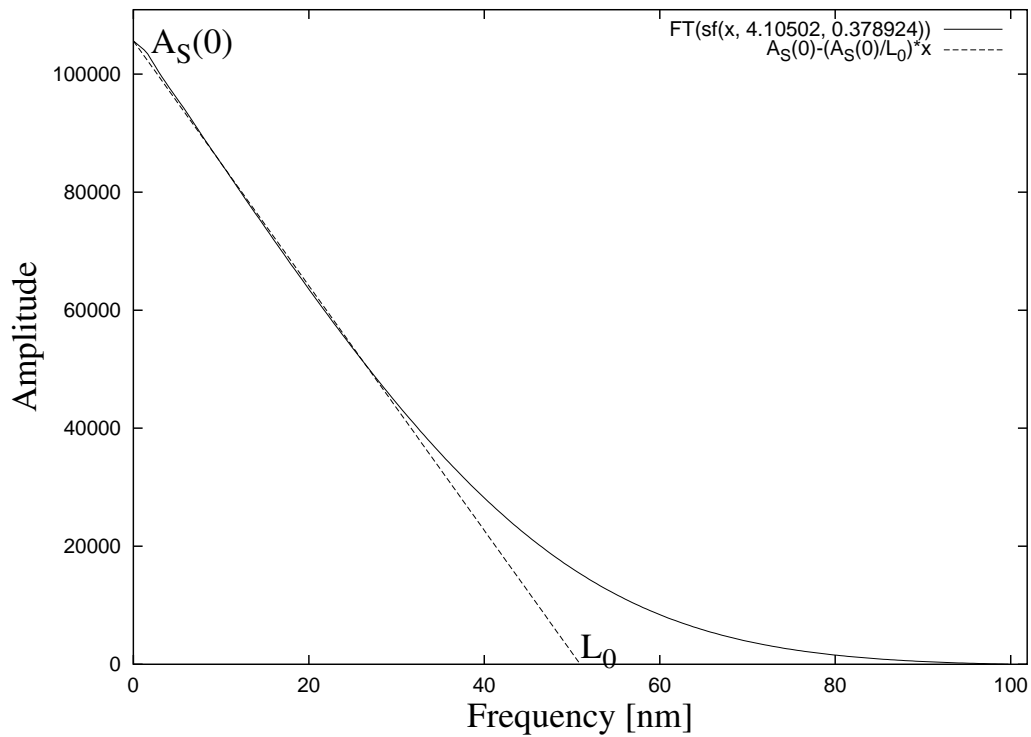


Figure 2.6: The theoretical Fourier transform of a size profile for spherical crystallites with lognormal size distribution. The initial slope defining  $L_0$  is also indicated in the figure.

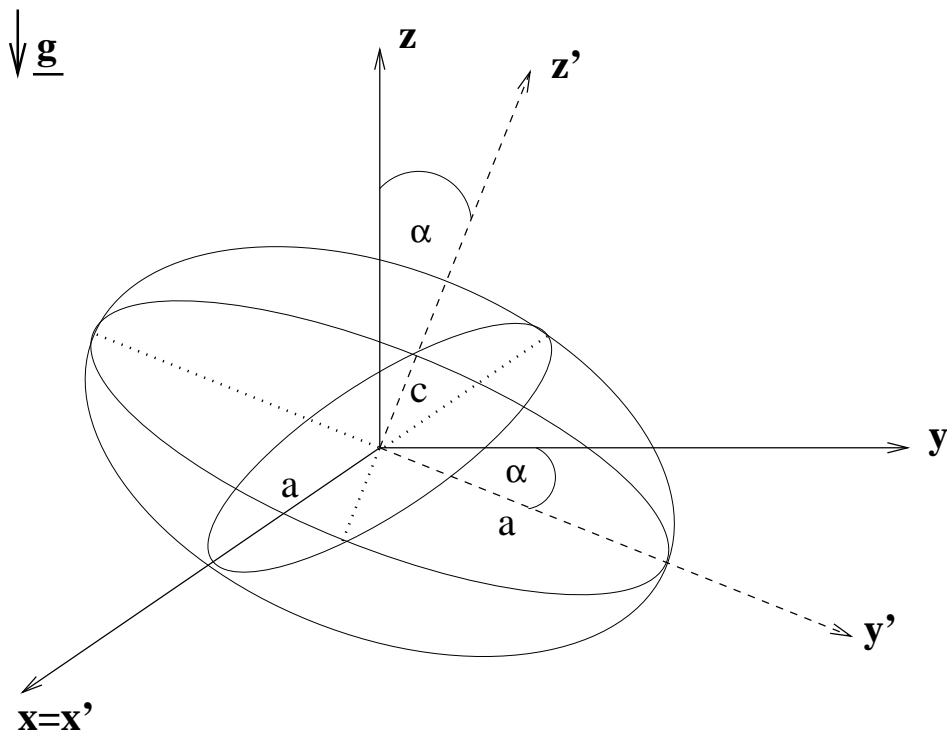


Figure 2.7: The determination of the ellipsoidal size function. The radii of the spherical ellipsoid are:  $a$  and  $c$ . There are two coordinate systems:  $x, y, z$  and  $x', y', z'$ . The latter is the eigensystem. The two coordinate systems are rotated by an angle of  $\alpha$  around the axis  $x$ . The diffraction vector  $\mathbf{g}$  is also indicated. The goal is to determine  $g(M) dM$  based on the geometrical properties of the part of the ellipsoid with column length between  $M$  and  $M + dM$  parallel to  $\mathbf{g}$ .

The determination of  $g(M) dM$  consists of the following steps (see Fig. 2.7 for the notations).

1. construction of the equation of the ellipsoid with ellipticity  $\varepsilon = \frac{c}{a}$  in the eigensystem denoted by  $x', y', z'$ .
2. transformation with rotation of angle  $\alpha$  around the axis  $x$  into the system  $x, y, z$  ( $\alpha$  is the angle between the diffraction vector and the axis of revolution of the ellipsoid and  $z$  is parallel to  $\mathbf{g}$ ).
3. expression of the column length  $M$ :  $M(x, y) = z_2(x, y) - z_1(x, y)$ , where  $z_1$  and  $z_2$  are determined using the equation of the ellipsoid.
4. determination of the area,  $T(M)$ , of the plane-curve determined by equation  $M(x, y) = M$  (which is in fact an ellipse).
5. For one crystallite the following is obtained:

$$g(M) dM = M[T(M) - T(M + dM)] = \frac{\pi}{2} h(\varepsilon, \alpha) M^2 dM, \quad (2.44)$$

where  $h(\varepsilon, \alpha)$  is determined using the equation of  $M(x, y)$ . It is noted, that in the case of a sphere:  $h(1, \alpha) = 1$ .

6. calculation of the maximum column length  $M_{max}$ :

$$M_{max} = \frac{2a}{\sqrt{1 + \left(\frac{1}{\varepsilon^2} - 1\right) \cos^2 \alpha}} \quad (2.45)$$

7. summing up for all crystallites with the column length  $M$  and using the lognormal size distribution density function  $f(x)$ :

$$g(M) dM \sim h(\varepsilon, \alpha) M^2 \operatorname{erfc} \left[ \frac{\log \left( \frac{M \sqrt{1 + \left(\frac{1}{\varepsilon^2} - 1\right) \cos^2 \alpha}}{m} \right)}{\sqrt{2}\sigma} \right] dM. \quad (2.46)$$

The size function obtained in this way is identical to that corresponding to spherical crystallites, the only difference is that the parameter  $m$  becomes  $hkl$ -dependent and the parameter  $m$  of the distribution has to be substituted for the following  $hkl$  dependent expression:

$$m_{hkl} = \frac{m_A}{\sqrt{1 + \left(\frac{1}{\varepsilon^2} - 1\right) \cos^2 \alpha_{hkl}}}, \quad (2.47)$$

where  $m_A$  is the parameter  $m$  of the size distribution.

If the relative orientation of the unit cell vectors to the axis of revolution of the ellipsoid are known,  $\cos \alpha_{hkl}$  can be expressed with the  $hkl$  indices.

For cubic crystals, if the axis of revolution is parallel to the unit cell vector  $\mathbf{a}$ :

$$\cos \alpha_{hkl} = \frac{l}{\sqrt{h^2 + k^2 + l^2}} \quad (2.48)$$

For hexagonal crystals, if the axis of revolution is parallel to the unit cell vector  $\mathbf{c}$ :

$$\cos \alpha_{hkl} = \frac{l}{\sqrt{\frac{4}{3} \frac{c^2}{a^2} (h^2 + hk + k^2) + l^2}}. \quad (2.49)$$

It is noted that Scardi & Leoni (2002) calculated the  $hkl$  dependent size broadening for different polyhedra, which is another possibility to introduce size anisotropy.

## 2.3 Strain broadening

In a real crystal, due to the lattice defects, the atoms are displaced relative to their ideal position. For this reason the reciprocal space may also be distorted and the condition of diffraction is satisfied not only in the ideal positions of the reciprocal lattice points, but in a finite volume in their proximity. This effect is called strain broadening. Warren & Averbach (1952) gave the Fourier transform of the X-ray line profile if size and strain effects are present simultaneously:

$$A(L) = A^S(L)A^D(L), \quad (2.50)$$

where the strain Fourier coefficients can be expressed in the following form:

$$A^D(L) = \exp(-2\pi^2 g^2 L^2 \langle \varepsilon_{\mathbf{g},L}^2 \rangle), \quad (2.51)$$

where  $g$  is the absolute value of the diffraction vector,  $\langle \epsilon_{\mathbf{g},L}^2 \rangle$  is the *mean square strain*, depending on the displacement of the atoms relative to their ideal position, and the brackets indicate spatial averaging.

According to the continuum theory of elasticity, the longitudinal strain parallel to the direction of the  $\mathbf{g}$  diffraction vector is defined as (Wilkins, 1970):

$$\epsilon_{\mathbf{g}}(L, \mathbf{r}) = \frac{\frac{\mathbf{g}}{|\mathbf{g}|} \mathbf{u}(\mathbf{r} + \frac{L}{2} \frac{\mathbf{g}}{|\mathbf{g}|}) - \frac{\mathbf{g}}{|\mathbf{g}|} \mathbf{u}(\mathbf{r} - \frac{L}{2} \frac{\mathbf{g}}{|\mathbf{g}|})}{L}, \quad (2.52)$$

where  $\mathbf{u}$  is the displacement field and  $L$  is the distance of the points  $\mathbf{r} + \frac{L}{2} \frac{\mathbf{g}}{|\mathbf{g}|}$  and  $\mathbf{r} - \frac{L}{2} \frac{\mathbf{g}}{|\mathbf{g}|}$ . Thus the mean square strain is obtained as:

$$\langle \epsilon_{\mathbf{g},L}^2 \rangle = \frac{\iiint_V (\epsilon_{\mathbf{g}}(L, \mathbf{r}))^2 d^3\mathbf{r}}{\iiint_V d^3\mathbf{r}} \quad (2.53)$$

For discrete atoms, the strain,  $\epsilon_{\mathbf{g},L}$  is defined as:

$$\epsilon_{\mathbf{g},n}^{(j,j')} = \frac{\frac{\mathbf{g}}{|\mathbf{g}|} \mathbf{u}(\mathbf{r}_j) - \frac{\mathbf{g}}{|\mathbf{g}|} \mathbf{u}(\mathbf{r}_{j'})}{nl_0}, \quad (2.54)$$

where  $j$  and  $j'$  are the indices of the atoms in the direction of  $\mathbf{g}$ ,  $n = j - j'$ ,  $L = nl_0$  and  $l_0$  is the distance between two atoms in the direction of  $\mathbf{g}$  (Warren & Averbach, 1952). The mean square strain is obtained as the square of the strain averaged over all atomic pairs with the distance of  $nl_0$ :

$$\langle \epsilon_{\mathbf{g},L}^2 \rangle = \frac{\sum_{j-j'=n} (\epsilon_{\mathbf{g},n}^{(j,j')})^2}{\sum_{j-j'=n} 1} \quad (2.55)$$

Several authors worked on the determination of the mean square strain, including Warren & Averbach (1952), Krivoglaz & Ryaboshapka (1963) and Wilkins (1970). Warren and coworkers (1952, 1959) assumed either random atomic displacements and/or stacking faults. Krivoglaz (1969) and Wilkins (1970) assumed dislocations as the main source of peak broadening close to the fundamental Bragg positions. Krivoglaz and Ryaboshapka (1963) assumed a totally random distribution of dislocations in the entire crystal and for small  $L$  values obtained:

$$\langle \epsilon_{\mathbf{g},L}^2 \rangle = \left( \frac{b}{2\pi} \right)^2 \pi \rho C \log \left( \frac{D}{L} \right), \quad (2.56)$$

where  $D$  is the crystal size. The problem with this formula is that (i) it diverges as  $D$  tends to infinity and (ii) using this strain function, the strain Fourier transform does not decay as  $L$  tends to infinity. However, for small  $L$  values this logarithmic expression enables to estimate the dislocation density,

for more details see the description of the *modified* Warren-Averbach method in section 3.2.

The logarithmic behaviour of the mean square strain for small  $L$  values, as a general property of any dislocation configuration was derived by a fairly exact method by Groma (1998, 2003).

A numerical code has recently been developed in [S23] to calculate the mean square strain and the strain profile for an arbitrary sized (e.g. 100x100 nm) crystal box containing up to a few hundred randomly distributed straight parallel edge dislocations. The numerical evaluation of eq. (2.53) has proved the logarithmic  $L$  dependence of  $\langle \varepsilon_{\mathbf{g},L}^2 \rangle$  for small  $L$  values in correlation with Krivoglaz (1969), Wilkens (1970) and Groma (1998). Fig. 2.8 shows a typical example for 10 dislocations in a 50x50 nm crystal box.

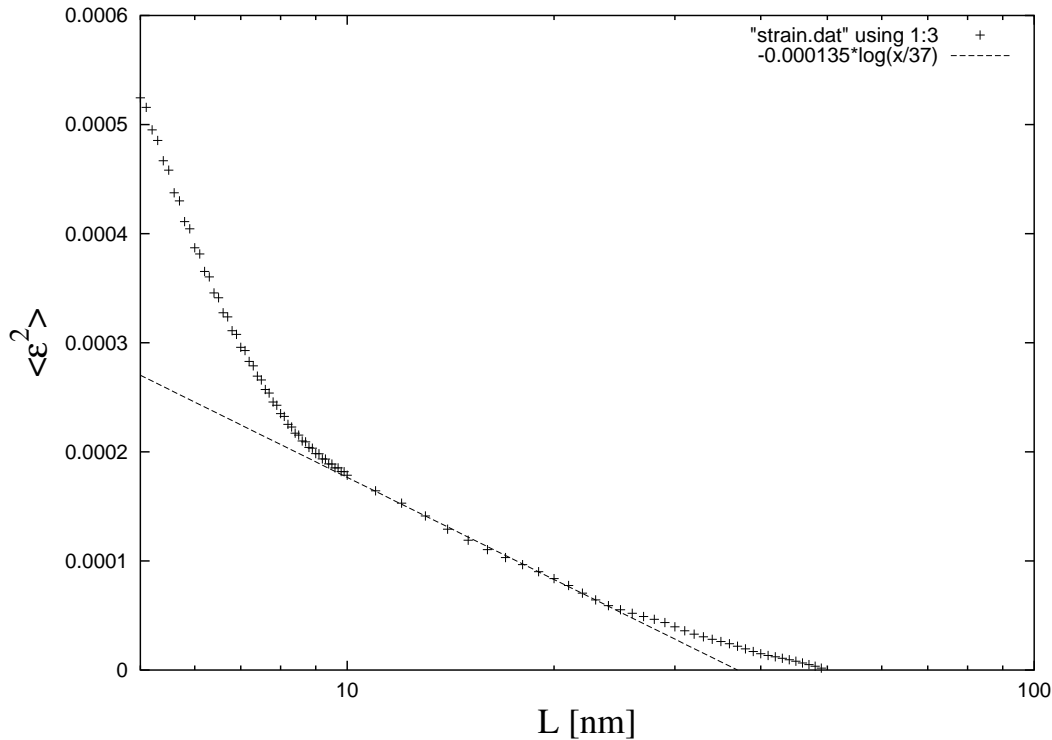


Figure 2.8: The mean square strain calculated for 10 randomly distributed edge dislocations in a 50x50 nm crystal box. The  $x$  scale is logarithmic. The dashed line indicates that the calculated mean square strain can be well described by a logarithmic function between approx. 10 and 25 nm.

Wilkens (1970) calculated the mean square strain in the entire  $L$  range assuming the so called *restrictedly random* distribution of dislocations. This calculation is discussed in somewhat more detail in the next paragraph.

### 2.3.1 The Krivoglaz–Wilkens model of dislocations

Wilkens improved the model of Krivoglaz by introducing a length parameter, the effective outer cut off radius of dislocations ( $R_e^*$ ), instead of the crystal diameter, by this eliminating the logarithmic singularity in the expression of the mean square strain in eq. (2.56). He assumed that the crystal contains separate regions with diameter of  $R_e^*$ , in which parallel screw dislocations are randomly

distributed. Within each of these regions the distribution of the dislocations is completely random and they have a density of exactly  $\rho$ . There is no interaction between dislocations outside of these regions. He called this special dislocation configuration restrictedly random distribution and the mean square strain was derived in the following form for the entire  $L$  range (Wilkins, 1970):

$$\langle \epsilon_{g,L}^2 \rangle = \left( \frac{b}{2\pi} \right)^2 \pi \rho C f \left( \frac{L}{R_e^*} \right), \quad (2.57)$$

where  $b$  is the absolute value of the Burgers-vector,  $\rho$  is the dislocation density,  $C$  is the contrast factor of the dislocations and  $f$  is the strain function. In the following  $f$  will be called the Wilkens function.  $f$  has the following explicit form, see eqs. A6-A8 in Appendix A in Wilkins (1970):

$$\begin{aligned} f^*(\eta) = & -\log \eta + \left( \frac{7}{4} - \log 2 \right) + \frac{512}{90\pi} \frac{1}{\eta} + \\ & \frac{2}{\pi} \left[ 1 - \frac{1}{4\eta^2} \right] \int_0^\eta \frac{\arcsin V}{V} dV - \\ & \frac{1}{\pi} \left[ \frac{769}{180} \frac{1}{\eta} + \frac{41}{90} \eta + \frac{2}{90} \eta^3 \right] \sqrt{1 - \eta^2} - \\ & \frac{1}{\pi} \left[ \frac{11}{12} \frac{1}{\eta^2} + \frac{7}{2} + \frac{1}{3} \eta^2 \right] \arcsin \eta + \frac{1}{6} \eta^2, \quad \text{if } \eta \leq 1, \\ f^*(\eta) = & \frac{512}{90\pi} \frac{1}{\eta} - \left[ \frac{11}{24} + \frac{1}{4} \log 2 \eta \right] \frac{1}{\eta^2}, \quad \text{if } \eta \geq 1, \end{aligned} \quad (2.58)$$

where  $f \left( \frac{L}{R_e^*} \right) = f^*(\eta)$  and  $\eta = \frac{1}{2} \exp \left( -\frac{1}{4} \right) \frac{L}{R_e^*}$ .

The Wilkens function and its approximations for small and large values of  $L$  are plotted in Fig. 2.9. In the Wilkens function the same logarithmic term is present as in the Krivoglaz model, but it does not diverge with the crystallite size, since it depends on the correlation length parameter,  $R_e^*$ , which is a finite parameter of the distribution. A common property of the Krivoglaz and Wilkens models is that the mean square strain has a singularity for small values of  $L$ . This singularity does not affect the shape of the line profiles considerably, since in the Fourier transform it is multiplied by  $L^2$  and this multiplier strongly compensates the divergence:  $L^2 \log L \rightarrow 0$ , if  $L \rightarrow 0$ .

It is noted that in previous papers  $R_e = \exp(2) R_e^* = 7.4 R_e^*$  was used as the effective outer cut-off radius of dislocations (Ungár et al. 1984; Wilkins, 1988; Hecker et al., 1997).

Inserting eq. (2.57) into (2.51), one obtains the strain Fourier-transform:

$$A^D(L) = \exp \left[ -\frac{\pi b^2}{2} (g^2 C) \rho L^2 f \left( \frac{L}{R_e^*} \right) \right]. \quad (2.59)$$

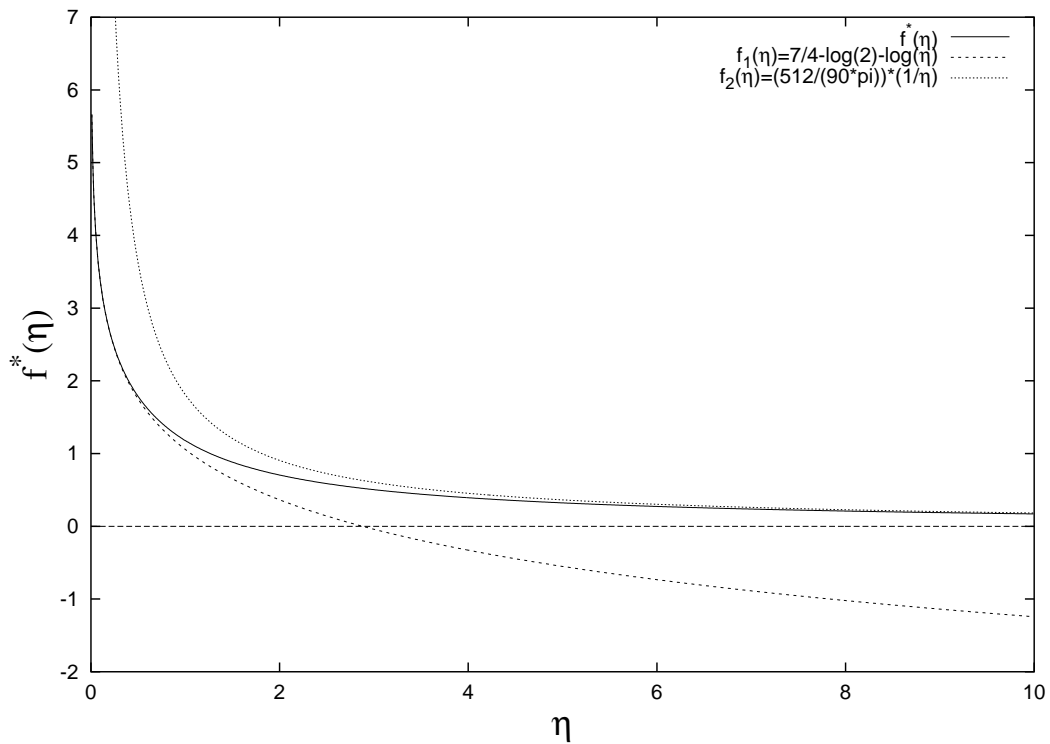


Figure 2.9:  $f^*(\eta)$ , the Wilkens function (where  $\eta = \frac{1}{2} \exp\left(-\frac{1}{4}\right) \frac{L}{R_e^*}$ ) and two of its approximations:  $f_1(\eta) = \frac{7}{4} - \log 2 - \log(\eta)$ , the function describing its logarithmic singularity at  $\eta \rightarrow 0$  and  $f_2(\eta) = \frac{512}{90\pi} \frac{1}{\eta}$ , the hyperbolic function describing the tails of the function.

Kamminga and Delhez (2000) have shown using numerical simulations that the line profile calculated by the Wilkens model is also valid for edge dislocations and curved dislocations.

Wilkens (1978) introduced  $M^*$ , the dislocation arrangement parameter, which is a dimensionless parameter:

$$M^* = R_e^* \sqrt{\rho} \quad (2.60)$$

The  $M^*$  parameter characterizes the dislocation arrangement:

- if the value of  $M^*$  is small, the correlation between the dislocations is strong
- if the value of  $M^*$  is large, the dislocations are distributed randomly in the crystallite

Fig. 2.10 shows two dislocation configurations: in the first the dislocations are strongly correlated and the value of  $M^*$  is small and in the second the correlation is weak and  $M^*$  is large. Fig. 2.11 presents the strain profile for fixed  $\rho$  and variable  $M^*$  values.

It is noted that the Fourier transform given by the Wilkens model is real, this means that its inverse Fourier transform, the strain intensity profile is symmetric, which is not always fulfilled in case of real measurements, e.g. in single crystals with dislocation cell structure, the line profiles can be asymmetric. Several different dislocation configuration can produce asymmetric broadening of the profiles (Ungár et al., 1984; Mughrabi et al., 1986; Gaál, 1973, 1976, 1984). In Ungár et al. (1984) and Mughrabi et al. (1986) authors propose a special cell-wall structure for dislocations: a matrix structure where the dislocation density in the dislocation walls is significantly larger (so the material is harder) than in the cell interiors. This model is called “Mughrabi’s composite model”. In section 5.2 an implementation of this model for X-ray line profile analysis is presented. Gaál developed a model for a far more general distribution of dislocations, in which a configuration of polarised dislocation dipoles leads to asymmetric strain broadening (Gaál, 1973, 1976, 1984). It should also be noted that not only strain broadening causes asymmetric broadening of the line profiles, but planar faults also introduce asymmetry in the profile shape, for more details see section 2.4.

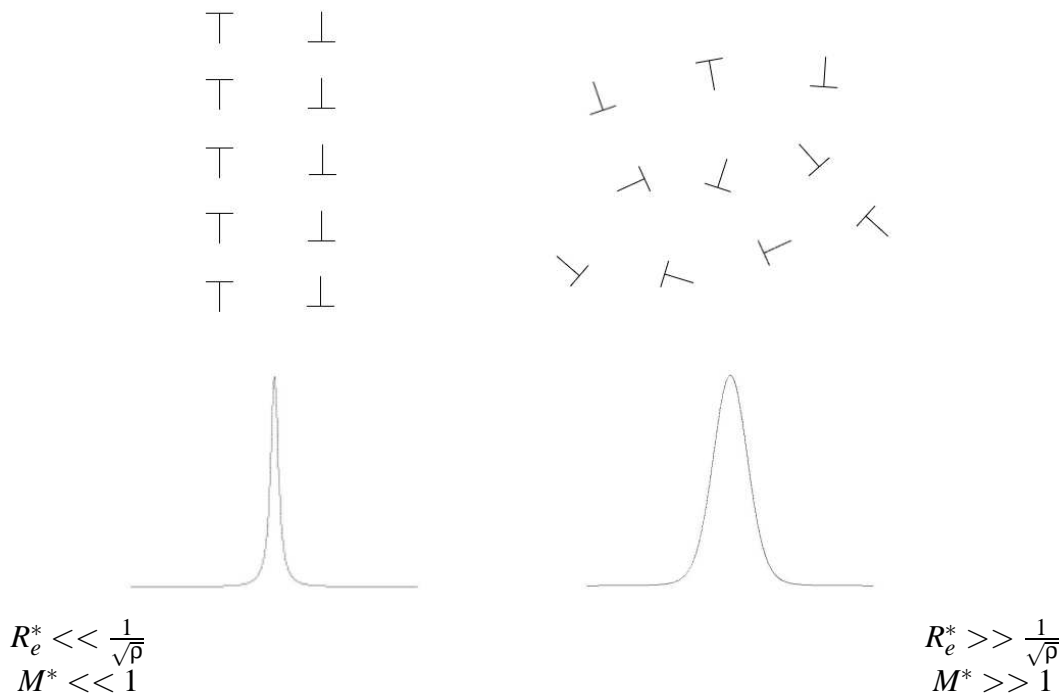


Figure 2.10: Schematic representation of dislocation configurations and the corresponding strain profile for small and large values of the  $M^*$  parameter. The y scale of the strain profiles is logarithmic.

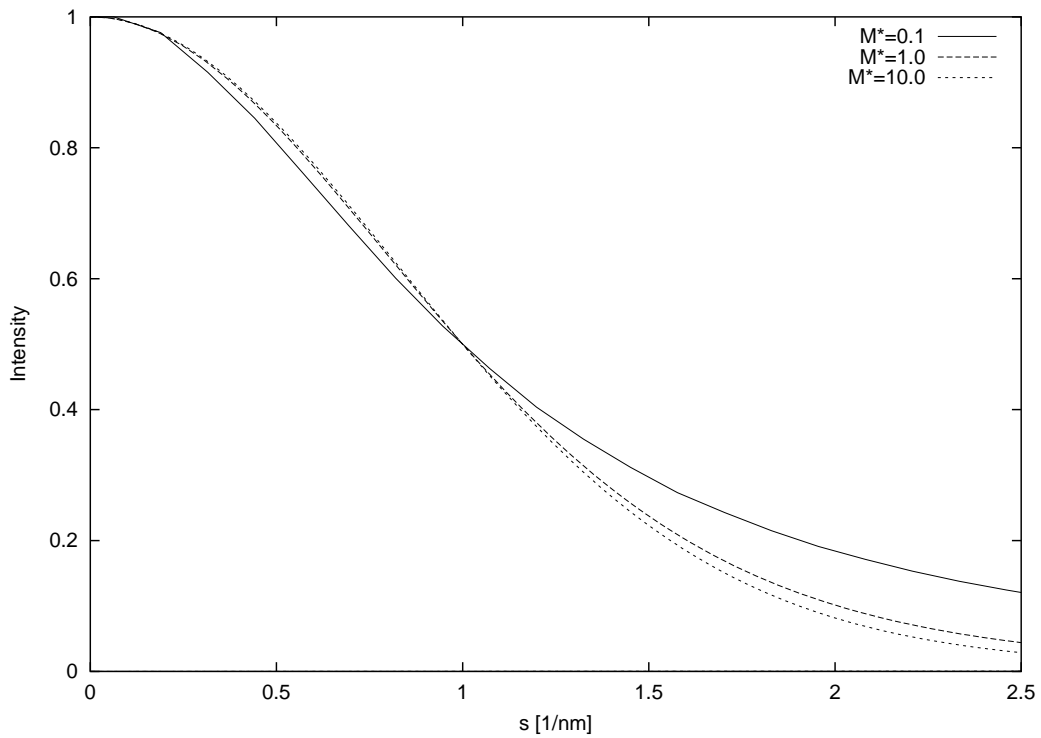


Figure 2.11: The shape of the strain profile for fixed  $\rho$  and variable  $M^*$  values. It is noted that for each profile the  $s$  variable is normalized by the FWHM value of the profile.

### 2.3.2 Strain anisotropy: the concept of contrast factors

Strain anisotropy means that the broadening of the profiles show an anisotropic behaviour as a function of the  $hkl$  indices: the width of the profiles is not a monotonous function of the length of the diffraction vector or its square, see for example the Williamson-Hall plot (Williamson & Hall, 1953) in Fig. 3.1. This is explained by the anisotropy of the mean square strain:  $\langle \varepsilon_{\mathbf{g},L}^2 \rangle$  depends on the  $hkl$  indices. This dependence is described by the contrast (or orientation) factors  $C$ . The value of the contrast factors depend on the elastic constants of the material and on the relative orientation of the diffraction vector ( $\mathbf{g}$ ), the Burgers vector ( $\mathbf{b}$ ), the line vector ( $\mathbf{l}$ ) and the normal vector of the slip plane ( $\mathbf{n}$ ) of the dislocations. The contrast factors of dislocations characterize the “visibility” of dislocations in the diffraction experiments. For example if  $\mathbf{bg} = 0$  for a dislocation, it has no, or almost no broadening effect on the line profile. While the contrast factors can be determined experimentally for single crystals, in a polycrystalline sample only the averages of  $C$  can be observed. For these type of materials, strain anisotropy can be well accounted for by the average contrast factors of dislocations. See for example the *modified* Williamson-Hall plot (Ungár & Borbély, 1996) in Fig. 3.2.

It has been shown by Ungár & Tichy (1999) that if the specimen is either untextured or if all possible slip systems are equally populated, the average contrast factors can be expressed by the fourth order polynomials of the  $hkl$  indices. For cubic crystals (Ungár & Tichy, 1999):

$$\bar{C} = C_{h00}(1 - qH^2), \quad (2.61)$$

where

$$H^2 = \frac{h^2k^2 + h^2l^2 + k^2l^2}{(h^2 + k^2 + l^2)^2}. \quad (2.62)$$

For hexagonal crystals (Ungár & Tichy, 1999):

$$\bar{C} = C_{hk0}(1 + a_1H_1^2 + a_2H_2^2), \quad (2.63)$$

where

$$H_1^2 = \frac{[h^2 + k^2 + (h+k)^2]l^2}{[h^2 + k^2 + (h+k)^2 + \frac{3}{2}(\frac{a}{c})^2l^2]^2},$$

$$H_2^2 = \frac{l^4}{[h^2 + k^2 + (h+k)^2 + \frac{3}{2}(\frac{a}{c})^2l^2]^2}, \quad (2.64)$$

and  $\frac{a}{c}$  is the ratio of the two lattice constants.

For orthorhombic crystals (Ungár & Tichy, 1999):

$$\bar{C}_{hkl} = C_{h00} (H_0^2 + a_1H_1^2 + a_2H_2^2 + a_3H_3^2 + a_4H_4^2 + a_5H_5^2), \quad (2.65)$$

where

$$\begin{aligned}
 H_0^2 &= \frac{\frac{h^4}{a^4}}{\left(\frac{h^2}{a^2} + \frac{k^2}{b^2} + \frac{l^2}{c^2}\right)^2}, \\
 H_1^2 &= \frac{\frac{k^4}{b^4}}{\left(\frac{h^2}{a^2} + \frac{k^2}{b^2} + \frac{l^2}{c^2}\right)^2}, \\
 H_2^2 &= \frac{\frac{l^4}{c^4}}{\left(\frac{h^2}{a^2} + \frac{k^2}{b^2} + \frac{l^2}{c^2}\right)^2}, \\
 H_3^2 &= \frac{\frac{h^2 k^2}{a^2 b^2}}{\left(\frac{h^2}{a^2} + \frac{k^2}{b^2} + \frac{l^2}{c^2}\right)^2}, \\
 H_4^2 &= \frac{\frac{l^2 h^2}{c^2 a^2}}{\left(\frac{h^2}{a^2} + \frac{k^2}{b^2} + \frac{l^2}{c^2}\right)^2}, \\
 H_5^2 &= \frac{\frac{k^2 l^2}{b^2 c^2}}{\left(\frac{h^2}{a^2} + \frac{k^2}{b^2} + \frac{l^2}{c^2}\right)^2}.
 \end{aligned} \tag{2.66}$$

Here it is noted that a formally similar equation to (2.61) has been derived for random displacement of atoms in elastically anisotropic cubic crystals by Stokes & Wilson (1944). However, it has not been evaluated until Ungár and Tichy (1999) have rediscovered and further evaluated the correlation between dislocations and strain anisotropy.

The constants  $C_{h00}$  and  $C_{hk0}$  are calculated on the basis of the crystallography of dislocations and from the elastic constants of the crystal (see: Ungár et al, 1999). The parameters  $q$ ,  $a_1, a_2, \dots, a_5$  are the same for all reflections. These parameters are related to the edge or screw character of the dislocations. In Ungár et al. (1999) the value of these contrast factor parameters were calculated for different materials and for different type of dislocations. For example the  $q$  parameter were calculated and plotted as a function of the  $A_Z$  Zener constant for pure edge and pure screw dislocations. The Williamson-Hall, MWP or CMWP procedure provide a measured value of the  $q$  parameter, which usually falls between the values of the  $q$  parameter calculated for edge or screw dislocations. If the value of the measured  $q$  parameter is close to the  $q$  value calculated for edge dislocations, then the character of the dislocations is edge, if it is close to the  $q$  value calculated for screw dislocations, then the character is screw and if its value is close to the average of the edge and screw  $q$  values, then the character of dislocations is mixed. One can see from eq. (2.59) that the diffraction order dependence of the strain Fourier–transform is given by  $g^2 C$ . A numerical code (the ANIZC program) has been developed by Dr. Borbély (2003) for the calculation of the individual or average contrast factors taking into account the elastic constants of the material, the lattice parameters and the relative orientations of the  $\mathbf{l}$ ,  $\mathbf{b}$ ,  $\mathbf{n}$  and  $\mathbf{g}$  vectors. In addition to X-ray line profile analysis, the theory of dislocation contrast factors can also be applied successfully for evaluating neutron diffraction experiments (see e.g. Somogyvári et al., 2001).

### 2.3.3 The Groma-Csikor strain function

The logarithmic approximation of the strain function for small  $L$  values given by eq. (2.56) was determined by several authors: Krivoglaz (1969) and Wilkens (1970) derived it for special dislocation distributions and Groma (1998) proved its validity for a general distribution of dislocations. This means an intensity profile which decays asymptotically as  $\frac{1}{s^3}$  (Groma, 1998).

Gaál (1984) determined the (complex) strain Fourier transform of a random configuration of polarised screw dislocation dipoles. Groma & Monnet (2002) calculated  $A(L)$  corresponding to a distribution of infinitesimal polarised dislocation dipoles and derived a negative exponential function for the strain Fourier transform. The strain Fourier transform calculated by Wilkens (1970) has the same asymptotic behaviour for large  $L$  values. This means a Lorentzian intensity profile.

Groma and Csikor proposed a simple interpolation function which connects smoothly these two functions (Groma, 2003; Csikor & Groma, 2004):

$$\langle \varepsilon_{\mathbf{g},L}^2 \rangle = \left( \frac{b}{2\pi} \right)^2 \pi C^{hkl} f^{GR-CS}(L), \quad (2.67)$$

where:

$$f^{GR-CS}(L) = W \log \left( 1 + \frac{X}{|L|} \right) + \frac{Y}{1 + ZL^2}, \quad (2.68)$$

and  $W$ ,  $X$ ,  $Y$  and  $Z$  are parameters of the function. Actually the authors have derived this formula for the  $P(\tau)$  distribution function of the internal stresses caused by dislocations, which is analogous to the  $I(s)$  intensity distribution used in X-ray line profile analysis.

For  $L \rightarrow 0$  this function tends to:  $W \log \frac{X}{|L|} + Y$  and by comparing the expression of  $\langle \varepsilon_{\mathbf{g},L}^2 \rangle$  to that given by Krivoglaz (2.57) the following equation is obtained for  $\rho^{disl.}$ , the dislocation density, and  $R_e$ , the effective outer cut-off radius of dislocations:

$$W \log \frac{X}{|L|} + Y = C_{h00}^{disl.} \rho^{disl.} \log \frac{R_e}{|L|} \quad (2.69)$$

For  $L \rightarrow \infty$  the function takes the form:

$$WX \frac{1}{|L|} + \left( -\frac{WX^2}{2} + \frac{Y}{Z} \right) \frac{1}{L^2}. \quad (2.70)$$

Since the profile function is area normalised, in other words  $A(0) = 1$ , the second term should disappear:

$$\left( -\frac{WX^2}{2} + \frac{Y}{Z} \right) = 0. \quad (2.71)$$

This means, that the strain function depends only on three independent parameters, therefore one of the four parameters can be eliminated, e.g.:  $Z = \frac{2Y}{WX^2}$ .

The first term in eq. (2.70) can be compared to the following expression depending on  $a^{dip.}$ , the dipole distance and on  $\rho^{dip.} = \frac{\rho^{disl.}}{2}$ , the density of dislocation dipoles:

$$WX \frac{1}{|L|} = C_{h00}^{dip.} a^{dip.} \rho^{dip.} \frac{1}{|L|} \quad (2.72)$$

From these equations, the following expressions are obtained for the values of the physical parameters ( $C_{h00}^{disl.}$  and  $C_{h00}^{dip.}$  are the dislocation and dipole contrast factors, respectively):

$$\rho^{disl.} = \frac{W}{C_{h00}^{disl.}}, \quad (2.73)$$

$$R_e = X \exp\left(\frac{Y}{W}\right), \quad (2.74)$$

$$a^{dip.} = \frac{C_{h00}^{disl.}}{C_{h00}^{dip.}} 2X, \quad (2.75)$$

$$\rho^{dip.} = \frac{W}{2C_{h00}^{dip.}}. \quad (2.76)$$

It is noted that the Groma-Csikor strain function is implemented in the CMWP program package [S14], however it is not always possible to determine so many strain parameters from the measurements, especially if size broadening is also present. In some cases, e.g. if the quality of the measured data is low, or if the tails of the profiles cannot be measured because of the strong overlapping between peaks, it is even not possible to determine  $\rho$  and  $R_e^*$  accurately.

Eq. (2.68) provides a simple and flexible strain function, which can also be used to approximate the Wilkens function if less independent parameters are used, e.g. by writing eq. (2.68) in the form  $f^{GR-CS^*}(\eta) = W \log\left(1 + \frac{X}{|\eta|}\right) + \frac{Y}{1 + Z\eta^2}$ , where  $\eta = \frac{1}{2} \exp\left(-\frac{1}{4}\right) \frac{L}{R_e^*}$ , the parameters  $W$ ,  $X$ ,  $Y$  and  $Z$  can be determined by fitting these parameters to the data points of the  $f^*(\eta)$  Wilkens function. The resulting function gives a perfect description of the Wilkens function, see the graphs of the fitted  $f^{GR-CS^*}(\eta)$  function and the Wilkens function in Fig. 2.12 (also cf. Fig. 2.9). The fitting provided the following parameters:  $W = 1.14908$ ,  $X = 1.4125$ ,  $Y = 0.212226$  and the value of  $Z$  is  $\frac{2Y}{WX^2} = 0.18514$ . By using these parameters a good approximation of the Wilkens function is obtained which is even simpler than the following approximate formula given by van Berkum (1994):

$$f^*(\eta) = -\log \eta + \left(\frac{7}{4} - \log 2\right) + \frac{\eta^2}{6} - \frac{32\eta^3}{225\pi} \quad \text{if } \eta \leq 1, \quad (2.77)$$

$$f^*(\eta) = \frac{256}{45\pi} \frac{1}{\eta} - \left[\frac{11}{24} + \frac{1}{4} \log 2\eta\right] \frac{1}{\eta^2}, \quad \text{if } \eta \geq 1.$$

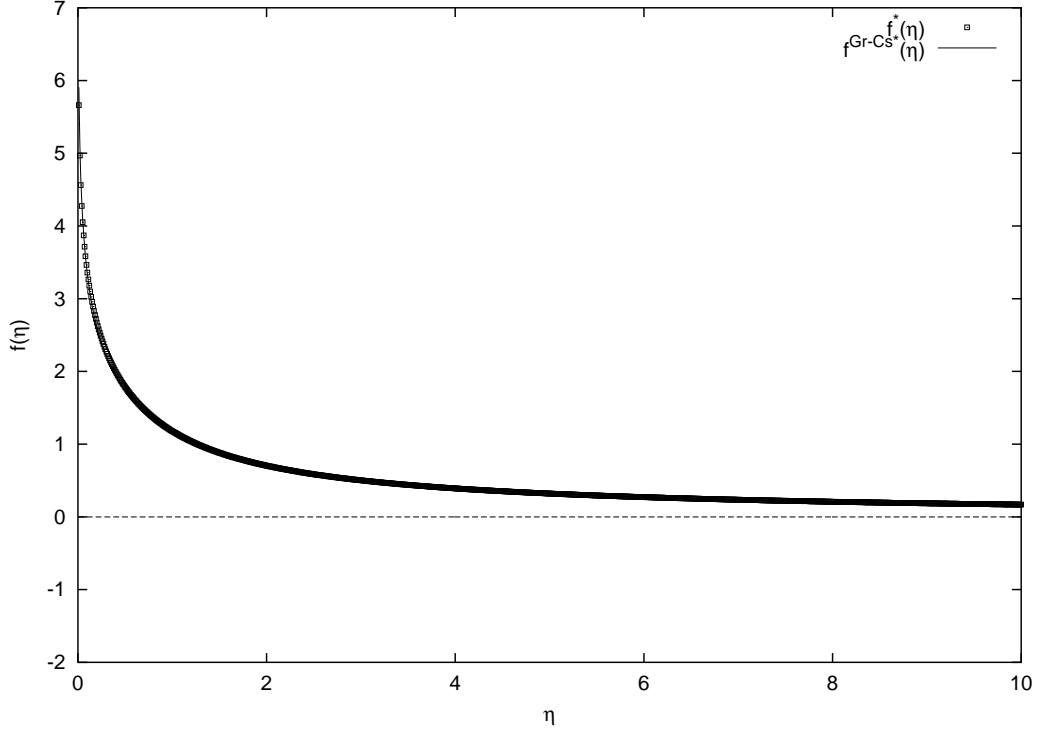


Figure 2.12:  $f^*(\eta)$ , the Wilkens function (where  $\eta = \frac{1}{2} \exp\left(-\frac{1}{4}\right) \frac{L}{R_e^*}$ ) and  $f^{GR-CS*}$ , the Groma-Csikor strain function fitted to the data points of the Wilkens function. The fitting provided the following parameters of the Groma-Csikor strain function:  $W = 1.14908$ ,  $X = 1.4125$ ,  $Y = 0.212226$  and  $Z = \frac{2Y}{WX^2} = 0.18514$ . This strain function gives a perfect approximation of the Wilkens function.

## 2.4 Planar faults [S18]

According to the numerical calculations of Mr. Levente Balogh, based on the theoretical work of Warren (1969) and the numerical code developed by Treacy et al. (1991), the peak broadening due to stacking faults for an  $hkl$  reflection in cubic fcc crystals can be expressed in the following form:

$$I^{st}(s) = p_0^{hkl} \delta(s) + \frac{p_1^{hkl}}{1 + \left(\frac{s - s_1^{hkl}}{w_1^{hkl}}\right)^2} + \frac{p_2^{hkl}}{1 + \left(\frac{s - s_2^{hkl}}{w_2^{hkl}}\right)^2} + \frac{p_3^{hkl}}{1 + \left(\frac{s - s_3^{hkl}}{w_3^{hkl}}\right)^2}, \quad (2.78)$$

where the first term is given by a Dirac delta function, the others are broadened and shifted Lorentzian functions,  $w_i^{hkl}$  are the FWHM values of the Lorentzian functions and  $s_i^{hkl}$  are the shifts of the Lorentzian functions. Both  $w_i^{hkl}$  and  $s_i^{hkl}$  can be expressed as fifth order polynomials of the  $\alpha_j$  probability of planar faults, where  $j$  stands for intrinsic or extrinsic stacking faults or twin boundaries:

$$w_1^{hkl} = W_{1,1}^{hkl} \alpha_j + W_{1,2}^{hkl} \alpha_j^2 + W_{1,3}^{hkl} \alpha_j^3 + W_{1,4}^{hkl} \alpha_j^4 + W_{1,5}^{hkl} \alpha_j^5, \quad (2.79)$$

$$w_2^{hkl} = W_{2,1}^{hkl} \alpha_j + W_{2,2}^{hkl} \alpha_j^2 + W_{2,3}^{hkl} \alpha_j^3 + W_{2,4}^{hkl} \alpha_j^4 + W_{2,5}^{hkl} \alpha_j^5, \quad (2.80)$$

$$w_3^{hkl} = W_{3,1}^{hkl} \alpha_j + W_{3,2}^{hkl} \alpha_j^2 + W_{3,3}^{hkl} \alpha_j^3 + W_{3,4}^{hkl} \alpha_j^4 + W_{3,5}^{hkl} \alpha_j^5, \quad (2.81)$$

$$s_1^{hkl} = S_{1,1}^{hkl} \alpha_j + S_{1,2}^{hkl} \alpha_j^2 + S_{1,3}^{hkl} \alpha_j^3 + S_{1,4}^{hkl} \alpha_j^4 + S_{1,5}^{hkl} \alpha_j^5, \quad (2.82)$$

$$s_2^{hkl} = S_{2,1}^{hkl} \alpha_j + S_{2,2}^{hkl} \alpha_j^2 + S_{2,3}^{hkl} \alpha_j^3 + S_{2,4}^{hkl} \alpha_j^4 + S_{2,5}^{hkl} \alpha_j^5, \quad (2.83)$$

$$s_3^{hkl} = S_{3,1}^{hkl} \alpha_j + S_{3,2}^{hkl} \alpha_j^2 + S_{3,3}^{hkl} \alpha_j^3 + S_{3,4}^{hkl} \alpha_j^4 + S_{3,5}^{hkl} \alpha_j^5. \quad (2.84)$$

The real and imaginary parts of the  $A^{st}(L)$  Fourier transform of  $I^{st}(s)$  can be expressed as:

$$\begin{aligned} \Re A^{st}(L) = & p_0^{hkl} + p_1^{hkl} \cos(2\pi s_1^{hkl} L) \exp(-\pi w_1^{hkl} L) + p_2^{hkl} \cos(2\pi s_2^{hkl} L) \exp(-\pi w_2^{hkl} L) + \\ & + p_3^{hkl} \cos(2\pi s_3^{hkl} L) \exp(-\pi w_3^{hkl} L) \end{aligned} \quad (2.85)$$

$$\begin{aligned} \Im A^{st}(L) = & p_1^{hkl} \sin(2\pi s_1^{hkl} L) \exp(-\pi w_1^{hkl} L) + p_2^{hkl} \sin(2\pi s_2^{hkl} L) \exp(-\pi w_2^{hkl} L) + \\ & + p_3^{hkl} \sin(2\pi s_3^{hkl} L) \exp(-\pi w_3^{hkl} L). \end{aligned} \quad (2.86)$$

It is noted, that since this Fourier transform is complex, the intensity profile (obtained by inverse Fourier transforming this expression) is asymmetric. For each type of materials and stacking faults, the values of  $p_i^{hkl}$ ,  $S_{i,j}^{hkl}$  and  $W_{i,j}^{hkl}$  are determined for different  $hkl$  values by using the program DIFFAX developed by Treacy et al. (1991). The  $p_i^{hkl}$ ,  $S_{i,j}^{hkl}$  and  $W_{i,j}^{hkl}$  parameter values have been evaluated for fcc crystals for the first 15 reflections and for the three fundamental planar fault types by Mr. Levente Balogh [S18].

# Chapter 3

## The classical methods of X-ray line profile analysis

This chapter is a summary of the methods of X-ray line profile analysis developed by other authors. The information about the microstructure is in the width and the shape of the diffraction profiles. Therefore the methods of X-ray line profile analysis can be divided into two main groups: (i) breadth methods and (ii) whole profile or pattern fitting methods. A brief summary is given for the Williamson-Hall breadth method and the Warren-Averbach Fourier procedure. The so called full-profile and whole-pattern methods of other authors and the moment-methods are shortly discussed.

### 3.1 Breadth methods

The Williamson-Hall procedures are based on the different order dependence of the different physical effects causing the broadening of diffraction profiles. In the case of spherical crystallites the size broadening of profiles is constant and isotropic in the whole reciprocal space, while strain broadening increases with  $K$ , the reciprocal space coordinate. If strain is caused by dislocations, the strain broadening is usually anisotropic and can be interpreted by the concept of dislocation contrast (or orientation) factors (Ungár & Borbély, 1996; Ungár & Tichy, 1999). If planar or stacking faults are present, the broadening is also anisotropic, however it does not increase with  $K$ . Here it is noted that anisotropic crystallite shape can also introduce anisotropy in the broadening ([S4, S6, S5]; Scardi & Leoni, 2002).

In the *Williamson-Hall procedure* (Williamson & Hall, 1953), the  $\Delta K$  values defined as the FWHMs (a) or integral breadths (b) of the measured profiles are plotted as a function of  $K$ . This is called the Williamson-Hall plot. Such a plot gives a qualitative idea about the causes of peak broadening: if the sample consists of small crystallites, the  $\Delta K$  value at  $K = 0$  is high, while if the crystallites are large, this value is negligible or small. Since at  $K = 0$  no strain broadening is present, the corresponding  $\Delta K$  value is due only to size broadening and according to eqs. (2.12) and (2.13) this  $\Delta K$  value is equal to  $\frac{0.9}{D}$  (a) or  $\frac{1}{d}$  (b), respectively. Here it is noted that this value can only be determined by extrapolation

from the measured data points, since there is no Bragg peak at  $K = 0$ .

The slope of the curve gives qualitative information on the strength of the strain effect. If the effect is strong,  $\Delta K$  increases strongly with  $K$ , while if the strain is weak, the  $\Delta K$  values are almost constant or the slope is small. In order to estimate the dislocation density, the slope can also be interpreted quantitatively, however it is better to use the Warren-Averbach (Warren & Averbach, 1952) method (or a more advanced full profile fitting procedure, see e.g. the methods described in Chapters 4 and 5) for this purpose.

If strain is caused by dislocations, the widths of peaks show a typical anisotropic behaviour (see for example for deformed polycrystalline copper sample Fig. 3.1) and the *modified* Williamson-Hall procedure (Ungár & Borbély, 1996) can be used to interpret strain in terms of dislocation contrast factors. In this procedure the widths are plotted as a function of  $K\sqrt{C}$  or  $K^2C$  leading to a considerably smoother curve for materials containing dislocations, see for the same deformed polycrystalline copper sample Fig. 3.2. The strain anisotropy parameters can be determined by using a simple linear regression procedure. In previous papers (e.g. Ungár & Borbély, 1996), it is suggested that the widths depend quasi-linearly on  $K\sqrt{C}$ . In recent papers [S4, S6], it is suggested that the widths depend quasi-linearly on  $K^2C$ . This is based on the Wilkens model (Wilkens, 1970), which is a very powerful model for describing the strain properties of materials containing dislocations. The Wilkens strain profile depend only on the powers of  $K^2C$ , so it is an even function of  $K\sqrt{C}$ , therefore the widths (FWHM or integral breadth values) of the peak profiles are also even function of  $K\sqrt{C}$ . As long as the basic assumptions of the Wilkens model are suitable for the investigated materials, the widths can depend only on  $K^2C$  and not on  $K\sqrt{C}$ . The modified Williamson-Hall plots have been plotted as a function of  $K^2C$  for several materials, and it has been found that the data can be very well fitted linearly as a function of  $K^2C$ . For a demonstration, see for example Fig. 3.3 for the same deformed polycrystalline copper sample as plotted in Figs. 3.1 and 3.2. However there is no guarantee that the assumptions of the Wilkens model are always satisfied and for some particular sample a linear dependence on  $K\sqrt{C}$  is also conceivable. The Williamson-Hall methods use only the widths of the profiles which is a very limited portion of the information in the profiles. However, these simple and powerful methods are well suitable to qualitatively investigate the materials.

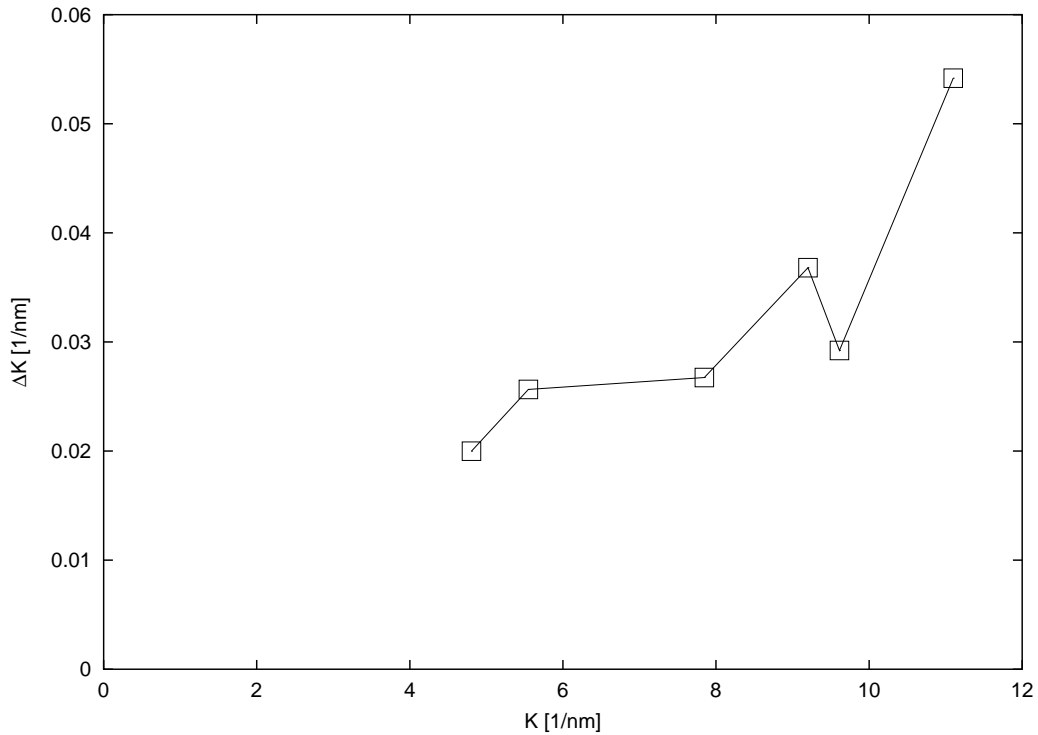


Figure 3.1: Classical Williamson-Hall plot for the integral breadths (deformed polycrystalline copper sample). In this figure the  $\beta$  values are plotted as a function of  $K$ .

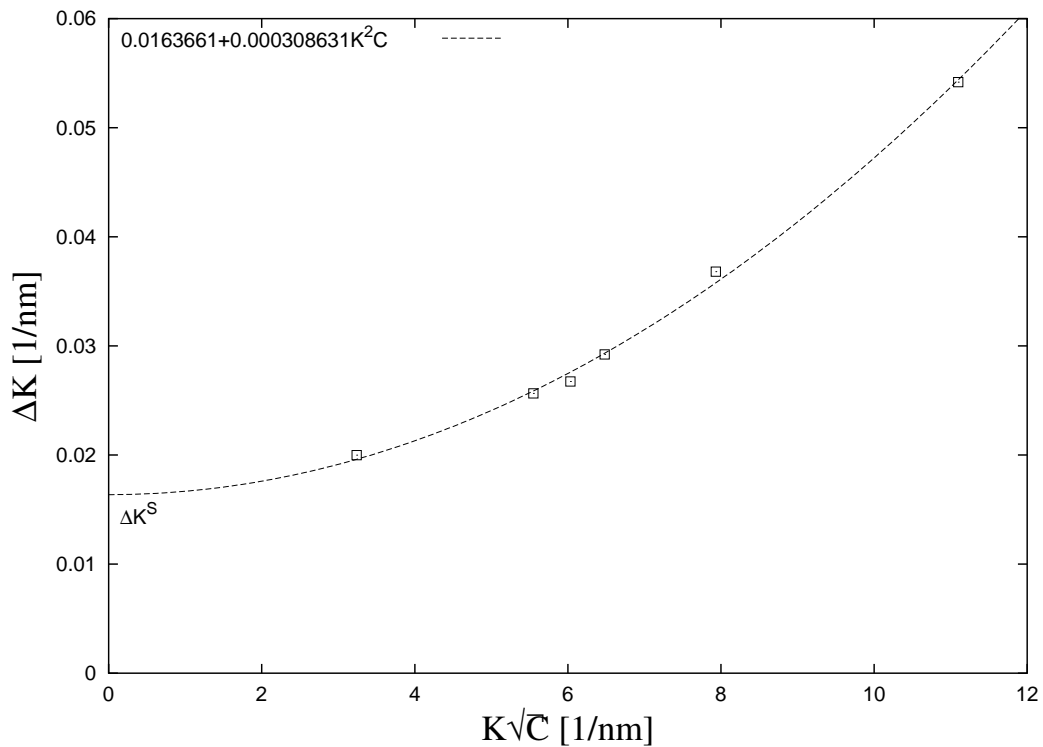


Figure 3.2: *Modified* Williamson-Hall plot for the integral breadths (deformed polycrystalline copper sample). In this figure the  $\beta$  values are plotted as a function of  $K\sqrt{C}$ . The data points are fitted by a parabolic curve, the fitted parameters of the parabola are also indicated. The value of the fitted function at  $K = 0$ ,  $\Delta K^S$  is the breadth of the pure size function.

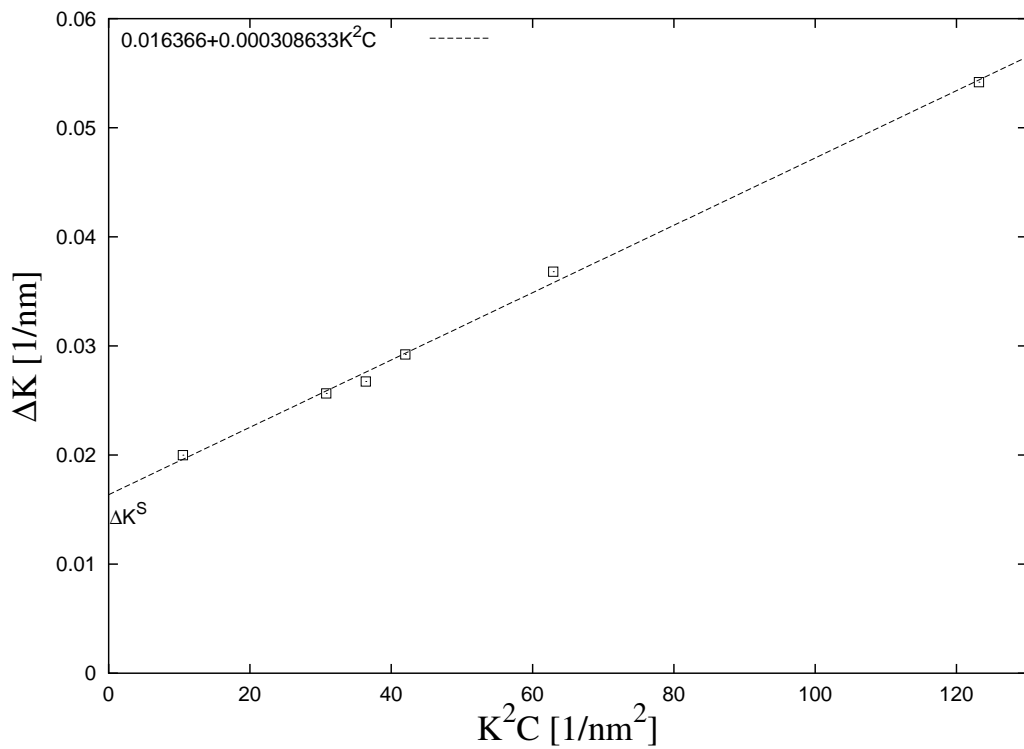


Figure 3.3: *Modified Williamson-Hall plot for the integral breadths (deformed polycrystalline copper sample). In this figure the  $\beta$  values are plotted as a function of  $K^2C$ . The data points are fitted by a straight line, the fitted parameters of the line are also indicated. The value of the fitted function at  $K = 0$ ,  $\Delta K^S$  is the breadth of the pure size function.*

## 3.2 Fourier methods

In the *Warren-Averbach procedure*, the Fourier transforms of the profiles are analysed. In the classical *Warren-Averbach plot* (Warren & Averbach, 1952) the normalized Fourier transforms of the measured peak profiles are calculated for equidistantly sampled values of  $L$  in a range  $[0, L_{\max}]$  and  $\log A(L)$  is plotted as a function of  $K^2$  for each  $L$  value. The Warren-Averbach plot shows usually a similar anisotropic behaviour as the Williamson-Hall plot. In the *modified* Warren-Averbach plot, the measured data points can be plotted smoothly as a function of the scaling parameter  $K^2C$ . It is demonstrated in Figs. 3.4 and 3.5.

The values of the physical parameters can be determined as follows. Using eqs. (2.50), (2.51) and (2.56), for small values of  $L$ , the logarithm of the Fourier transform of the profiles can be approximated as:

$$\log A(L) \approx \log A^S(L) - \rho B L^2 \log \left( \frac{R_e}{L} \right) (K^2 C), \quad (3.1)$$

where  $B = \frac{\pi b^2}{2}$ . In this method, the parameters in the contrast factors are not fitted, but are fixed to particular values (obtained for example by the modified Williamson-Hall procedure).

For each value of  $L_i$ ,  $\log A(L_i)$  is fitted by the parabolic curve  $a_i + b_i K^2 C + c_i K^4 C^2$  and by plotting the exponential of the  $a_i$  values as a function of  $L$ , the *size* Fourier transform is obtained. By fitting the initial slope of the size Fourier transform (using linear regression) one can get the value of  $L_0$ , see Fig. 3.6.

The initial slopes  $b_i$  divided by  $L_i^2$  are plotted as a function of  $\log L_i$ , as shown in Fig. 3.7. By using linear regression on the linear part of this data, the initial slope is equal to  $\rho B$ , from which the dislocation density,  $\rho$ , can be determined. The other parameter of the regression line is equal to  $-\rho B \log R_e$  from which the value of  $R_e$  can be determined.

The applicability of this method is limited by the fact that in some cases when plotting  $\frac{b_i}{L_i^2}$  as a function of  $\log L_i$ , the curve has no linear part (the logarithmic formula is not valid for larger  $L$  values and even for small values of  $L$  for materials containing dislocations a “hook-effect”, a deviation from the logarithmic function can be observed, see e.g. Wilkens, 1970), so the determination of  $\rho$  and  $R_e$  becomes very unstable.

When fitting  $\log A(L_i)$ , the term  $c_i K^4 C^2$  indicates the presence of a higher order term in  $\langle \epsilon_{\mathbf{g},L}^2 \rangle$ . This term is used only for describing the curve more accurately, the value of  $c_i$  is not used at all.

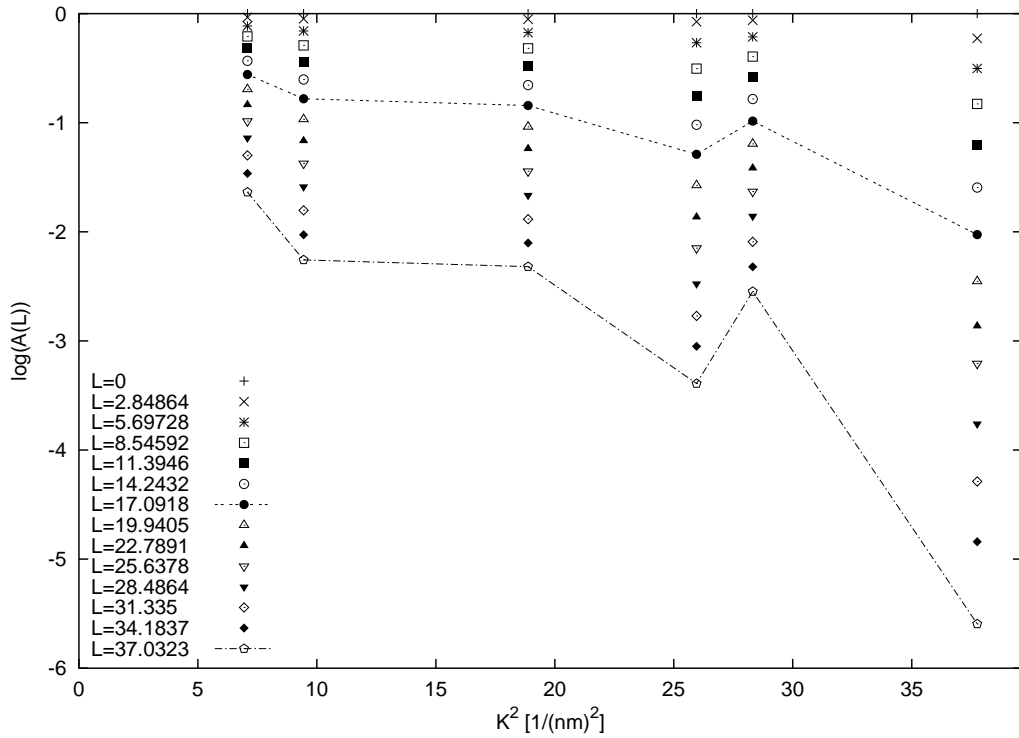


Figure 3.4: Warren-Averbach plot (deformed polycrystalline copper sample). In this figure  $\log A(L)$  is plotted as a function of  $K^2$  for each  $L$  value. The anisotropic behaviour of the data points can also be observed.

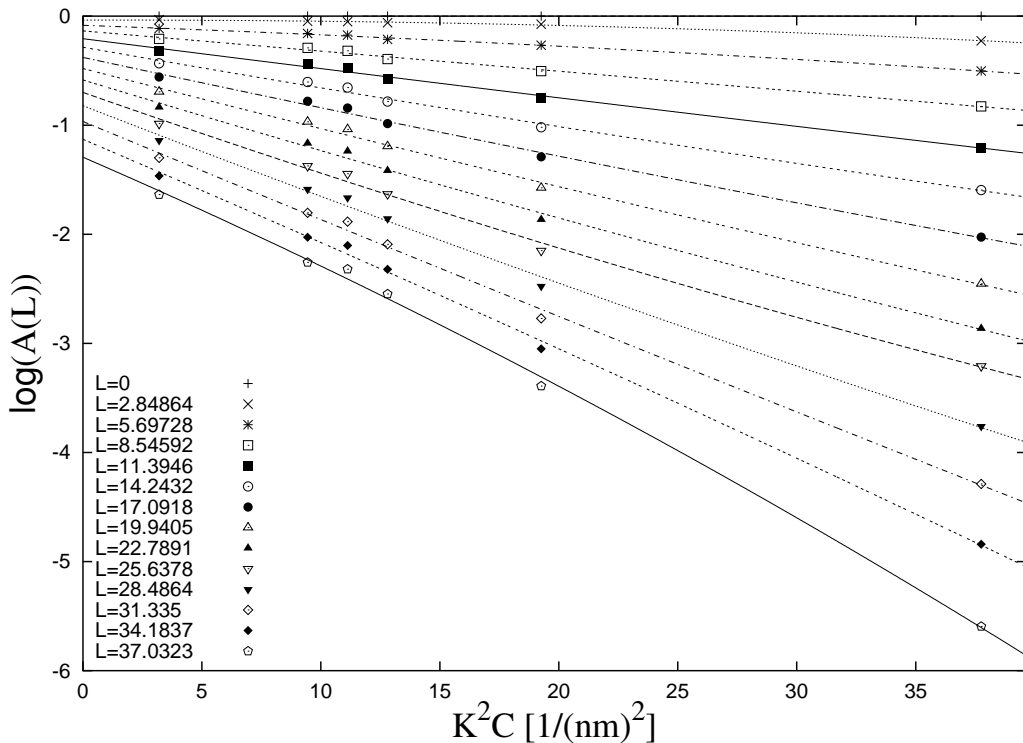


Figure 3.5: Modified Warren-Averbach plot (deformed polycrystalline copper sample). In this figure  $\log A(L)$  is plotted as a function of  $K^2 C$  for each  $L$  value. The data points are fitted by parabolic curves, which are also plotted. The  $\log A(L)$  values at  $L = 0$  correspond to the pure size Fourier transform.

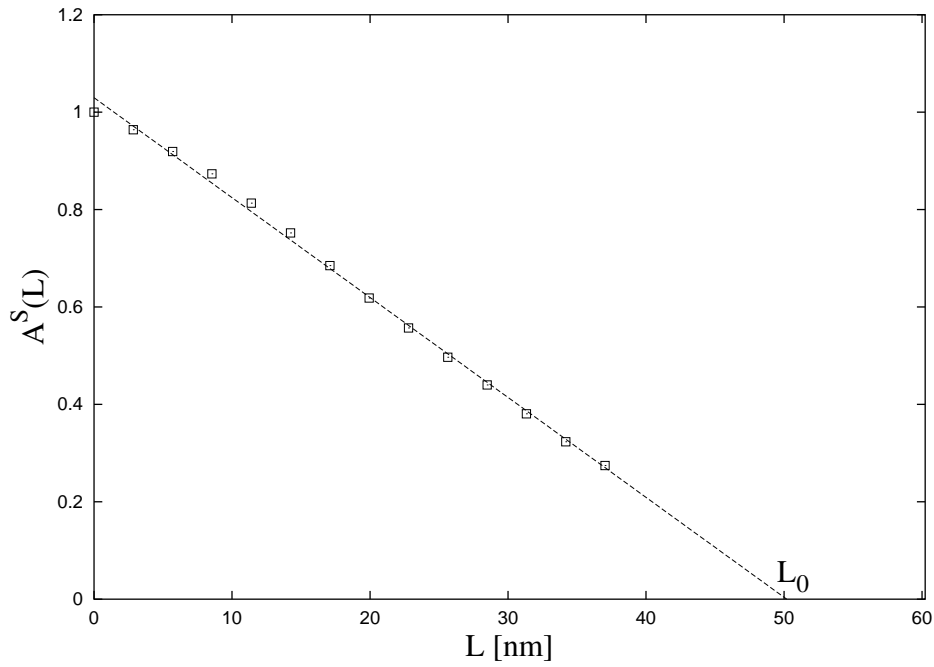


Figure 3.6: The size Fourier Transform obtained by the *modified* Warren-Averbach method (deformed polycrystalline copper sample). In this figure the  $A^S(L)$  values, the values of the size Fourier transform, are plotted as a function of  $L$ . The data points are fitted by a line and the  $L$  value of this line corresponding to  $A^S(L) = 0$  is the parameter  $L_0$ .

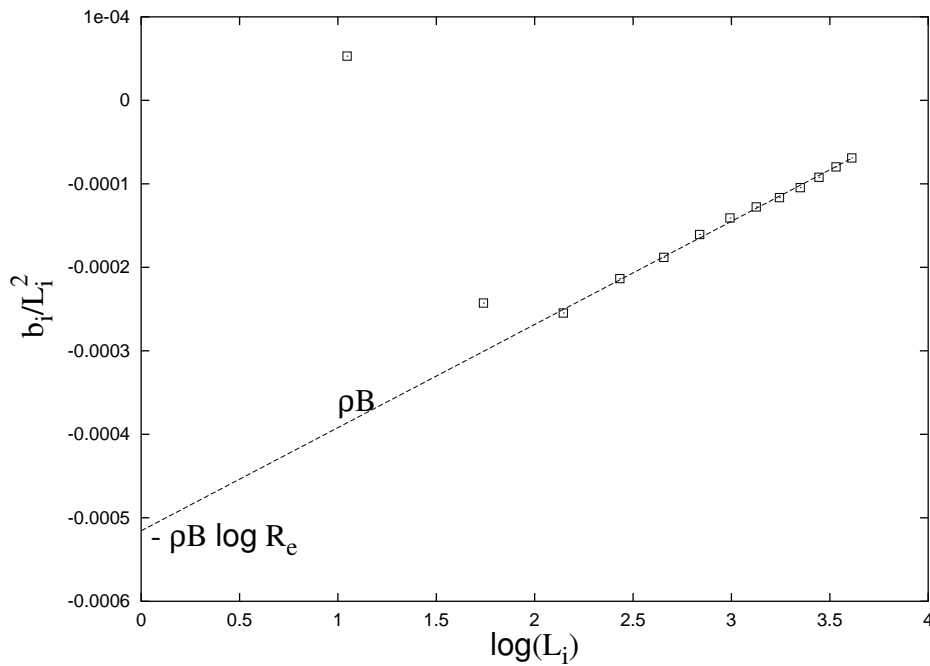


Figure 3.7: The plot for determining  $\rho$  and  $R_e$  by using the *modified* Warren-Averbach method (deformed polycrystalline copper sample). In this figure the  $\frac{b_i}{L_i^2}$  values are plotted as a function of  $\log(L_i)$ . The linear part of the data points is fitted by a line and the slope of this line gives the value of  $\rho$  and the  $\frac{b}{L^2}$  value of this line at  $L = 0$  gives the parameter  $R_e$ .

### 3.3 Full profile fitting methods

Instead of the breadth methods, whole profile methods have been developed recently for the determination of microstructural parameters. In Chapter 4 the Multiple Whole Profile (MWP) fitting method [S4, S6] will be presented in detail, which is in fact a Fourier method working on the whole (Fourier) profiles. In the MWP method the Fourier transforms of the measured profiles for all reflections are fitted simultaneously with ab-initio theoretical functions. Its theoretical basis for including the effect of size and strain simultaneously is the convolutional equation (2.50) given by Warren & Averbach (1952). According to the literature, some of the full profile methods other than the MWP method are briefly presented here:

1. Nusinovici & Rehfeldt-Osierski (1990) developed the program PROFILE which uses a method called pattern decomposition. By using this program one can determine interactively line profile parameters by fitting the measured peaks or clusters of peaks with analytical functions. The following analytical functions have been incorporated in their program: Voigt, pseudo-Voigt and Pearson VII.
2. Louer & Audebrand (1999) developed the program *ProfFOU*. In their method all reflections are fitted simultaneously by using pseudo-Voigt functions. The microstructural parameters can be determined by analysing the parameters of the pseudo-Voigt functions.
3. Dong & Scardi (1999) developed a similar program, called *MarqX* which also provides individual profile parameters.
4. A similar approach is the method of Whole Powder Pattern Fitting (WPPF) developed by Scardi and Leoni (1999). In this method an analytical function (e.g. a Voigtian) is adopted to fit the experimental profiles and the profile parameters are connected by suitable conditions (Gaussian and Lorentzian widths in the case of a Voigtian profile function) to the microstructural parameters.

It is noted, that unlike these methods, the MWP method does not provide individual profile parameters, the microstructural parameters for size and strain effect are obtained directly from the fitting procedure which is using ab-initio theoretical profile functions depending only on the microstructural parameters.

### 3.4 Pattern fitting methods

As discussed in the previous section, most of the earlier whole profile fitting methods are based on fitting the measured profiles by analytical profile functions. The most common fitting functions are the Voigt, the pseudo-Voigt and the Pearson VII profile functions which are scaled to the *hkl* anisotropy by ad-hoc scaling parameters, as suggested by Caglioti et al. (1958). These procedures have several deficiencies: (i) the analytical profile functions usually do not describe the physical

profiles correctly over the entire intensity range, they either fit around the maxima or in the tail regions, but usually do not fit well the two regions simultaneously, (ii) there is no unique correlation between the microstructural parameters of the materials and the profile parameters of the analytical functions. Therefore the method of Convolutional Multiple Whole Profile (CMWP) fitting [S14] has been developed in which the profile functions are based and constructed by using fundamental physical principles applied to the different types and kinds of lattice defects. The CMWP method works directly on the measured pattern instead of the Fourier transform of the separated individual profiles (as it was the case in the MWP method). The theoretical basis for including the effect of size and strain simultaneously is the convolutional equation (2.50) given by Warren & Averbach (1952), just like in the case of the MWP method. In the CMWP method, a model based pattern is compared directly to the measured pattern using a nonlinear least squares procedure. As the MWP method, the CMWP method does not need individual peak parameters either, the microstructural parameters are determined directly from the fitting procedure. For the details of the CMWP procedure, see Chapter 5.

In this section a few introductory comments are made about the literature, regarding some of the pattern fitting methods other than the CMWP procedure.

1. Langford et al. (2000) proposed a pattern fitting method for nanocrystalline distortion-free materials. They applied it successfully to the powder pattern of nanocrystalline  $CeO_2$  and the size distribution function has been determined by fitting.
2. Scardi & Leoni (2002) developed a similar procedure which is called Whole Powder Pattern Modeling (WPPM) which uses also ab-initio theoretical functions, but does not account only for the size effect, but also includes theoretical model for several sources of strain. Its theoretical basis for including the size and strain effect simultaneously is also the convolutional equation (2.50) of Warren & Averbach (1952).

### 3.5 Methods analysing the moments of the profiles

These single profile methods are based on the different asymptotic behaviour for the different sources of broadening of the higher order moments of the scattered intensity. The first model was the variance method proposed by Wilson (1962). Borbély and Groma (2001) proposed recently a very powerful momentum method which deals correctly with measurements when both strain and size broadening are present and also the level of the background can be determined in a physically correct way. It uses a general theory for the asymptotic behaviour of dislocation induced X-ray peak broadening, it does not depend on a particular model of dislocation arrangement like the Wilkens model, only the general  $s^{-3}$  dependence of the tails of the intensity profile is used. The size broadening is accounted for by the  $s^{-2}$  dependence of the size profile for the case of small crystallites. Unlike the multi-profile fitting methods, this method can be applied to single profiles, especially for single crystals and the dislocation density can be estimated in this case too. However, in order to evaluate the tails of the

profiles accurately, this method requires the peaks to be measured with good statistics which is not always available.

The  $k$ 'th moment of an intensity profile  $I(s)$  is defined as (Groma, 1998):

$$M_k(s) = \frac{\int_{-\infty}^s S^k I(S) dS}{\int_{-\infty}^{\infty} S^k I(S) dS} \quad (3.2)$$

Borbély & Groma (2001) gave the following asymptotic expansion for the second and fourth order moments:

$$M_2(s) = \frac{1}{\pi^2 \varepsilon_F} s - \frac{L}{4\pi^2 K^2 \varepsilon_F} + \frac{\Lambda \langle \rho \rangle}{2\pi^2} \log\left(\frac{s}{s_0}\right), \quad (3.3)$$

$$\frac{M_4(s)}{s^2} = \frac{1}{3\pi^2 \varepsilon_F} s + \frac{\Lambda \langle \rho \rangle}{4\pi^2} + \frac{3\Lambda^2 \langle \rho^2 \rangle}{4\pi^2} \frac{\log^2\left(\frac{s}{s_1}\right)}{s^2}, \quad (3.4)$$

where  $\Lambda = \frac{\pi}{2} g^2 b^2 C$  and  $\varepsilon_F$  is the area-weighted average crystallite size, for spherical crystallites:  $\varepsilon_F = \frac{3}{2} L_0$ .

By plotting the moments as a function of  $s$  one can readily see the type of broadening present in the experiment and verify if the assumptions of small particle size or the presence of dislocations apply. So, using this method one can easily visualize qualitatively the different sources of broadening as well as the size parameter  $\varepsilon_F$  and the strain parameters  $\langle \rho \rangle$  or  $\langle \rho^2 \rangle$  can be determined quantitatively by a fitting procedure.

An example is presented for ECAP deformed copper sample, the second order moment is plotted in Fig. 3.8 and the fourth order moment divided by  $s^2$  is shown in Fig. 3.9. The moments (calculated by using the measured profile of the 111 reflection) and the fitted theoretical moment functions according to eqs. (3.3) and (3.4) are plotted.

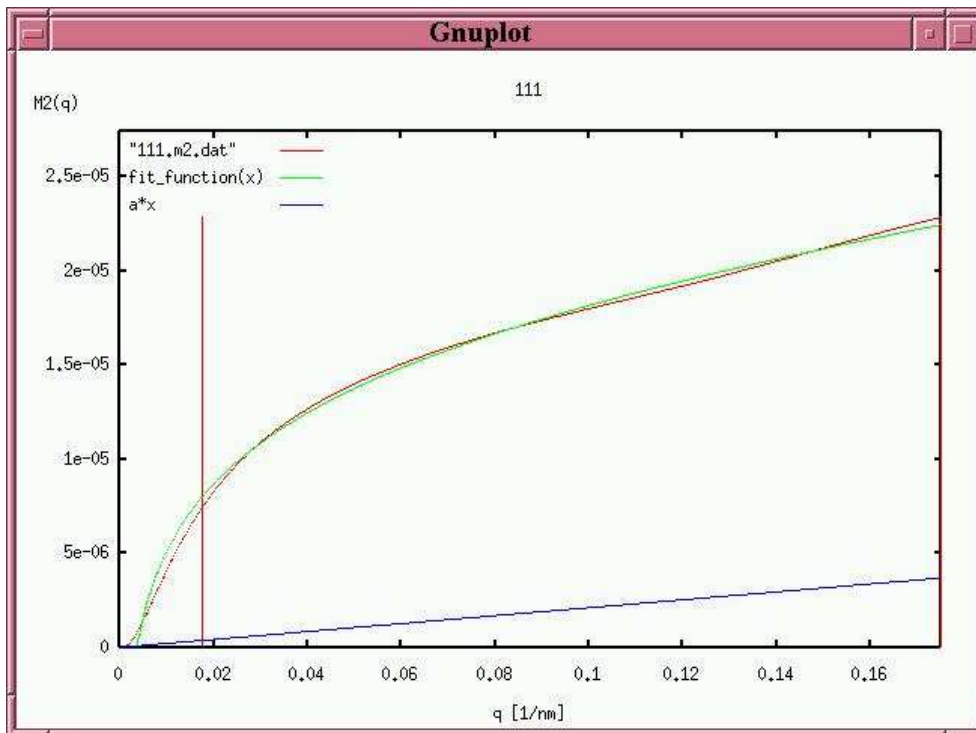


Figure 3.8: The second order moment and the fitted theoretical function (ECAP deformed copper sample). In the figure  $s$  is denoted by  $q$ .

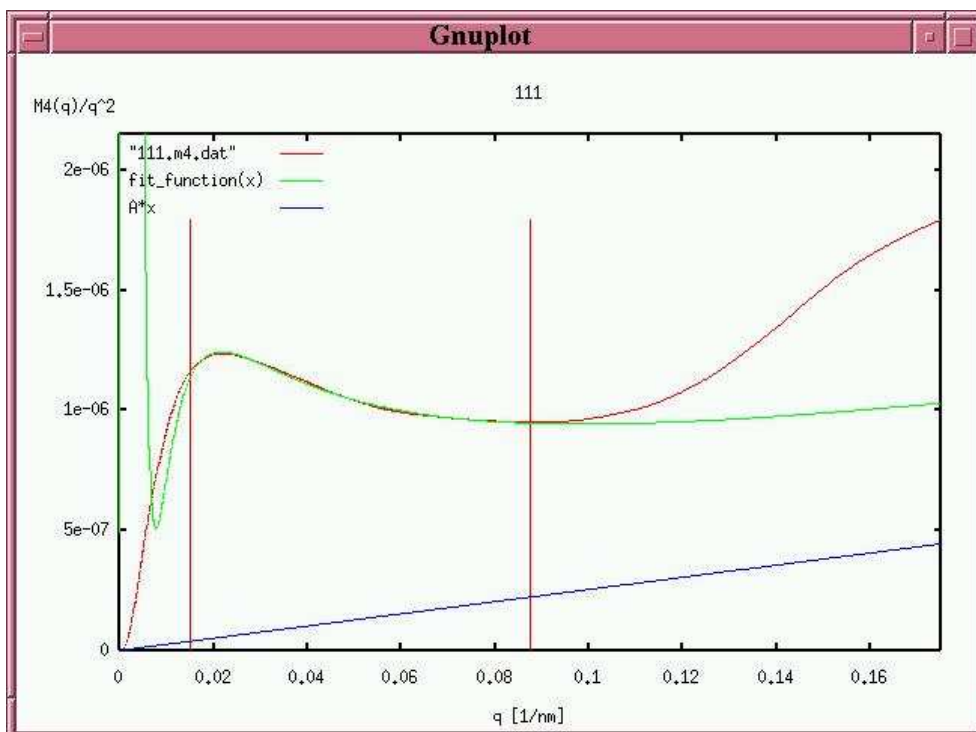


Figure 3.9: The fourth order moment divided by  $s^2$  and the theoretical function fitted between the two markers (ECAP deformed copper sample). In the figure  $s$  is denoted by  $q$ .

# Chapter 4

## Determining microstructure by the Multiple Whole Profile fitting method

The essential parts of this dissertation are the two methods of X-ray line profile analysis: the Multiple Whole Profile (MWP) [S4, S6] and the Convolutional Multiple Whole Profile (CMWP) [S14] fitting procedures. The MWP procedure and a couple of problems solved by this method are described and discussed in detail. It is shown that the MWP method enables to evaluate X-ray diffraction profiles in terms of crystallite size and size distribution and dislocation densities and dislocation character.

### 4.1 The MWP method [S4, S6]

#### 4.1.1 The principles of the method

The aim of the MWP procedure [S4, S6] is to describe the shape and the width of measured profiles on the basis of the microstructure. The microstructural parameters, especially the crystallite size and size distribution, the dislocation density and arrangement parameter and strain anisotropy, are refined by a nonlinear least squares procedure, the Marquardt-Levenberg algorithm (Levenberg, 1944 and Marquardt, 1963). Since it is working on individual profiles, the measured pattern first has to be separated into single diffraction peaks. A special program, called MKDAT, was developed for this separation procedure [S4].

#### 4.1.2 Data preparation: profile separation using the MKDAT program

In the MKDAT procedure the selected overlapping region of the measured intensity pattern is fitted by the sum of a background polynomial and simple analytical functions (Gauss, Lorentz, Pearson VII, Pseudo-Voigt or Voigt). The peak positions, the peak intensities and the shape parameters are fitted by using the nonlinear Marquardt-Levenberg least squares algorithm. For each reflection the sum of the background polynomial and the analytical functions corresponding to the unrequired reflections is subtracted from the measured data and only the peak profile corresponding to the required reflection remains. The parameters of these analytical functions are not interpreted physically, these functions

are used only to describe the shape of the overlapping region. This procedure is correct if the peak shapes are close to the shape of the analytical functions used in the fitting. This may depend on the microstructural properties of the materials, however practice has shown that in most cases these simple analytical functions are adequate to describe the shape of the unrequested measured peaks. This separation procedure should be used only for data preparation and this is not the procedure intended for evaluating the microstructure. If the overlapping between the peaks is weak, the separation procedure is simpler: in this case only the background (represented by a polynomial) is subtracted from the measured data and there is no need for the above mentioned analytical functions, so the data and the results of the MWP evaluation procedure are not influenced by the shape of any analytical function. Fig. 4.1 is an example for the separation of overlapping peaks.

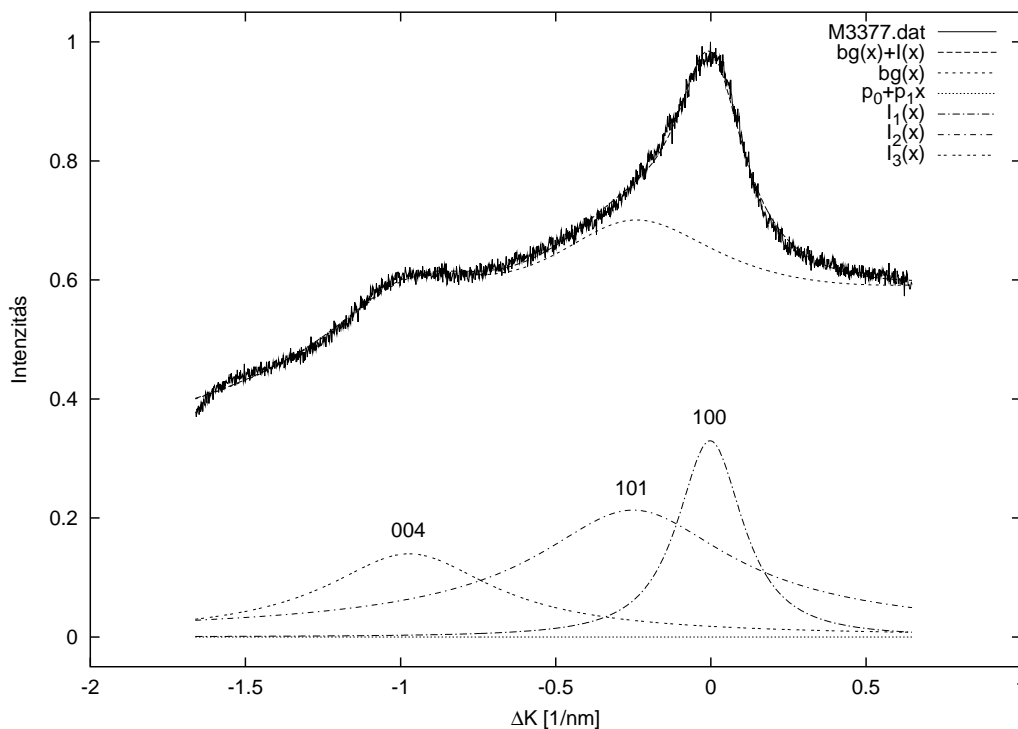


Figure 4.1: Typical example for the separation of strongly overlapping peaks in the case of carbon black sample. The background polynomial is given as  $p_0 + p_1x$  and the measured data are fitted by the function  $p_0 + p_1x + I_1(x) + I_2(x) + I_3(x)$ , where:  $I_1(x)$ ,  $I_2(x)$  and  $I_3(x)$  are Pearson VII functions. For the 100 peak, the peak profile is determined by subtracting  $bg(x)$ , the sum of the background polynomial and the *other* Pearson VII functions (004 and 101) from the *measured* data. After the subtraction, the remaining data correspond to the pure, separated peak. The same procedure can be applied to obtain the other peaks.

### 4.1.3 Data preparation: instrumental deconvolution using the MKDAT program

If instrumental broadening is present, the peaks should be corrected for the instrumental effect too. In the MKDAT program a simple deconvolution (based on the method of Stokes, 1948) is used for

this purpose. In this procedure the Fourier transforms of the measured peak,  $A^m(L)$ , and the Fourier transforms of the corresponding instrumental peak,  $A^i(L)$ , are calculated. By using complex division,  $A^{ph}(L) = \frac{A^m(L)}{A^i(L)}$ , the Fourier transform of the physical and pure microstructural peak profile is calculated. The instrumental free intensity profile can also be determined by calculating the inverse Fourier transform of  $A^{ph}(L)$ .

#### 4.1.4 Evaluation of X-ray diffraction profiles using the MWP program

Since the MWP method is a microstructural method, the peak intensities are not interpreted physically, so the measured intensity profiles and their Fourier-transforms, as well as the fitting theoretical functions are normalized by their maximum values in the fitting procedure.

The theoretical basis of the microstructural analysis is the ab-initio theoretical Fourier-transform given by equations (2.50), (2.58), (2.59), (2.61), (2.64), (2.36) and (2.47)-(2.49). There are two possible approaches:

- (i) **Multiple Whole Profile fitting of the Fourier-transforms.** In this procedure first the *measured* intensity profiles are Fourier-transformed and normalized. Then all of them are fitted simultaneously by the normalized *theoretical* Fourier-transform:

$$A(L) = \frac{A^S(L)}{A^S(0)} \exp \left[ -\frac{\pi b^2}{2} (g^2 C) \rho L^2 f \left( \frac{L}{R_e^*} \right) \right], \quad (4.1)$$

where  $A^S(L)$  and  $A^S(0)$  are given by eqs. (2.36) and (2.37), respectively.

- (ii) **Multiple Whole Profile fitting of the intensity profiles.** In this procedure first the measured intensity profiles are normalized. Then all of them are fitted simultaneously by the normalized theoretical intensity function:

$$I(s) = \frac{F_c(s)}{F_c(0)}, \quad (4.2)$$

where  $F_c$  is the Cosine Fourier-transform of (5.9), which is equivalent to the inverse Fourier transform of  $A(L)$ , since  $A(L)$  is a real and even function:

$$F_c(s) = 2 \int_0^{\infty} A(L) \cos(2\pi Ls) dL. \quad (4.3)$$

In the MWP fitting procedure all profiles are fitted simultaneously using the nonlinear Marquardt-Levenberg least-squares algorithm, in which the Weighted Sum of Squared Residuals (WSSR) is minimised. In this procedure the profiles are weighted uniformly. Here it is noted that the profiles which correspond to the same  $g$  value but their  $hkl$  indices are not permutations of each other (e.g. the  $333$  and  $511$  reflections in the case of fcc cubic materials) should be omitted from the evaluation procedure, because their contrast factors are different and the theoretical Fourier-transform (2.59) corresponds to only one contrast factor. If the intensity ratio of these coincident reflections is known,

they can be included in the CMWP procedure, see Chapter 5 for more details. The theoretical functions depend on the  $hkl$  indices and on the microstructural parameters:  $m$  and  $\sigma$ , the parameters of the crystallite size distribution,  $\rho$ , the dislocation density,  $R_e^*$  the dislocation arrangement parameter and the strain anisotropy parameters  $q$  (or  $a_1, a_2$  for hexagonal crystals). These microstructural parameters are the common parameters which connect the different reflections during the simultaneous fitting. The difference between the theoretical profiles is in their  $hkl$  dependence which is scaled by  $g^2C$  depending on the  $q$  (or  $a_1, a_2$ ) anisotropy parameters. The values of the microstructural parameters are refined during the fitting procedure. If the ellipsoidal size function is used, the value of the ellipticity parameter,  $\varepsilon$  is refined too. The other parameters, the lattice constants,  $a$  (and  $c$  in the hexagonal case), the absolute value of the Burgers-vector ( $b$ ) and  $C_{h00}$  or  $C_{hk0}$  are input parameters of the fitting procedure. Since the strain Fourier–transform depends on the product  $b^2\rho C_{h00}$  (or  $b^2\rho C_{hk0}$  in the hexagonal case), the value of  $b$  and  $C_{h00}$  (or  $C_{hk0}$ ) should be known in order to determine the value of  $\rho$ . The value of  $C_{h00}$  (or  $C_{hk0}$ ) depend on the elastic constants of the materials and on the edge or screw character of the dislocations. However, in most cases the type of dislocations is only known after the fitting procedure, by analysing the contrast factor parameters ( $q$  or  $a_1, a_2$ ) which are the result of the fitting procedure. In this case an estimated value of  $C_{h00}$  (or  $C_{hk0}$ ) should be given during the fitting procedure, and the value of  $C_{h00}$  (or  $C_{hk0}$ ) should be determined according to the resulting  $q$  or  $a_1, a_2$  parameters. After this, the procedure should be repeated in order to get the correct value for  $\rho$ . For the method of determining the  $C_{h00}$  (or  $C_{hk0}$ ) constants, see Ungár et al. (1999). If the value of  $b$  or  $C_{h00}$  ( $C_{hk0}$ ) cannot be determined, the value of the microstructural parameter  $\rho$  becomes uncertain up to a scaling factor.

#### 4.1.5 The steps of the MWP evaluation procedure

The function of the program `evaluate` is to evaluate the previously prepared data for the microstructural parameters using the method of Multiple Whole Profile fitting. The steps of the evaluation procedure are:

1. *Selection of the crystal system.* The possible selections are: cubic or hexagonal. In the following the parentheses indicate the case of hexagonal system.
2. *Setting the value of the input parameters.* The program prompts for the value of the lattice constant(s), the absolute value of the Burgers-vector and  $C_{h00}$  (or  $C_{hk0}$ ).
3. *Selection of the size function.* The possible selections are: no size effect, spherical size function (default) or ellipsoidal size function.
4. *Specification of the sampling of the Fourier–transform of the measured data.* The number of samples (default: 256) and the upper limit of sampling (the default is: five times the maximal FWHM value of the Fourier profiles) may be specified.
5. *Computing the normalized Fourier–transform of the measured data.* This step is skipped if the Fourier–transforms are available from the instrumental correction (see the description of the

program MKDAT, sections 4.1.2 and 4.1.3) or from previous runs. The Fourier–transforms are saved after their computation.

6. *Specification of the initial values of the parameters and the limit of stopping.* The initial values of the fitting parameters are always saved for subsequent runs. The limit of stopping is the convergence criteria of the Marquardt-Levenberg algorithm: the fitting is stopped if the specified maximal number of iterations (default: 5000) is reached or if the relative change of the WSSR between two iteration steps is less than the specified limit (default:  $10^{-9}$ ).
7. *Selection of the method of fitting.* The procedure of Multiple Whole Profile fitting can be carried out by using the Fourier–transforms or the intensity profiles.
8. *Fitting.* In this step the values of the parameters are refined using the `gnuplot` program extensively modified for the MWP and CMWP procedures. The measured profiles and the fitted theoretical functions are plotted side by side in order of  $g$  and are replotted in each step of iteration, so one can trace continuously how the theoretical profiles approach the measured data. The figure is saved after the fit converges. A typical plot for fitting the Fourier–transforms is shown in Fig. 4.3.
9. *Printing of solutions.* In addition to the resulting parameters  $m$ ,  $\sigma$ ,  $\varepsilon$ ,  $\rho$ ,  $R_e^*$ ,  $q$  (or  $a_1$ ,  $a_2$ ) the dislocation arrangement parameter  $M^* = R_e^* \sqrt{\rho}$  (introduced by Wilkens) and the size parameters  $D$ ,  $d$  and  $L_0$  are printed too. These size parameters are defined by equations (2.12), (2.13) and (2.16), and they are calculated from the pure theoretical size profile using the fitted  $m$  and  $\sigma$  values.
10. *Preparation of figures.* If the Fourier–transforms were fitted, the program plots the intensity functions too. If the intensity functions were fitted, the program plots the Fourier–transforms too.
11. *Saving the results and removal of temporary files.*

It is noted that the actual fitting parameters used by the MWP and CMWP methods are denoted by  $a$ ,  $b$ ,  $c$ ,  $d$ ,  $e$  and these parameters are related to the microstructural parameters by the following equation:

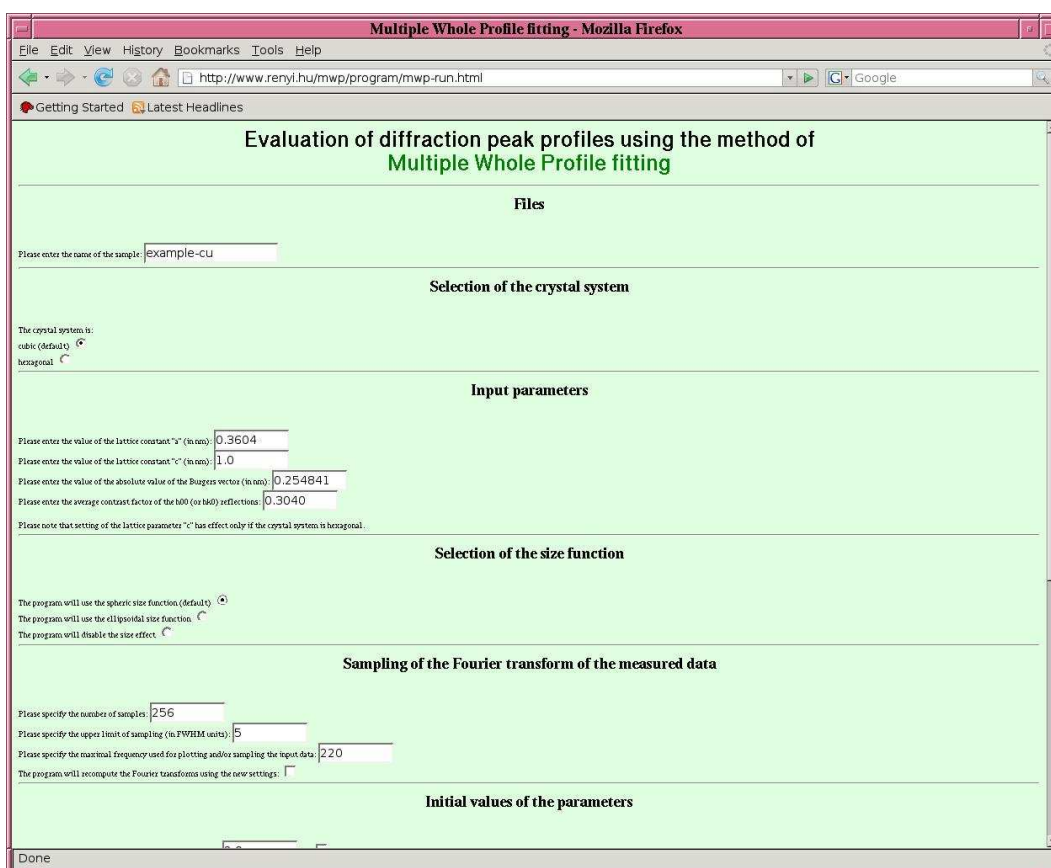
$$\begin{aligned}
 m &= \exp(b), \\
 \sigma &= \frac{c}{\sqrt{2}}, \\
 q &= a, \\
 \rho &= \frac{2}{\pi(b_{BURGERS}d)^2}, \\
 R_e^* &= \frac{\exp(-\frac{1}{4})}{2e},
 \end{aligned}
 \tag{4.4}$$

## 4.1.6 The MWP frontend

The program MKDAT and a WWW frontend for the evaluate program of the MWP procedure is available on the web: <http://www.renyi.hu/mwp>. The program MKDAT was developed for UNIX systems, and its goal is to prepare the measured data for the MWP evaluation procedure including the steps of peak separation and instrumental correction as described in sections 4.1.2 and 4.1.3. The MWP frontend provides a platform-independent interface of the procedure: after uploading the previously prepared data, the options of the fitting procedure can be selected (as described in section 4.1.5) and the evaluation procedure can be started.

Fig. 4.2 shows the control panel of the MWP frontend. A detailed description of the frontend can be found at the MWP documentation page:

<http://www.renyi.hu/mwp/doc>



The screenshot shows a web browser window titled "Multiple Whole Profile fitting - Mozilla Firefox". The address bar shows the URL <http://www.renyi.hu/mwp/program/mwp-run.html>. The page content is titled "Evaluation of diffraction peak profiles using the method of Multiple Whole Profile fitting". The interface is divided into several sections:

- Files**: A text input field for the sample name, containing "example-cu".
- Selection of the crystal system**: Radio buttons for "cubic (default)" (selected) and "hexagonal".
- Input parameters**: Four text input fields for lattice constants and contrast factors:
  - Lattice constant "a" (in nm): 0.3604
  - Lattice constant "c" (in nm): 1.0
  - Absolute value of the Burgers vector (in nm): 0.254841
  - Average contrast factor of the h00 (or h0l) reflections: 0.3040A note below states: "Please note that setting of the lattice parameter 'c' has effect only if the crystal system is hexagonal."
- Selection of the size function**: Radio buttons for "The program will use the spheric size function (default)" (selected), "The program will use the ellipsoidal size function.", and "The program will disable the size effect."
- Sampling of the Fourier transform of the measured data**: Three text input fields:
  - Number of samples: 256
  - Upper limit of sampling (in FWHM units): 5
  - Maximal frequency used for plotting and/or sampling the input data: 220A checkbox for "The program will recompute the Fourier transforms using the new settings:" is present and unchecked.
- Initial values of the parameters**: A section with a text input field and a checkbox, both partially visible.

Figure 4.2: The control panel of the MWP frontend: <http://www.renyi.hu/mwp>

## 4.2 MWP application to deformed Cu [S4, S6] and ball milled PbS [S9]

The MWP method was applied to polycrystalline copper samples of 99.98% purity deformed by ECA (Equal Channel Angular) pressing and by removing a surface layer of  $100\mu\text{m}$  with chemical etching [S4, S6]. The results of the MWP fit can be seen in Fig. 4.3. The procedure provided the following values for the microstructural parameters:  $m = 56\text{ nm}$ ,  $\sigma = 0.34$ ,  $q = 1.64$ ,  $\rho = 1.5 \cdot 10^{15} \frac{1}{\text{m}^2}$  and  $R_e = 5.1\text{ nm}$  [S4, S6].

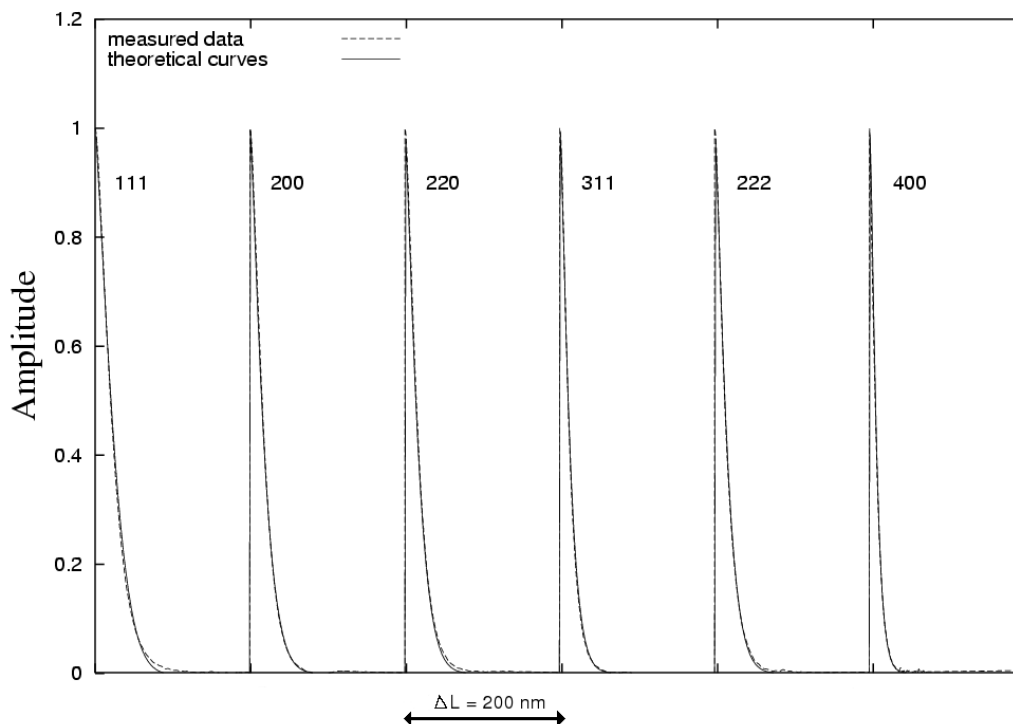


Figure 4.3: Example for the MWP fit (copper sample). In this figure the Fourier transforms of the measured and fitted profiles are plotted as a function of  $L$ . The peaks corresponding to the different  $hkl$  indices are plotted one after the other. The  $L$  ranges corresponding to the different peaks are independent, and extend from 0 to 200 nm for each peak.

The MWP procedure can be used to determine the microstructure of systematically prepared samples. Such an example is the fcc galena: a series of natural PbS (galena) samples were ball-milled and in some cases heat treated. These samples were studied by X-ray diffraction together with samples from ancient Egyptian make-ups fabricated from galena (Walter, 1999; Martinetto et al., 2000). The diffraction patterns were measured by the high resolution powder diffraction beam line, BM16 of ESRF in Grenoble, France (Martinetto et al., 2000). By evaluating the X-ray patterns of the archeological and systematically prepared samples a map of the microstructure was obtained. The microstructural parameters are considered as fingerprints of the state of the materials. By comparing the microstructural parameters of the archeological samples to that of the ball-milled and/or heat treated galena samples, the ancient manufacturing practices were traced back [S9]. It was found that the ancient specimens

have been gently crushed and no heat treatment was used or the heat treatment was carried out at temperatures not higher than about 300 °C.

Fig. 4.4 shows the MWP fit of the archeological sample E23105. In this case the procedure provided the following values for the microstructural parameters:  $m = 87$  nm,  $\sigma = 0.72$ ,  $q = -4.5$ ,  $\rho = 1.7 \cdot 10^{16} \frac{1}{m^2}$  and  $R_e = 10$  nm.

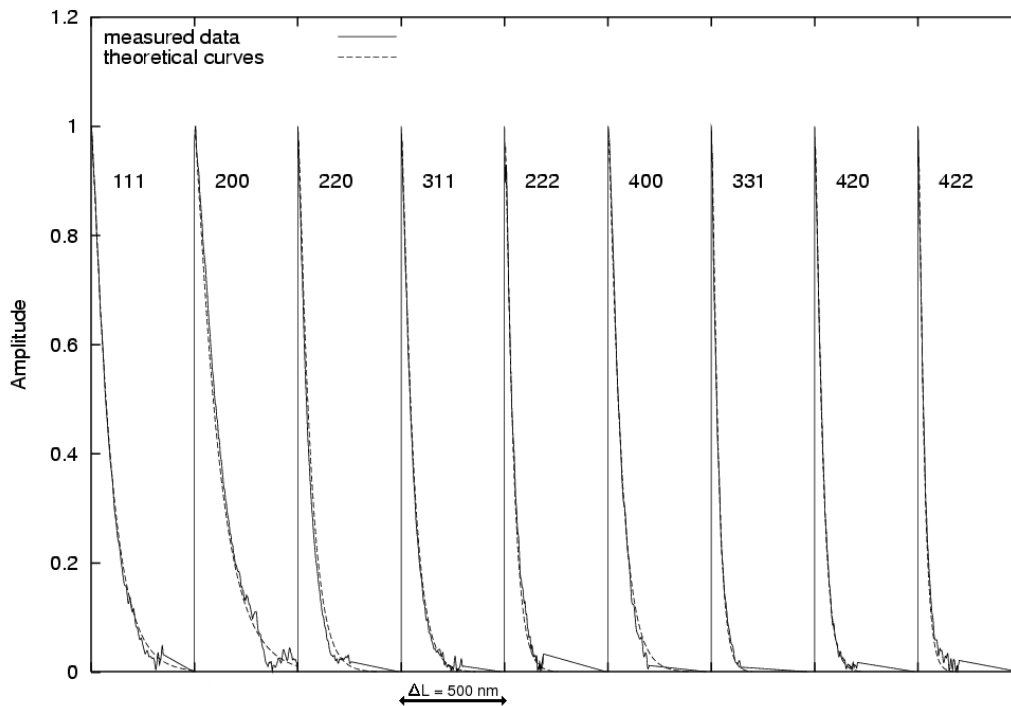


Figure 4.4: The MWP fit of the archeological galena sample E23105. The  $A(L)$  values of the measured and fitted profiles are plotted as a function of  $L$ .

PbS, galena is an ionic crystal, where it is not trivial if dislocations are created by plastic deformation (Sprackling et al., 1976). For this purpose, Martinetto and coworkers (2002) have carried out detailed transmission electron microscopy (TEM) on ball milled PbS crystals. A typical TEM micrograph in Fig. 4.5 shows the extended dislocation network in one of the deformed PbS specimens (Martinetto et al., 2002).

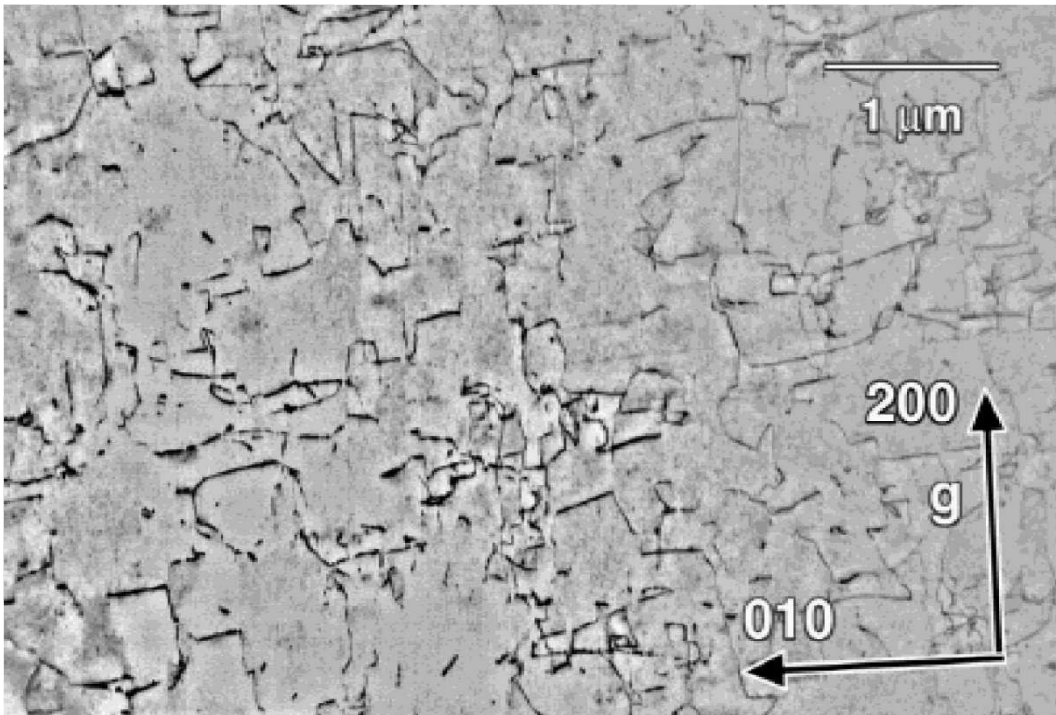


Figure 4.5: PbS coarse particle bright-field TEM micrograph of a dislocation network densely connected.

### 4.3 MWP application to Al-Mg alloys [S13, S14]

In [S13, S14] the effect of the nominal Mg content and the milling time on the microstructure and the hardness of mechanically alloyed Al-rich Al-Mg solid solutions were studied.

A series of Al-Mg samples were prepared from high purity aluminium (99.9%) powder and high purity magnesium chips (less than 2 mm thick and 5 mm long). The mechanical alloying was carried out using a Spex8000 shaker miller at room temperature.

Aluminium with 6 wt.% magnesium alloys were milled for periods of 0.5, 1, 3 and 6 h. Additionally, a series of Al - x wt.% Mg (x=0, 3, 6) were milled for 3 h at the same conditions to study the effect of the nominal Mg content. The milled powders were compacted at a pressure of 1 GPa in air at room temperature without any lubricant. The microstructure of both the ball-milled powders and the compacted specimens were studied by X-ray line profile analysis. The diffraction profiles were recorded by a Philips X'pert powder diffractometer using Cu anode and pyrolithic graphite secondary monochromator. Step size and step time were 0.030 and 22 s/step, respectively. The X-ray diffraction peak profiles were evaluated for the crystallite size distribution and the dislocation structure by the MWP fitting procedure. The measured and the fitted Fourier transforms are shown in Fig. 4.6 for the Al - 6 wt.% Mg specimen after ball milling for 0.5 h.

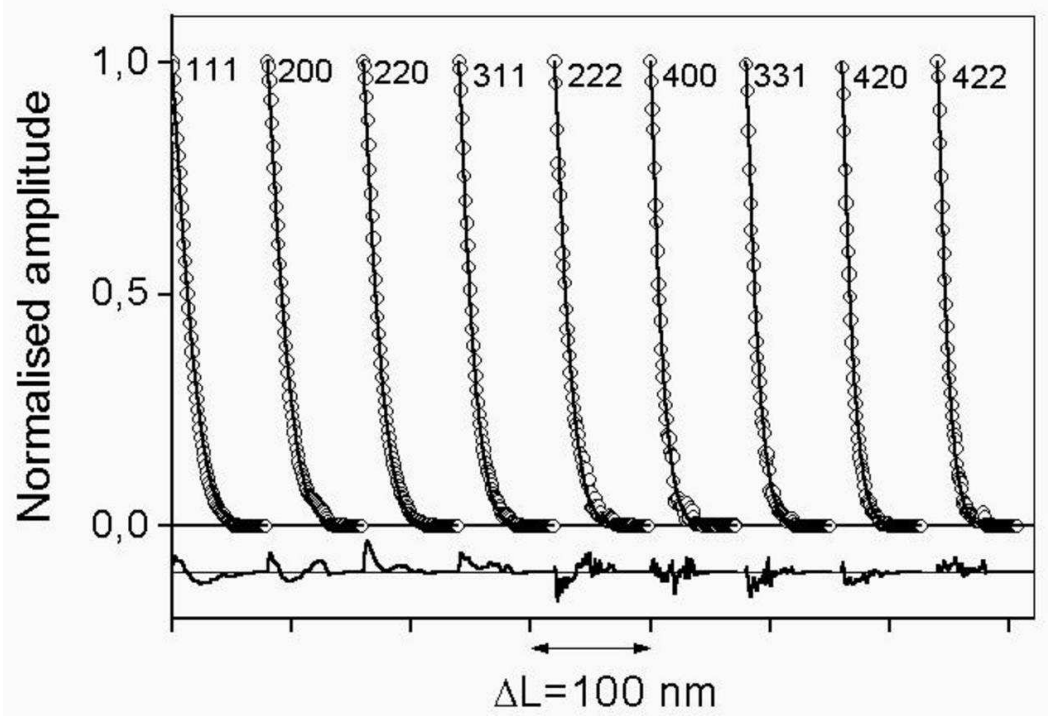


Figure 4.6: The MWP fit of the Al - 6 wt.% Mg specimen after ball milling for 0.5 h. The  $A(L)$  values of the measured and fitted profiles are plotted as a function of  $L$ . The difference plot is also given at the bottom of the figure.

The volume-weighted crystallite size, the dislocation density, the hardness and the Mg concentration as a function of the milling time and the nominal Mg content are plotted in Figs. 4.7 and 4.8, respectively. For the Al - 6 wt.% Mg samples the Mg concentration increases with milling time up to 3 h. After 3 h there is no change in the Mg concentration. The dislocation density increases while the crystallite size decreases rapidly with milling time up to 1 h. Between 1 and 6 h milling time the dislocation density and the crystallite size do not change significantly, as shown in Fig. 4.7. In the case where the nominal Mg content changes and the milling time period is fixed to 3 h, the Mg concentration in the solid solution and the dislocation density increase while the crystallite size decreases and the crystallite size distribution becomes wider with increasing nominal Mg content, as shown in Fig. 4.8.

The hardness of the compacted samples was also measured by depth-sensing Vickers indentation tests. For hardness measurements the ball milled powders were compacted. To check the effect of compaction on the microstructure, the parameters of the crystallite size distribution and the dislocation structure of the compacted specimens were determined by X-ray diffraction peak profile analysis. Comparing the microstructural parameters obtained before and after compaction it is concluded that this procedure has only slight effects on the microstructure of the ball milled specimens. This means that the hardness measured on the compacted samples characterizes also the mechanical properties of the milled Al-Mg alloys.

By analysing the hardness values for the compacted specimens it was found that with increasing milling time, the hardness increases up to 3 h due to the increasing Mg concentration, the increase of the dislocation density and the decrease of crystallite size. Upon increasing milling time from 3 to 6 h the hardness does not change significantly since neither the Mg concentration nor the microstructure changes. It is found that the Mg concentration in Al-Mg alloys has a considerable effect on the defect structure. With increasing nominal Mg content of the powder or increasing milling time, the dislocation density increases and the character of dislocations is shifted toward edge type. These changes can be attributed to the increase of the solute Mg concentration which increases the pinning effect of Mg atoms on edge dislocations thus hindering their annihilation. After 3 h milling the Mg concentration in solid solution is much higher than the equilibrium solubility limit. The hardness obtained for the mechanically alloyed Al 3 wt.% Mg specimen is in good correlation with those predicted from the Hall-Petch relationship (Hall, 1951; Petch, 1953) determined for bulk samples in other papers.

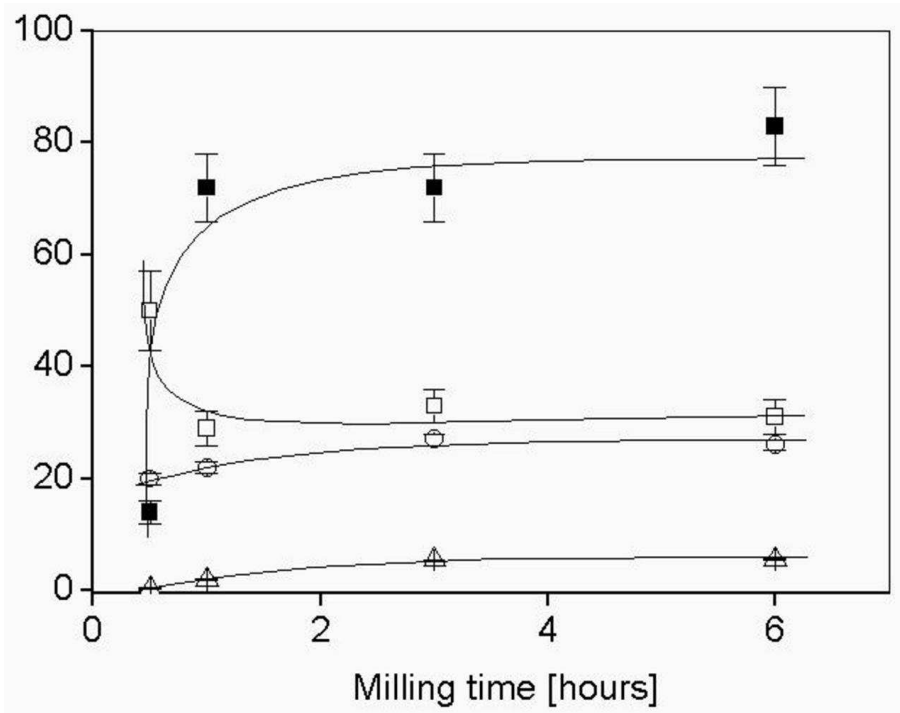


Figure 4.7: The volume-weighted mean crystallite size in nanometers (open squares), the dislocation density in  $10^{14}m^{-2}$  (solid squares), the Mg concentration in wt.% (open triangles) and the hardness in  $10^8 Pa$  (open circles) as a function of the milling period for the specimen of Al-6wt.% Mg nominal composition.

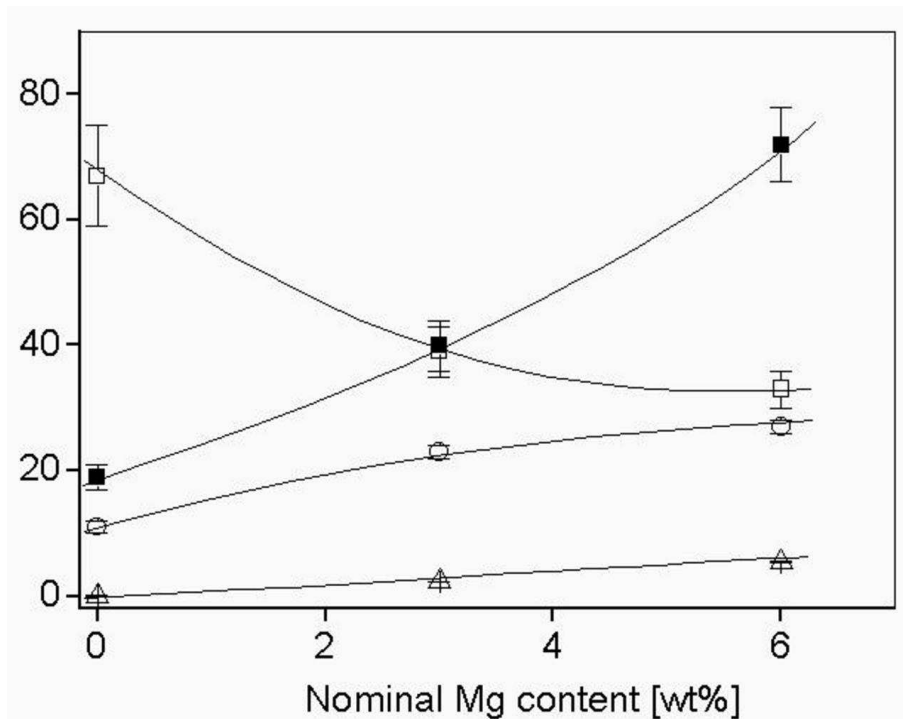


Figure 4.8: The volume-weighted mean crystallite size in nanometers (open squares), the dislocation density in  $10^{14}m^{-2}$  (solid squares), the Mg concentration in wt.% (open triangles) and the hardness in  $10^8 Pa$  (open circles) as a function of the nominal Mg content for the specimens ball milled for 3h.

## 4.4 MWP application to Ti [S12, S21] and Si<sub>3</sub>N<sub>4</sub> [S1, S6]

Hexagonal Ti samples were investigated in [S12]. Nanocrystalline titanium specimens were produced by severe plastic deformation (ECA pressing) and X-ray diffractograms were measured by a Philips X'pert diffractometer. The profiles were evaluated using the MWP method and the procedure provided the following values for the microstructural parameters:  $m = 38 \text{ nm}$ ,  $\sigma = 0.49$ ,  $q_1 = -0.05$ ,  $q_2 = 0.18$ ,  $\rho = 8.6 \cdot 10^{14} \frac{1}{\text{m}^2}$  and  $M = 6.5$ . The results of the MWP fit can be seen in Fig. 4.10. The large dislocation density of  $\rho \simeq 9 \times 10^{14} \text{ m}^{-2}$  is confirmed by detailed high resolution TEM as shown in the micrograph in Fig. 4.9 (Zhu et al., 2003).

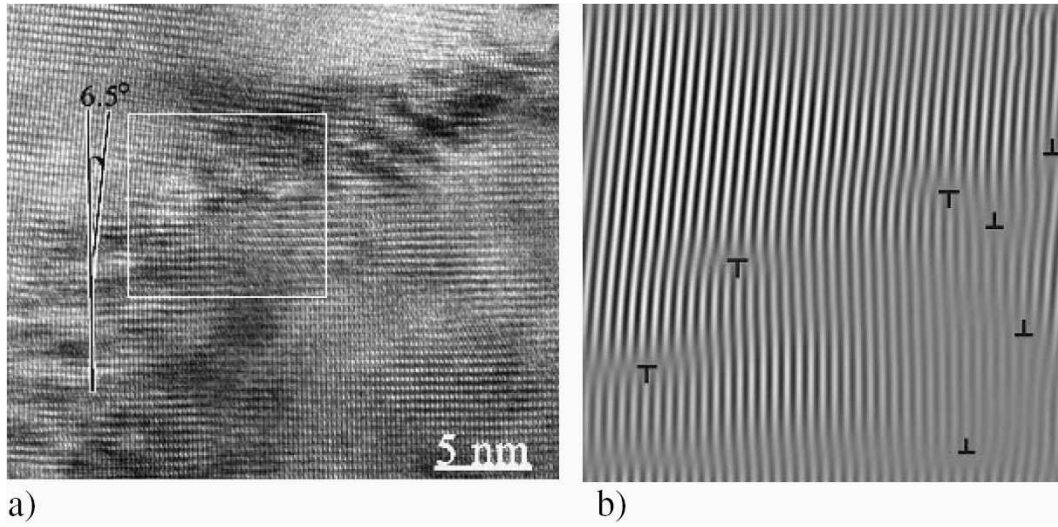


Figure 4.9: (a) High resolution TEM image of a low-angle grain boundary with a misorientation of 6.5°, (b) Fourier-filtered image from the white frame in (a), showing the dislocation arrangement in the grain boundary.

From the analysis of the measured  $q$  parameter values,  $q_1^{(m)}$  and  $q_2^{(m)}$ , which are easily derived from the  $a_1$  and  $a_2$  fitting parameters according to equations  $q_1^{(m)} = a_1$  and  $q_2^{(m)} = -\frac{a_1}{\frac{2}{3} \left(\frac{c}{a}\right)^2} + a_2$  (Dragomir & Ungár, 2002), the active slip system types can be concluded [S21]. In the ECAP deformed Ti specimen it was found that the dominant active slip system types are  $\langle a \rangle$  and  $\langle c + a \rangle$  [S11, S22], in good correlation with TEM observations (Paton et al., 1970).

Another hexagonal samples were investigated in [S1, S6]. Commercial Si<sub>3</sub>N<sub>4</sub> samples (powder LC12 from Starck Ltd, Germany) were investigated by X-ray diffractometry. The results of the MWP fit can be seen in Fig. 4.12.

Fig. 4.11 shows the TEM micrograph of the Si<sub>3</sub>N<sub>4</sub> particles and the particle size distributions measured either by TEM or X-ray line profile analysis. A good correlation between the two size distributions determined by two completely different methods can be seen.

The microstructural parameter values determined by X-ray line profile analysis are listed in Table 4.1.

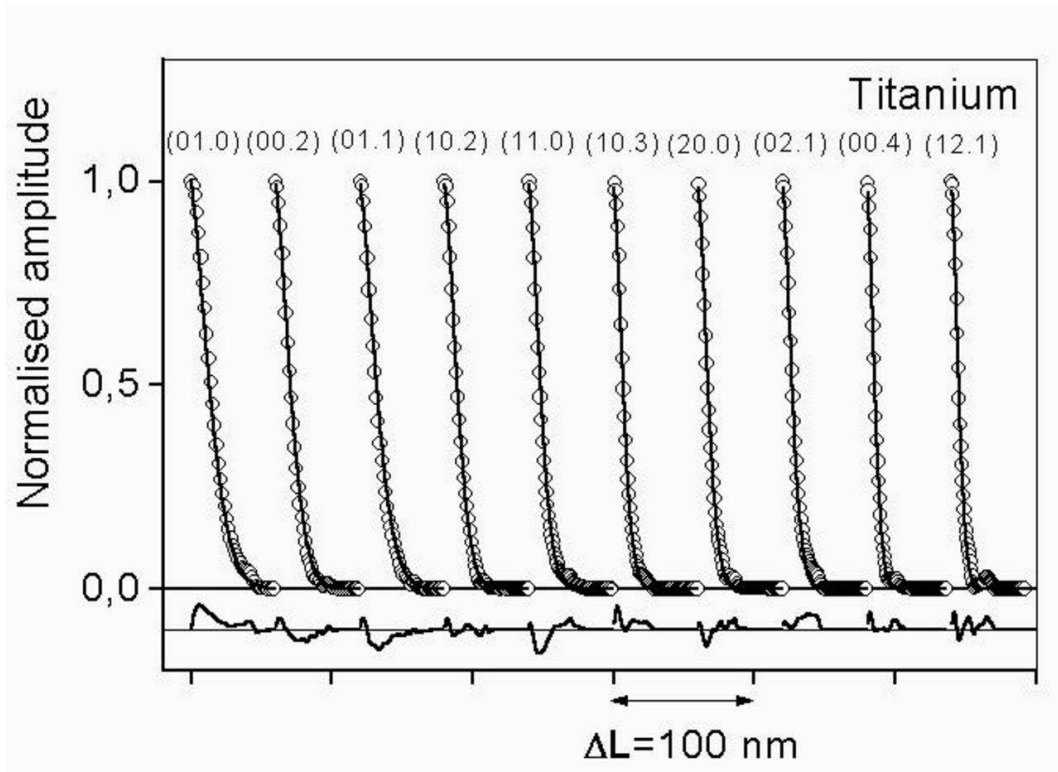


Figure 4.10: The MWP fit of the hexagonal Ti sample. The  $A(L)$  values of the measured and fitted profiles are plotted as a function of  $L$ .

Table 4.1: Microstructural parameters obtained for nanocrystalline  $\text{Si}_3\text{N}_4$  determined by the MWP method

$m$ [nm]	$\sigma$	$\rho$ [ $10^{14} \text{ m}^{-2}$ ]	$M$	$a_1$	$a_2$
20 (3)	0.65 (5)	7.5 (8)	2.1	3.54	-1.93

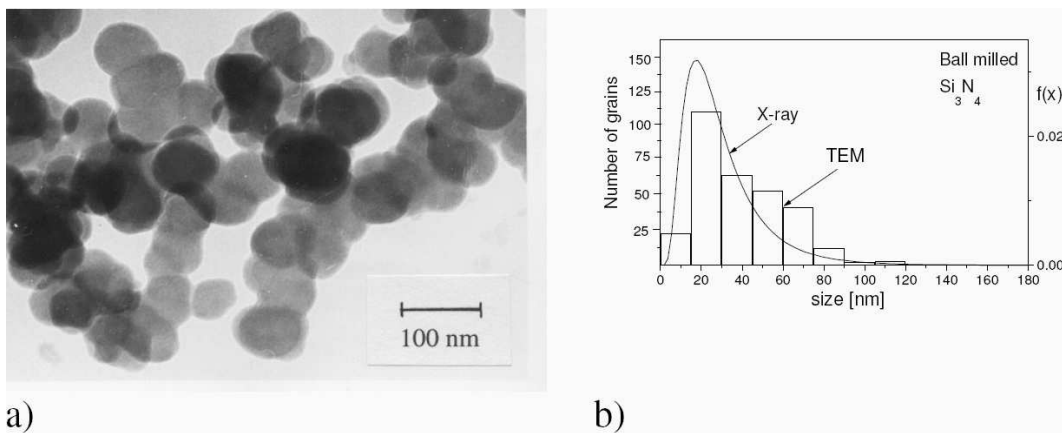


Figure 4.11: (a) TEM micrograph of the  $\text{Si}_3\text{N}_4$  particles, (b) particle size distributions measured by TEM and X-ray line profile analysis.

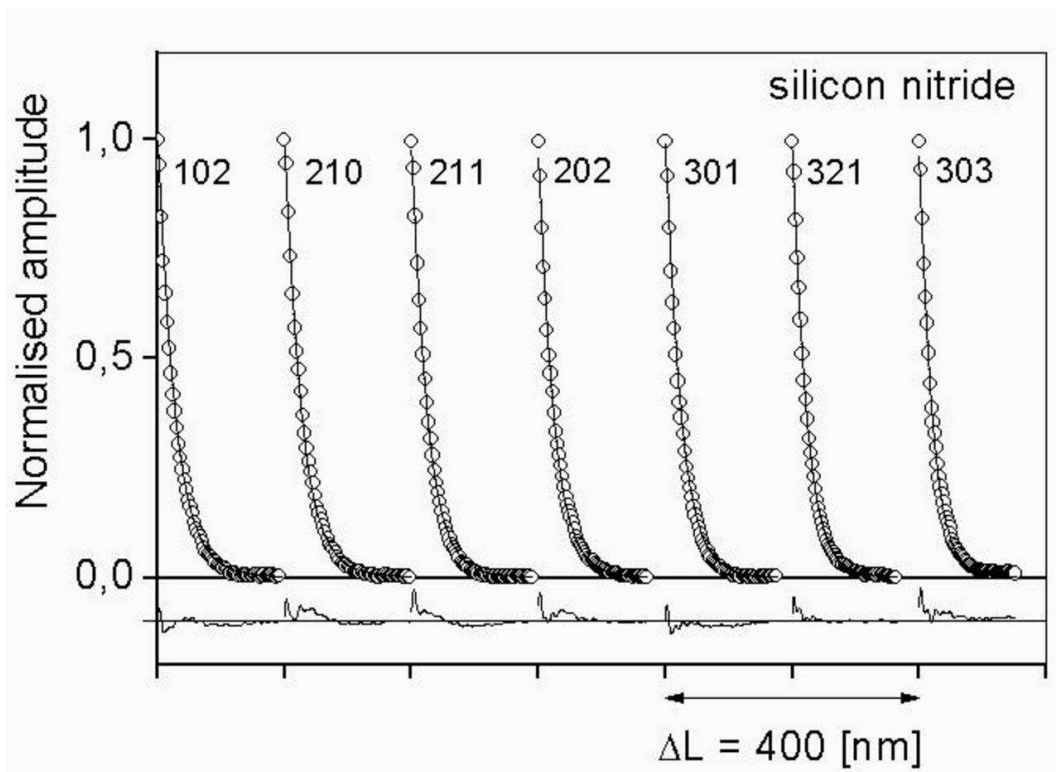


Figure 4.12: The MWP fit of the hexagonal  $\text{Si}_3\text{N}_4$  sample. The  $A(L)$  values of the measured and fitted profiles are plotted as a function of  $L$ . The difference plot is also given at the bottom of the figure.

## 4.5 MWP evaluation of carbon black samples by assuming ellipsoidal crystallite shape [S4, S5, S6, S8]

The microstructure of hexagonal carbon blacks were investigated in [S5, S8]. Carbon black has the turbostratic layer structure, therefore the evaluation could only be carried out by assuming that the coherently scattering domains are of ellipsoidal shape flat crystallites (Warren, 1965). The measured X-ray profiles were evaluated using the MWP procedure with the additional assumption that the crystallites are rotational ellipsoids (see section 2.2.4 for more details about the ellipsoidal size function). Untreated, heat treated and compressed at 2.5 GPa carbon black specimens were investigated. The measured X-ray profiles were evaluated using the MWP procedure and assuming ellipsoidal crystallite shape. The value of  $\epsilon$ , the ellipticity parameter is found between 0.5 and 1.2.

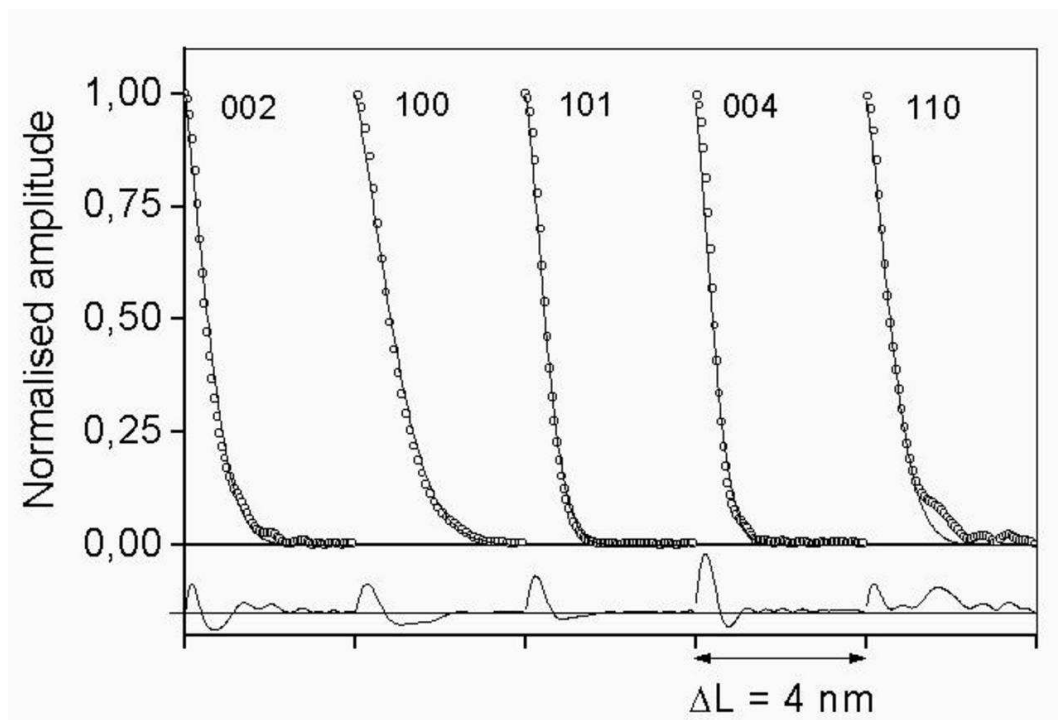


Figure 4.13: The MWP fit of carbon black sample. The  $A(L)$  values of the measured and fitted profiles are plotted as a function of  $L$ . The difference plot is also given at the bottom of the figure.

## Chapter 5

# Determining microstructure by the Convolutional Multiple Whole Profile fitting method

The CMWP procedure and a couple of problems solved by this method are described and discussed in detail. It is shown that the CMWP method enables to evaluate X-ray diffraction patterns in terms of crystallite size and size distribution, dislocation densities and dislocation character, without the necessity to separate overlapping diffraction peaks or to deconvolute instrumental effects. It is shown that the CMWP method makes it also possible to obtain the density and character of stacking faults or twin boundaries. A special application of the CMWP procedure to solve the problem of unusual narrowing of the first few diffraction peaks in ball milled fluorides is also presented.

### 5.1 The CMWP method [S14]

The Convolutional Multiple Whole Profile (CMWP) fitting procedure works as a computer program developed for the determination of microstructural parameters from diffraction profiles of materials with cubic, hexagonal or orthorhombic crystal lattices [S14], but works in principle, for all crystal systems. Unlike the MWP method, which uses the Fourier transform of the separated profiles, the CMWP method works directly on the measured intensity pattern and the separation of the profiles is not needed. Another difference is, that there is no need to correct the measured data for the instrumental effect. The instrumental effect is added to the theoretical (physical) pattern by convolution, thus avoiding numerical division of small numbers.

#### 5.1.1 The principles of the method

The whole measured powder diffraction pattern is fitted directly by the sum of a background function and profile functions obtained as the convolution of ab-initio theoretical functions for size, strain and planar faults and the measured instrumental profiles [S14]:

$$I_{theoretical} = BG(2\theta) + \sum_{hkl} I_{MAX}^{hkl} I^{hkl}(2\theta - 2\theta_0^{hkl}), \quad (5.1)$$

where  $BG(2\theta)$  represents the background,  $I_{MAX}^{hkl}$  is the peak intensity,  $2\theta_0^{hkl}$  is the  $2\theta$  value at the peak center and  $I^{hkl}$  is the theoretical profile for the  $hkl$  reflection, which can be expressed as the convolution of  $I_{instr.}^{hkl}$ , the *measured* instrumental profile and ab-initio profile functions:  $I_{size}^{hkl}$ , the theoretical size profile,  $I_{disl.}^{hkl}$ , the theoretical strain profile for dislocations and  $I_{pl.faults}^{hkl}$ , the theoretical profile function for planar faults:

$$I^{hkl} = I_{instr.}^{hkl} * I_{size}^{hkl} * I_{disl.}^{hkl} * I_{pl.faults}^{hkl} \quad (5.2)$$

This convolutional equation is based on equation (2.50) given by Warren & Averbach (1952). The equation can be easily extended to include other physical effects as further sources of broadening. In order to get realistic results, not all the effects should be included without consideration in the evaluation procedure, it is better to have some initial knowledge about the nature of the effects causing the broadening and only the physically relevant effects should be included in the evaluation. There are several possibilities to obtain this preliminary knowledge about the nature of the microstructural effects. For example TEM observations can be used or the qualitative information provided by the Williamson-Hall plot or the momentum method on one of the reflections can be used. In the calculation of the theoretical functions it is assumed that the crystallites have spherical or ellipsoidal shape with lognormal size distribution and strain is caused by dislocations. Strain and size anisotropy are taken into account by the dislocation contrast factors and the ellipticity of crystallites, respectively. The mathematical formulae together with the dependence on the microstructural parameters of these theoretical functions are given in Chapter 2. Note that in most cases the Fourier transform of the profiles is expressed in an analytical form, which is favourable, since in the CMWP method, the convolution is carried out in the Fourier-space and the  $I^{hkl}$  profiles are obtained by inverse Fourier-transforming the product of the theoretical Fourier transforms and the (complex) Fourier transform of the corresponding measured instrumental profiles. Another possibility would be the usage of the definition of the convolution:

$$(f * g)(x) = \int_{-\infty}^{\infty} f(t) g(x-t) dt, \quad (5.3)$$

however, it is simpler and considerably faster for obtaining the theoretical intensity profile to directly use the Fourier transforms provided by theory and performing an inverse Fourier transformation once after the multiplication of the Fourier transforms, than inverse Fourier transforming all the theoretical Fourier transforms and using the convolutional equation (5.3). Depending on the effects included, the fitting procedure can provide the following microstructural parameters: median and the variance of the size distribution, the ellipticity of the crystallites, the density and arrangement of dislocations, the strain anisotropy parameters and the probability of planar faults. Since it is a microstructural

method, the  $I_{MAX}^{hkl}$  and  $2\theta_0^{hkl}$  values are not modeled on the basis of the crystal structure, they are treated simply as free fitting parameters. The fit should be carried out in two steps: in (i) the  $I_{MAX}^{hkl}$  and  $2\theta_0^{hkl}$  parameters are fitted together with the microstructural parameters (a few steps of iteration is usually enough to determine the  $I_{MAX}^{hkl}$  and  $2\theta_0^{hkl}$  parameters which is the goal of this step; in this step the values of the physical parameters are not interpreted) and in (ii) the previously fitted  $I_{MAX}^{hkl}$  and  $2\theta_0^{hkl}$  parameters are fixed and only the physical parameters are refined.

The CMWP procedure treats the reflections which correspond to the same  $g$  value but their  $hkl$  indices are not permutations of each other (e.g. the  $333$  and  $511$  reflections in the case of fcc cubic materials). In this case both profiles are added to the model based, generated pattern and an intensity ratio is introduced for this purpose (the total intensity at maximum is equal to  $I_{MAX}^{hkl}$  in this case too). By avoiding the need for the profile separation and instrumental correction the CMWP method is free from the uncertainties due to these steps and it is much more adequate and superior in a sense than the MWP method for evaluating full powder patterns with overlapping peaks. However, if the overlapping of the profiles is weak and they are measured separately on an instrument with negligible instrumental effect, like a Nonius FR 591 special double crystal high resolution diffractometer (see e.g. Ungár et al., 1998), it is more convenient to apply the MWP method. In the case of separately measured profiles, before applying the CMWP method the profiles should be linked into a pattern, the empty  $2\theta$  regions between the peaks should be filled with artificial data and in this case the background of the generated pattern usually has larger steps because of the different level of background of the different peaks. This causes uncertainties when determining the background which is not present when using the MWP procedure in these cases. The situation is the same for the evaluation of the measured profiles of single crystals, where obviously no powder pattern can be measured. Another case when the MWP method is more suitable than the CMWP when only the Fourier transforms of the profiles are available. In the CMWP procedure the measured and model-generated pattern given by eq. (5.1) are compared using the Marquardt-Levenberg nonlinear least squares algorithm (Levenberg, 1944 and Marquardt, 1963) and the fitting procedure provides the parameters of the ab-initio theoretical functions as well as the refined theoretical powder pattern. Figs. 5.1 and 5.2 demonstrate the results of the CMWP fitting procedure for Al-6Mg sample ball milled for 6 hours, the measured and the fitted pattern are shown in both linear and logarithmic scale and their difference is shown in linear scale. The results for the microstructural parameters are also indicated.

### 5.1.2 The JAVA frontend of CMWP

There are two main options to use the CMWP method: the first is to run directly the program evaluate (which is part of the CMWP package) and the second is to use it via its WWW frontend. Latter will be described in the next subsection. The evaluate program is a frontend written in the

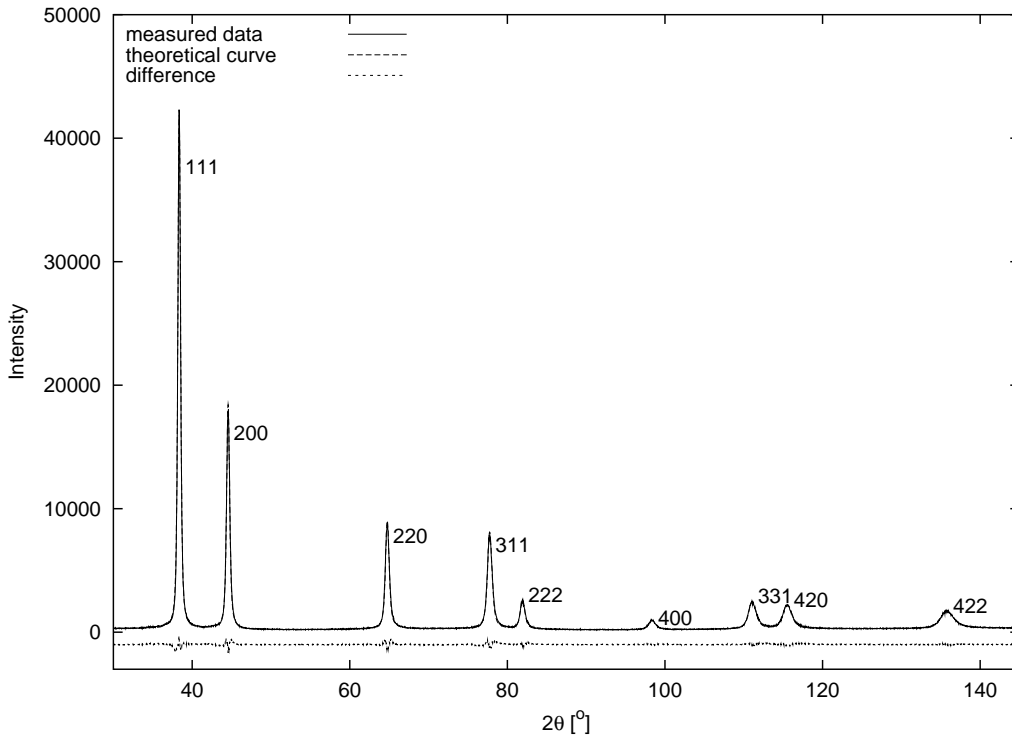
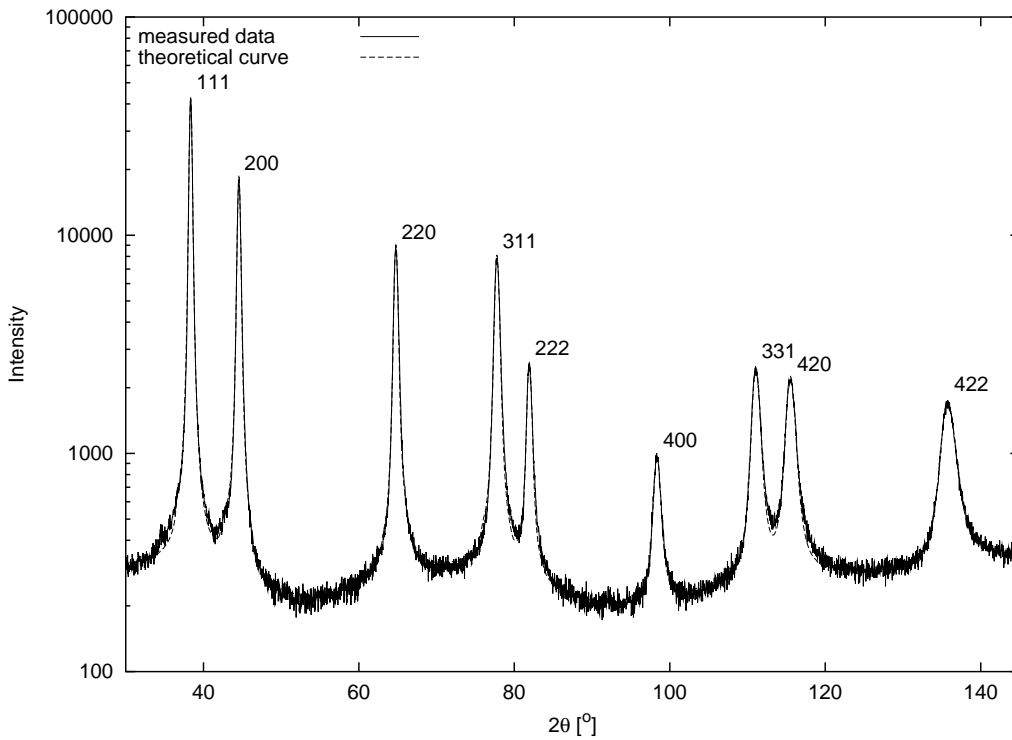


Figure 5.1: The measured (solid lines) and theoretical fitted (dashed lines) intensity patterns for Al-6Mg sample ball milled for 6 hours as a function of  $2\theta$ . The difference plot is also given at the bottom of the figure.



Results of the  
CMWP fit:  
 $m = 21\text{nm}$   
 $\sigma = 0.36$   
 $\rho = 10^{16}\text{m}^{-2}$   
 $M = R_e\sqrt{\rho} = 1.3$   
 $q = 1.3$

Figure 5.2: The measured (solid lines) and theoretical fitted (dashed lines) intensity patterns for Al-6Mg sample ball milled for 6 hours as a function of  $2\theta$  (plotted with logarithmic intensity scale). The results for the microstructural parameters are also indicated.

shell script language zsh and it is enhanced with graphical functions written in the JAVA programming language. Fig. 5.3 shows the JAVA panel of the evaluate frontend. All the parameters can be adjusted in this panel and all the functions of the fitting can be reached by pressing the appropriate buttons. Another JAVA tool, the mkspline program can be used for the interactive determination of the base points of the background spline. See Fig. 5.4 for an example of the background spline determined by mkspline.

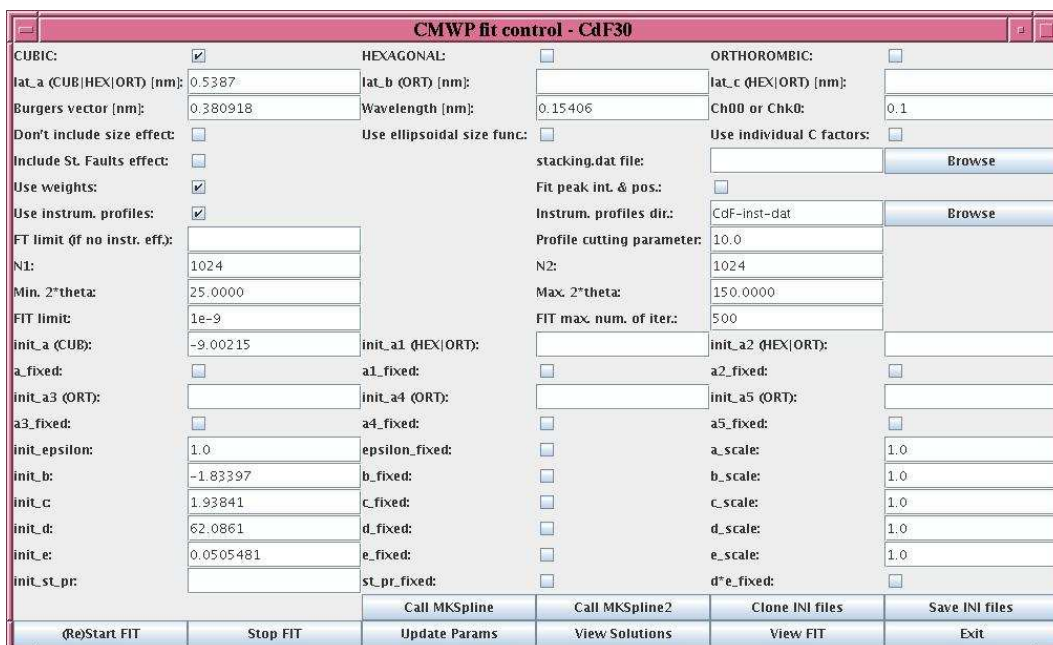


Figure 5.3: The JAVA panel of the CMWP frontend

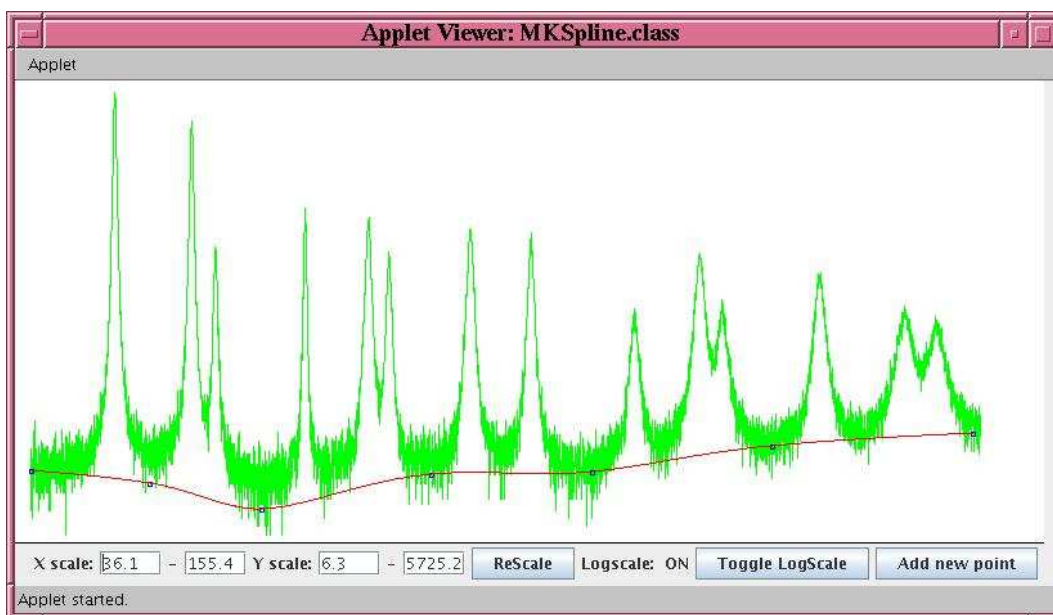


Figure 5.4: The mkspline program of the CMWP package

### 5.1.3 The WEB frontend of CMWP

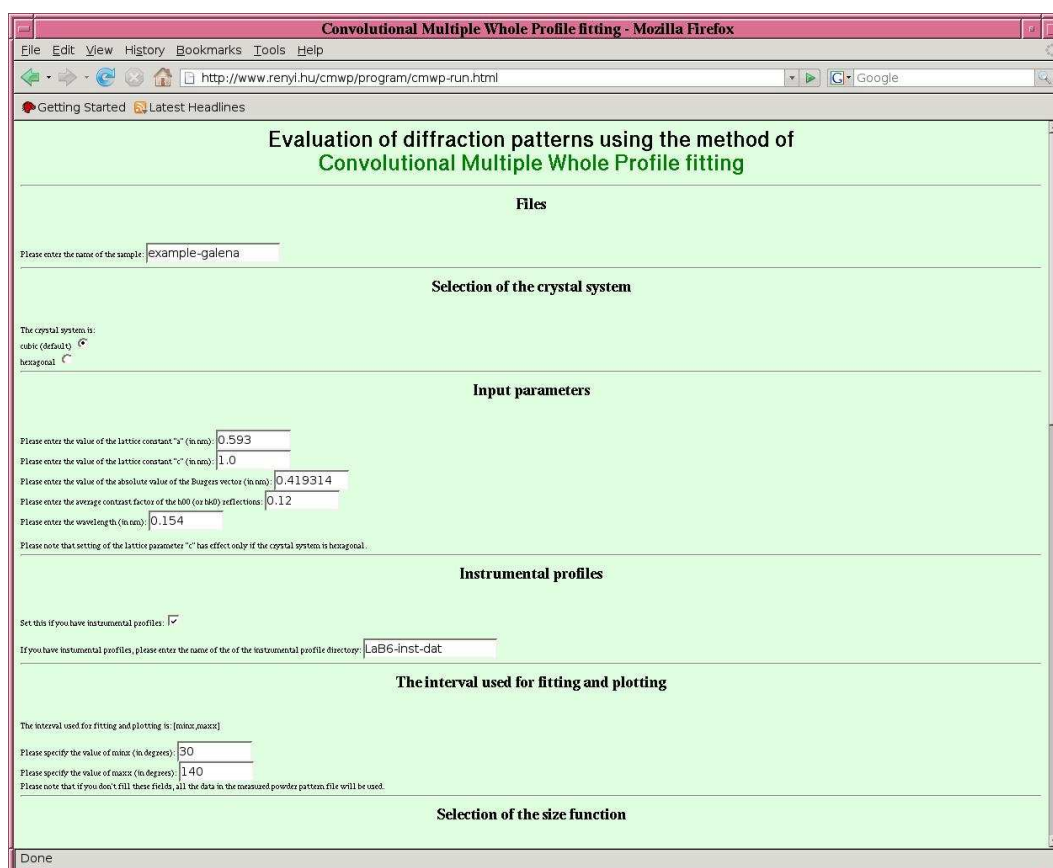
The CMWP procedure can also be used via its WWW frontend:

<http://www.renyi.hu/cmwp>

This latter option has many advantages compared to the previous one:

1. it is platform-independent, only an internet connection and a machine with a working web browser is needed,
2. there is no need for installation,
3. the frontend is served by well configured and relatively fast machines,
4. the program and the code behind the frontend is continuously maintained.

Fig. 5.5 shows the control panel of the CMWP frontend, a more detailed description of the frontend can be found at the CMWP documentation page: <http://www.renyi.hu/cmwp/doc>



The screenshot shows a web browser window titled "Convolutional Multiple Whole Profile fitting - Mozilla Firefox". The address bar shows the URL <http://www.renyi.hu/cmwp/program/cmwp-run.html>. The page content is titled "Evaluation of diffraction patterns using the method of Convolutional Multiple Whole Profile fitting".

The form is divided into several sections:

- Files**: A text input field for "Please enter the name of the sample:" with the value "example-galena".
- Selection of the crystal system**: A dropdown menu showing "cubic (default)" and "hexagonal".
- Input parameters**: Several input fields with labels and values:
  - "Please enter the value of the lattice constant 'a' (in nm):" with value "0.593".
  - "Please enter the value of the lattice constant 'c' (in nm):" with value "1.0".
  - "Please enter the value of the absolute value of the Burgers vector (in nm):" with value "0.419314".
  - "Please enter the average contrast factor of the h00 (or h0l) reflections:" with value "0.12".
  - "Please enter the wavelength (in nm):" with value "0.154".
- Instrumental profiles**: A checkbox "Set this if you have instrumental profiles:" which is checked. Below it, a text input field for "If you have instrumental profiles, please enter the name of the of the instrumental profile directory:" with the value "\_lab6-inst-dat".
- The interval used for fitting and plotting**: A label "The interval used for fitting and plotting is: [minix,maxix]". Below it, two input fields:
  - "Please specify the value of minix (in degrees):" with value "50".
  - "Please specify the value of maxix (in degrees):" with value "140".
- Selection of the size function**: A section header at the bottom of the form.

The browser's status bar at the bottom shows "Done".

Figure 5.5: The control panel of the CMWP frontend

### 5.1.4 The CMWP evaluation procedure

Using the evaluation program (by running `evaluate` or by using the WWW frontend) one can evaluate the previously prepared and uploaded data for the microstructural parameters using the CMWP method. The steps of the evaluation are the following:

1. *Specification of the sample name.*
2. *Selection of the crystal system.* The possible selections are: cubic (default), hexagonal or orthorhombic.
3. *Setting the values of the input parameters.* The value of the lattice constants, the absolute value of the Burgers-vector,  $C_{h00}$  (or  $C_{hk0}$  in the case of hexagonal crystal system) and the wavelength of the measuring instrument have to be specified.
4. *Specification of the instrumental profiles.* If instrumental profiles are available, the inclusion of the instrumental effect can be selected and the name of the instrumental profiles directory can be specified.
5. *Determining the background.* The base points of the background spline should be given interactively by using the `mk spline` program.
6. *Peak searching.* In this step the indices, the centers and the maximal intensities of all peaks should be determined.
7. *Specification of the interval used for fitting and plotting.* Here can be specified the lower and upper limit of the interval used for fitting and plotting (in  $2\theta$  degrees).
8. *Selection of the size function.* The possible selections are: no size effect, spherical size function (default) or ellipsoidal size function.
9. *Specification of the sampling of the theoretical Fourier transforms.* The  $A_{lim}$  amplitude ratio limit of the normalized theoretical Fourier transforms can be specified, see section 5.1.6 for more details. It is noted here that this limit should be specified only in case if no instrumental profiles are available.
10. *Specification of the sampling of the simulated powder pattern data.* The value of  $N1$ ,  $N2$  and the profile cutting parameter should be specified here. For the details of the meaning of these parameters see sections 5.1.7 and 5.1.8.
11. *Specification of the initial values of the parameters.* The initial values of the fitting parameters have to be specified. They are always saved for subsequent runs. There is an option for fixing the value of any parameter, which means that the value of that parameter will not be refined during the fitting procedure. Fixing the value of  $d \cdot e$  means that the value of the parameter  $M^*$  is fixed. This option can be used if the program enters into an asymptotic minimum (the

values of  $\rho$  and  $R_e^*$  tend to infinity and zero, respectively, and the asymptotic standard errors of the parameters  $d$  and  $e$  become extremely large, larger than 100%). The scales of the fitting parameters can also be specified here.

12. *Peak parameter refinement and weighting.* Here the refinement of the peak positions and peak intensities can be chosen. If the peaks have very different intensities, you can choose here to use weights in the fitting algorithm (see section 5.1.10 for more details about the weighting algorithm).
13. *Fit control.* The limit of stopping is the convergence criterium of the Marquardt-Levenberg algorithm: the fitting is stopped if the specified maximum number of iterations (default: 200) is reached or if the relative change of the WSSR between two iteration steps is less than the specified limit (default:  $10^{-9}$ ).
14. *Fitting.* In this step the values of the parameters are refined using the `gnuplot` program extensively modified for the MWP and CMWP procedures. The measured and the fitted theoretical pattern are plotted and are replotted in each step of iteration, so one can trace continuously how the theoretical pattern approaches the measured data. The figure is saved after the fit converges. A typical plot for fitting is shown in Fig. 5.2.
15. *Printing of solutions.* The resulting physical parameters  $m$ ,  $\sigma$ ,  $\varepsilon$ ,  $\rho$ ,  $R_e^*$ ,  $q$  (or  $a_1$ ,  $a_2$ ),  $\alpha$  together with the dislocation arrangement parameter  $M^* = R_e^* \sqrt{\rho}$  and the size parameters  $d$  and  $L_0$  are printed.
16. *Preparation of figures.* The program plots the measured and theoretical fitted patterns together with their differences in linear scale and the data is saved in a file containing 4 columns:  $2\theta$ , the measured intensities, the fitted intensities and their difference. A plot with logarithmic scale is also created.
17. *Saving the results and removal of temporary files.*

### 5.1.5 Determining the background

The background function  $BG(2\theta)$  is given by an analytical function.

By giving the list of the relevant base points of the physical background, the background function is determined as the interpolated *cubic spline* corresponding to the specified base points. Fig. 5.6 shows an example for the spline background. The base points are indicated in Table 5.1. Fig. 5.4 shows the spline background of a real sample.

Another possibility is to use a sum of *Legendre polynomials* as the background. In this case, the coefficients must be specified. The Legendre polynomials are orthogonal functions, so there is no dependence between the coefficients.

x	y
30	120
40	420
60	320
65	520
70	580
93	670

Table 5.1: The base points for the example spline background.

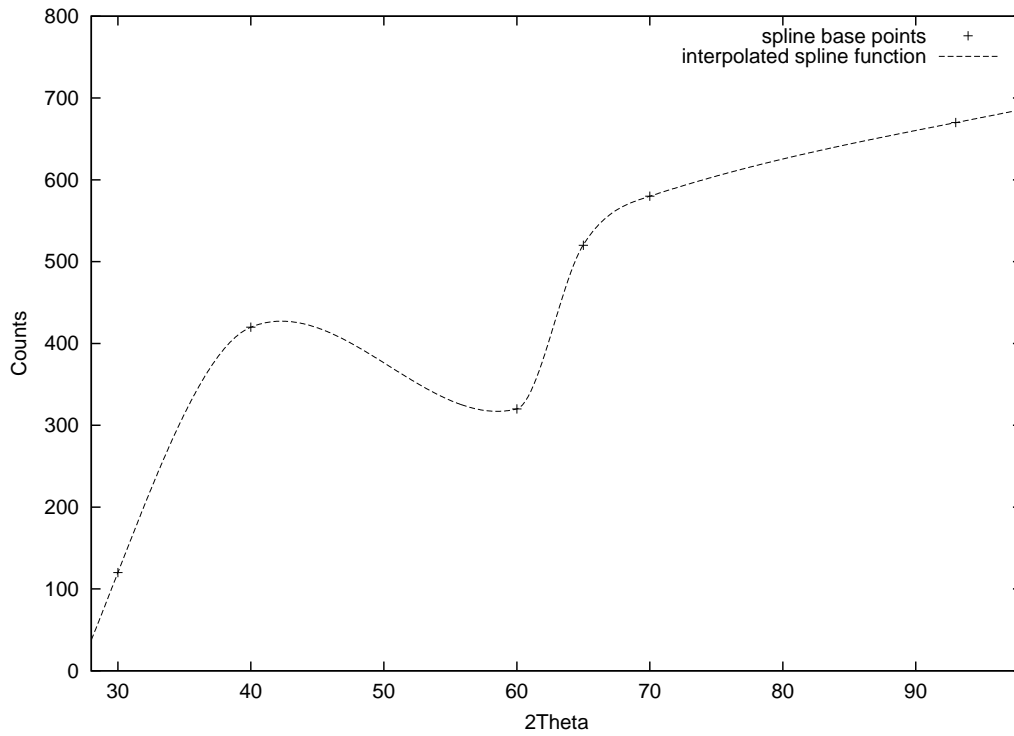


Figure 5.6: Example for a cubic spline, which can be used as background. As it can be seen, the spline goes through the points very smoothly.

### 5.1.6 Sampling of the Fourier transforms

In the CMWP procedure the sampling of the Fourier transforms depends on whether instrumental broadening is present or not.

- If there is no instrumental effect, the Fourier transforms are evaluated with an arbitrary precision specified by the user of the program. The sampling of the theoretical Fourier transform is determined by  $A_{lim}$ , an amplitude ratio limit: for each reflection, the normalized theoretical Fourier transform is calculated with equidistant sampling from  $L = 0$  to  $L_{max}^{hkl}$ , where  $L_{max}^{hkl}$  is defined by the following equation:  $\frac{A(L_{max}^{hkl})}{A(0)} = A_{lim}$ .
- If instrumental profiles are available, the sampling of the theoretical Fourier transforms depends on the Fourier transform of the measured instrumental profiles. Since the measured instrumental profile is represented by a set of numerical data which terminates at a finite  $2\theta$  value, its Fourier transform is periodic. If the sampling of the instrumental intensity profiles is equidistant and the intensity values are given in points with a distance of  $\Delta K_{instr.}$ , the period of the instrumental Fourier transforms is  $\frac{1}{\Delta K_{instr.}}$ . This period determines the maximum  $L$  value for calculating the theoretical Fourier transforms: it has no sense to calculate the theoretical Fourier transform above this value and include the other maxima of the instrumental Fourier transform in the convolution. Therefore, the Fourier transforms are calculated with equidistant sampling from  $L = 0$  to  $L_{max}^{hkl}$ , where  $L_{max}^{hkl}$  is the  $L$  value where  $A_{instr.}^{hkl}$ , the Fourier transform of the measured instrumental profile has the first minimum value. This value is determined as follows: the (complex) instrumental Fourier transform,  $A_{instr.}(L)$  is calculated from  $L = 0$  by increasing  $L$  with small steps and in each point the integral  $I_{int}(L) = \int_{L'=0}^L |A_{instr.}(L')| dL'$  is calculated and the calculation is stopped if  $I_{int}(L)$  exceeds  $I_{instr.}(0) = I_{instr.}^{MAX}$ , the maximum intensity value of the instrumental profile. The so obtained  $L$  value is corresponding approximately to the second maximum of  $A_{instr.}(L)$ , so the correct value for  $L_{max}^{hkl}$  is half of this  $L$  value (where the instrumental Fourier transform has its first minimum value).

Fig. 5.7 shows the Fourier transform of a measured instrumental profile, the periodic function is plotted until its second maximum value. The period of this function is 1526 nm, which is in good agreement with the sampling of the measured instrumental profile: the instrumental peak is measured in equidistantly sampled points:  $\Delta K = 0.00065 \frac{1}{nm}$ , so the calculated period of the Fourier transform is:  $L_{NYQUIST} = \frac{1}{\Delta K} = 1538nm$ .

Depending on the value of  $L_{max}^{hkl}$ , the number of Fourier samples is:

$$N_{FT} = 2L_{max}^{hkl} \Delta K^P, \quad (5.4)$$

where:

$$\Delta K^P = \frac{2}{\lambda} \left[ \sin \left( \frac{2\theta_B + P}{2} \right) - \sin \left( \frac{2\theta_B}{2} \right) \right], \quad (5.5)$$

and the profile cutting parameter is denoted by  $P$  and the  $2\theta$  value of the peak center is denoted by  $2\theta_B$ . So by using this sampling the Fourier transforms are calculated equidistantly at points with a distance of  $\Delta L = \frac{L_{hkl}^{max}}{N_{FT}} = \frac{1}{2\Delta K^P}$  and the period of the inverse Fourier transform is  $\frac{1}{\Delta L} = 2\Delta K^P$ . This means that the peak intensity profile has minimums at the points  $K_B \pm \Delta K^P$  (where  $K_B = \frac{2 \sin \theta_B}{\lambda}$ ) and it is cut at these points. If  $P$  is small, this means that it is cut approximately at the points  $2\theta_B \pm P$ .

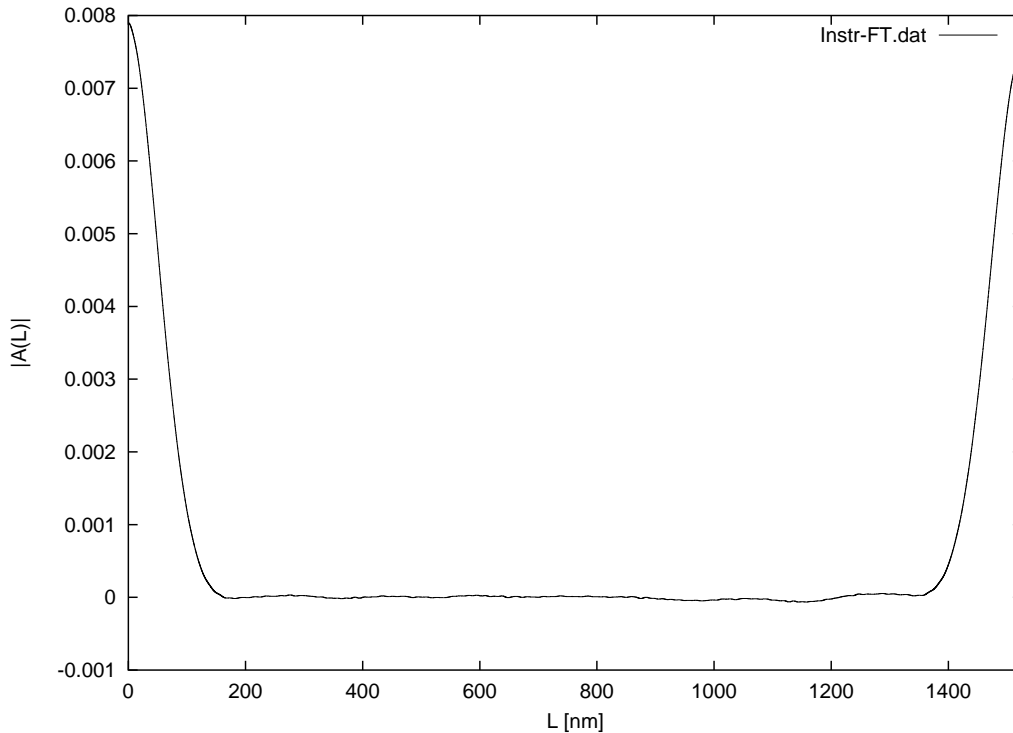


Figure 5.7: The absolute value of the Fourier transform of an instrumental profile as a function of  $L$ . It is plotted from  $L = 0$  until its second maximum value.

### 5.1.7 Sampling of the intensity patterns

In the least squares algorithm, the value of the theoretical intensity pattern is required at the  $2\theta$  values of the measured pattern data. However, since the measured pattern can contain many data points, by calculating the theoretical pattern only at relevant points and by using simple linear interpolation between these points, considerable speed-up can be achieved in the evaluation procedure. These relevant points are determined by two parameters:  $N_1$  is a parameter which represents an equidistant sampling in the measured  $2\theta$  range and the theoretical pattern is calculated in additional positions whose number is  $N_2$ . These points are selected around the measured peaks using the following algorithm:

1. the measured  $2\theta$  range is divided into  $N_1$  equidistant sub-intervals.
2. in each sub-interval additional points are added equidistantly where the theoretical pattern is also calculated. The integral of the background stripped measured pattern is calculated for

the  $n$ -th sub-interval. Denoting this integral by  $I_n$  and the whole area under the background stripped measured pattern by  $I_{pat}$ , the number of the additional sampling points added in the  $n$ -th sub-interval are:  $N_2 \frac{I_n}{I_{pat}}$ .

So the total number of sampling points is:  $N_1 + N_2$ .

### 5.1.8 The profile cutting parameter

The theoretical intensity profiles are calculated only in the points corresponding to the sampling determined by  $N_1$  and  $N_2$  (see the previous section for the details). Since the inverse Fourier transform is also periodic, the profiles cannot be calculated in the entire  $2\theta$  range, and the usage of a cutting parameter is necessary. It is noted that the inverse Fourier transform is periodical in  $K$  only and not in  $2\theta$ , this is the reason why the cutting is performed in  $K$  and not in  $2\theta$ . The profiles are evaluated only in the proximity of  $\Delta K^P$  of the corresponding Bragg positions, where  $P$  is the ‘‘profile cutting parameter’’ and  $\Delta K^P$  is defined by eq. (5.5). As we have seen in section 5.1.6, the period of the inverse Fourier transform is two times  $\Delta K^P$ , so it has a minimum value at the distance of  $\Delta K^P$ , where it is cut. The theoretical intensity pattern is put together from the background and the theoretical intensity profiles sampled in the manner described above.

### 5.1.9 Instrumental profiles

In the CMWP procedure  $I_{instr.}^{hkl}$ , the measured instrumental profiles corresponding to the  $hkl$  indices are used directly. The ideal sample for measuring the instrumental profiles has the following properties:

1. it should possibly have a large number of well separated Bragg reflections in the whole investigated  $2\theta$  angular range.
2. it should be strain free with a large enough grain size in order to avoid size broadening, this way it shows only the instrumental properties.

These conditions are more-or-less well satisfied in the case of  $LaB_6$  specimens provided by the National Institute of Standards and Testing (NIST). The CMWP evaluation program selects automatically the nearest instrumental profile to each of the peak center of the evaluated pattern. Since the overlapping between the peaks of the instrumental patterns is negligible, it is easy to separate the spectrum (e.g. with the program MKDAT, see section 4.1.2 for more details). Fig. 5.8 demonstrates the angular dependence of the instrumental broadening measured on the high resolution powder diffraction beam line, BM16 of ESRF in Grenoble, France (Martinetto, 2000). Fig. 5.9 shows a part of the instrumental pattern of a Philips X’Pert powder diffractometer measured on  $LaB_6$  sample.

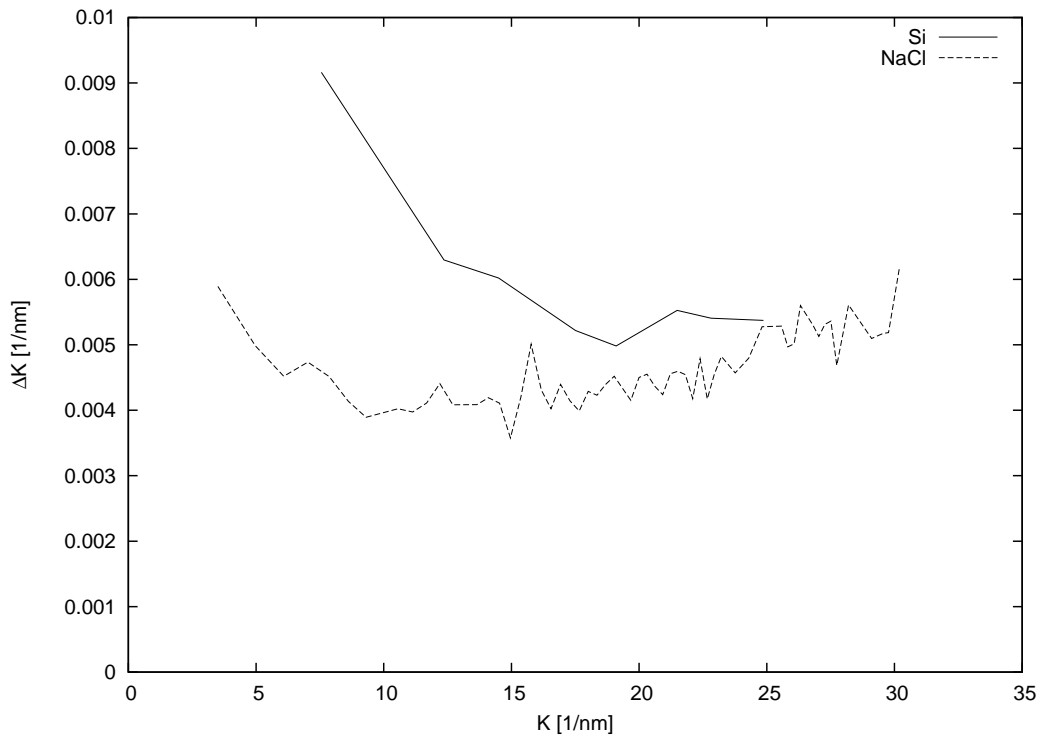


Figure 5.8: The FWHM values of the instrumental profiles measured on the high resolution powder diffraction beam line, BM16 of ESRF in Grenoble, France, as a function of  $K$  for Si and NaCl samples.

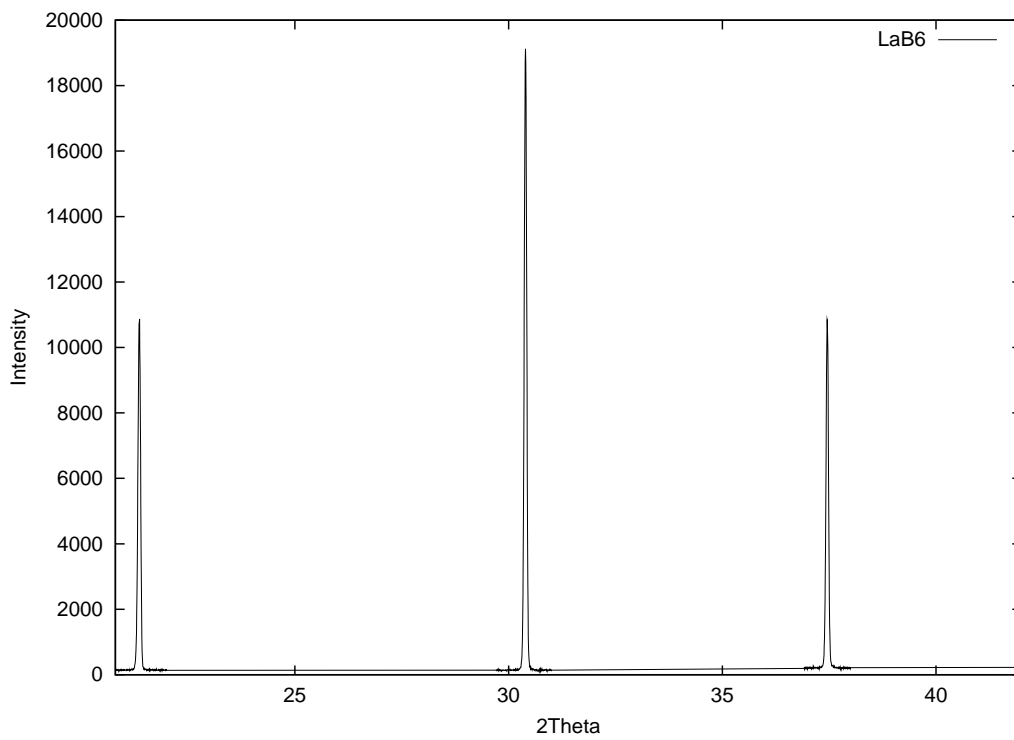


Figure 5.9: Part of the instrumental pattern of a Philips X'Pert powder diffractometer measured on a  $LaB_6$  sample.

### 5.1.10 Weighting algorithms

Without proper weighting the least squares algorithms are strongly influenced by the points with large  $y$  values (these points are overweighted). If the difference between the  $y$  values is significant, the usage of weighting is justified. In the MWP method the profiles are normalized, so there is no need for weighting. In the CMWP method the intensity of the measured peaks can be different by orders of magnitude.

The intensity maxima decrease with  $2\theta$  since the atomic scattering factors decrease with  $2\theta$  and, on top of that, the structure factor can also cause significant differences in the peak maxima. A further effect can be caused by texture. The CMWP program offers to use appropriate weighting if needed in order to take into account the peaks with smaller intensity maxima. In the least squares method the weights are usually  $1/y^2$ . A special weighting is used for the CMWP procedure in which the profiles are weighted uniformly (provided that the overlapping between the peaks is weak), however, the smaller peaks have larger weights. The weights are generated from the maximum intensity values according to the equation:

$$w_i(2\theta_i) = \max\{I_j^{MAX}, \text{ where } |2\theta_i - 2\theta_j| < P\}. \quad (5.6)$$

In this equation the  $I_j^{MAX}$  intensities are the background-stripped peak intensities,  $2\theta_j$  are the peak centers and  $P$  is the profile cutting parameter. The actual weights used in the least squares procedure are the  $\frac{1}{w_i^2}$  values.

Fig. 5.10 shows the intensity pattern and the corresponding  $w_i$  values for a  $CdF_2$  sample ball milled for 30 minutes as a function function of  $2\theta$ . By using these weights, the results provided by the CMWP procedure are in better correlation with the results of the MWP procedure, where the peaks are also uniformly weighted. It is noted that due to the different weighting algorithms, a difference is expected between the results of the MWP method on the intensity profiles, the results of the MWP method on the Fourier transforms and the results of the CMWP method. The usage of the weights  $1/y^2$  is also possible in CMWP, however this is not optimal if the level of the background is elevated.

### 5.1.11 Interpretation of the errors of the fitting parameters

In the least squares procedures the errors of the fitting parameters are usually given by their confidence levels. In the fitting algorithm of `gnuplot` (which is used by the MWP and CMWP procedures also) the error estimates of the parameters are given rather than confidence intervals. These error estimates are calculated from the variance-covariance matrix after the final step of the iterations. These estimates are the so called “asymptotic standard errors” (which are given by the program `gnuplot` at the end of the fitting). They are calculated as the standard deviation of each parameter. It should be noted, that these asymptotic standard errors are usually over-optimistic and therefore should not be used instead of the confidence levels. However, these asymptotic standard errors can be used as a qualitative measure of the fit.

The program `gnuplot` also gives a correlation matrix, which indicates the correlation of the parameters in the region of the solution. The meaning of the elements of the correlation matrix is: if the value of a parameter is changed, in this way increasing the WSSR, does the changing of the other parameter compensate? The elements in the main diagonal elements are always 1 (they correspond to autocorrelation) and if all parameters were independent, all other elements would be nearly 0. Two different parameters which completely compensate each other would have an element of unit magnitude, their sign is depending on whether the relation is proportional or inversely proportional. If the magnitudes of the non-diagonal elements are small, it means that the estimates of the standard deviation of each parameter are close to the asymptotic standard error given by `gnuplot`.

### 5.1.12 Convergence and numerical stability

By using the Marquardt-Levenberg nonlinear least squares algorithm MWP and CMWP tries to find the minimum value of WSSR in a multi dimensional parameter space (the dimension is denoted by  $n$  and it is the number of the fitting parameters). In the nonlinear Marquardt-Levenberg algorithm the gradient vector (whose components are the partial derivatives of WSSR as a function of the fitting parameters) is calculated and the parameter values are modified according to the direction of the gradient vector and a step parameter called  $\lambda$ . In order not to jump over the minimum - which would be the solution - the step is modified adaptively, i.e. after each step of the iteration,  $\lambda$  is either multiplied or divided by a numerical factor and, if the WSSR is better in the new point, the new value for  $\lambda$  is accepted. Depending on the properties of this  $n$ -dimensional surface, finding the physical minimum is not a trivial problem since local (non-physical) minimums can also be obtained. If this surface has a sharp minimum there is usually no problem. However if it is flat, there is a chance to find an inappropriate minimum. By changing the initial values of the parameters and examining the value of WSSR and the residuals corresponding to the final solution one can try if the solution corresponds to the absolute minimum or not.

In the following an example will be presented for the examination of the stability of the solution by running systematically selected fittings starting from different initial values of the parameters. Since practice has shown that in some cases it is difficult to get a solution for the dislocation parameters, the stability of the parameters  $d$  and  $e$  will be examined ( $d$  and  $e$  are related to the dislocation density and effective outer cut-off radius of dislocations, respectively).

Table 5.2 shows the examination of the solution of the CMWP fit for  $SrF_2$  sample ball milled for 30 minutes: the solution parameters are indicated for different initial values of the parameters  $d$  and  $e$  (the initial value of the other parameters was always the same:  $a = -1.3$ ,  $b = 1.7$  and  $c = 1.3$ ). It can be seen that the solution for this sample is well defined and unique: it finds approximately the same minimum starting from a wide range of the initial parameter values. However, at the same time, by using inappropriate values for the parameters used for the sampling of the theoretical Fourier transforms and/or the intensity pattern (e.g. for the profile cutting parameter) it is possible to get an unstable behaviour for the solution even in the case of the same sample.

Fig. 5.11 shows the WSSR corresponding to the solution of the CMWP fit for the same  $SrF_2$  sample

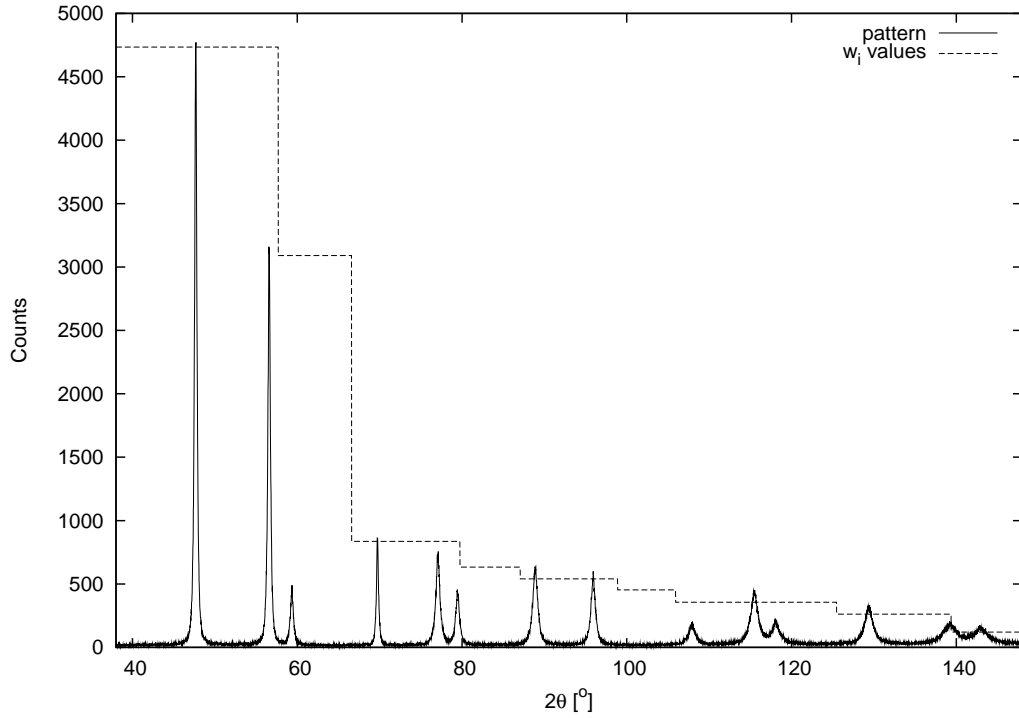


Figure 5.10: The measured pattern (solid lines) and the corresponding  $w_i$  values used in the CMWP algorithm (dashed line) for  $CdF_2$  sample ball milled for 30 minutes, as a function of  $2\theta$ . The actual weights are the  $\frac{1}{w_i^2}$  values.

$d_{ini}$	$e_{ini}$	$a_{sol}$	$b_{sol}$	$c_{sol}$	$d_{sol}$	$e_{sol}$	WSSR
4	0.5	-0.8062 (13%)	2.054 (1.6%)	1.204 (0.72%)	19.5 (21%)	0.87 (43%)	2.6698
6	0.4	-0.7934 (14%)	2.069 (1.4%)	1.200 (0.63%)	15.8 (17%)	-1.33 (34%)	2.6709
8	0.3	-0.8062 (13%)	2.054 (1.6%)	1.204 (0.72%)	19.5 (21%)	-0.87 (43%)	2.6698
10	0.25	-0.8062 (13%)	2.054 (1.6%)	1.204 (0.72%)	19.5 (21%)	-0.87 (43%)	2.6698
20	0.2	-0.8156 (13%)	2.044 (1.7%)	1.207 (0.74%)	21.5 (18%)	0.71 (37%)	2.6696
30	0.15	-0.8331 (13%)	2.028 (1.4%)	1.211 (0.62%)	24.4 (5.7%)	0.55 (12%)	2.6702
40	0.1	-0.8597 (13%)	2.005 (1.4%)	1.218 (0.61%)	28.1 (4.4%)	0.41 (8.9%)	2.6724
60	0.08	-0.8323 (13%)	2.028 (1.4%)	1.211 (0.61%)	24.4 (5.6%)	0.55 (11%)	2.6702
80	0.05	-0.8331 (13%)	2.028 (1.4%)	1.211 (0.62%)	24.4 (5.7%)	0.55 (12%)	2.6702
100	0.03	-0.8605 (13%)	2.005 (1.4%)	1.218 (0.61%)	28.1 (4.5%)	0.41 (9.1%)	2.6724

Table 5.2: The initial values ( $d_{ini}$  and  $e_{ini}$ ), the solution parameters ( $a_{sol}, \dots, e_{sol}$ ) and the WSSR values obtained as the solution of the CMWP fit for  $SrF_2$  sample ball milled for 30 minutes. The initial value of the other parameters was always the same:  $a = -1.3$ ,  $b = 1.7$  and  $c = 1.3$ . It is noted that the WSSR values have to be multiplied by a factor of  $10^7$ . The asymptotic errors of the fitting parameters are also indicated in parentheses.

as a function of the value of the  $d$  parameter (this value was fixed during the fitting and only the values of the other parameters were refined). It can be seen that it has a flat minimum value around  $d = 20$ . However if the same type of curve for a sample is monotonously increasing (so its derivative is always positive and does not reach zero at a particular  $d_{sol}$  value), when refining all parameters instead of a well defined solution, the parameter  $d$  approaches asymptotically zero (and at the same time  $e$  approaches asymptotically infinity). By fixing the value of  $de$  (which means that the value of  $M$ , the dislocation arrangement parameter is fixed) a solution can be obtained for  $\rho$ , however it is better to solve the problem without this (ad-hoc) restraint. These problems have several possible sources:

- the incorrect choice of the theoretical function is a possible cause
- the incorrect choice of the sampling parameters of the theoretical Fourier transform or theoretical intensity pattern should also be avoided
- the noise and low quality measurements have negative effects on the evaluation

In section 5.5 a solution for a similar stability problem will also be presented: by using a more appropriate physical model for the size broadening of these samples the unstable behaviour of the dislocation parameters can be eliminated.

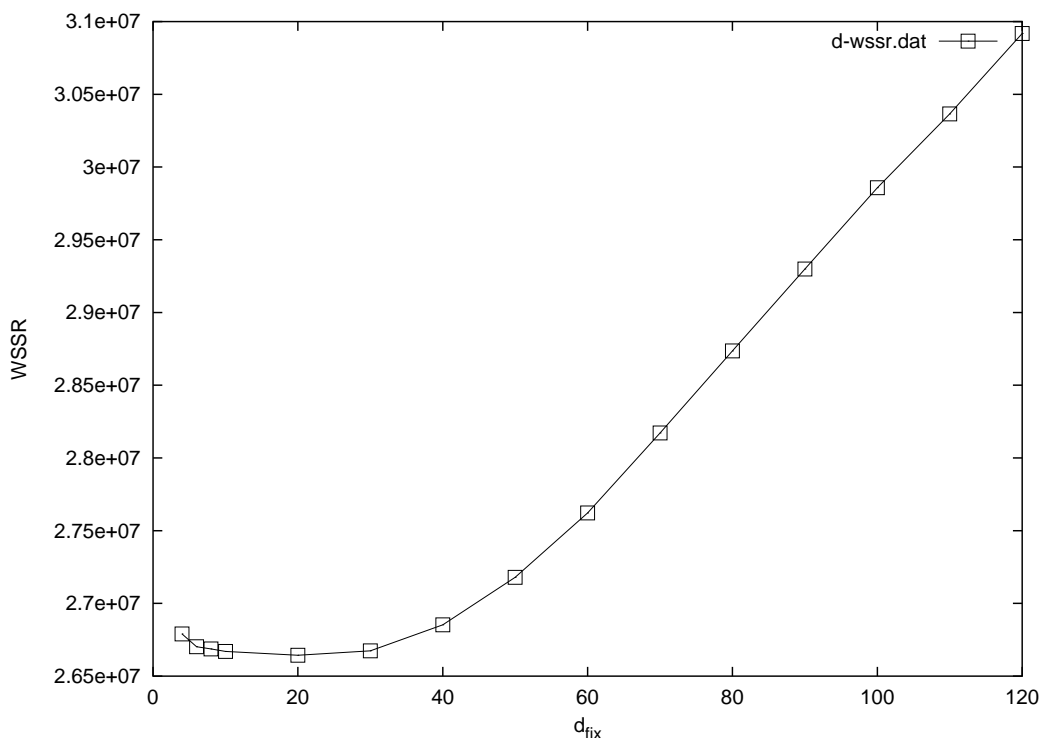


Figure 5.11: The WSSR corresponding to the solution of the CMWP fit for  $SrF_2$  sample ball milled for 30 minutes, as a function of the value of the  $d$  parameter (which was fixed during the fitting and only the value of the other parameters were refined).

## 5.2 Modeling asymmetric diffraction profiles

In this section a method suitable for modeling asymmetric line profiles is presented. It is based on *Mughrabi's composite model* (Ungár et al., 1984; Mughrabi et al., 1986) and an asymmetric strain profile is composed by the sum of two shifted strain profiles calculated by using the Wilkens model (Wilkens, 1970). The  $\rho$  parameters of these functions correspond to the dislocation density in the inner region of the cell and in the cell's wall, respectively. In this procedure only a single peak is analysed and the size broadening is neglected. The evaluation procedure consists of the following steps:

1. **Correction of the peak's center and normalization:** The center of gravity of the *measured* intensity profile  $I_m(s)$  is defined as:

$$\bar{s} = \frac{\int_{-\infty}^{\infty} s I_m(s) ds}{\int_{-\infty}^{\infty} I_m(s) ds}. \quad (5.7)$$

Therefore the area normalized and center *corrected* intensity profile is given by the transform:

$$I_c(s) = \frac{I_m(s - \bar{s})}{\int_{-\infty}^{\infty} I_m(s) ds}. \quad (5.8)$$

2. **Evaluation using the symmetrized theoretical intensity profile:** The size broadening of the profiles is neglected, so the theoretical Fourier transform becomes:

$$A(L, \rho, R_e^*) = \exp \left[ -\frac{\pi b^2}{2} (g^2 C) \rho L^2 f \left( \frac{L}{R_e^*} \right) \right], \quad (5.9)$$

Since  $A(L)$  is real and even function of  $L$ , its inverse Fourier transform, the theoretical intensity profile is real and even function of  $s$ :

$$I(s, \rho, R_e^*) = 2 \int_0^{\infty} A(L, \rho, R_e^*) \cos(2\pi Ls) dL. \quad (5.10)$$

Note that the theoretical intensity function  $I(s)$  is area normalized, since:  $\int_{-\infty}^{\infty} I(s) ds = A(0) = 1$ .

In this step  $I_c(s)$ , the area normalized and center *corrected* intensity profile is fitted by  $I(s - s_1^0, \rho, R_e^*)$ , so the value of the parameters  $s_1^0$ ,  $\rho$  and  $R_e^*$  is refined.

3. **Evaluation using the asymmetrical theoretical intensity profile:**

In this step, the theoretical intensity function  $I_{as}(s)$  is defined as:

$$I_{as}(s) = f_1 I(s - s_1, \rho_1, R_{e,1}^*) + f_2 I(s - s_2, \rho_2, R_{e,2}^*), \quad (5.11)$$

where:

$$\begin{aligned} f_1 + f_2 &= 1 \\ s_1 f_1 + s_2 f_2 &= 0 \\ f_1 \rho_1 + f_2 \rho_2 &= \rho \\ \left(R_{e,1}^*\right)^{f_1 \frac{\rho_1}{\rho}} \cdot \left(R_{e,2}^*\right)^{f_2 \frac{\rho_2}{\rho}} &= R_e^* \end{aligned} \quad (5.12)$$

The parameters  $\rho$  and  $R_e^*$  are known from the previous step, so the parameters  $f_2$ ,  $s_2$ ,  $\rho_2$  and  $R_{e,2}^*$  are determined unequivocally by the parameters  $f_1$ ,  $s_1$ ,  $\rho_1$  and  $R_{e,1}^*$ . In this step  $I_c(s)$  is fitted by  $I_{as}(s)$ , so the value of the parameters  $f_1$ ,  $s_1$ ,  $\rho_1$ ,  $R_{e,1}^*$  is refined and the value of the parameters  $f_2$ ,  $s_2$ ,  $\rho_2$ ,  $R_{e,2}^*$  is calculated using equations (5.12).

Although the method presented here was developed for single profile analysis, it was presented here, because the CMWP program package [S14] includes an evaluation program developed for this procedure.

### 5.3 CMWP application to Al-Mg alloys [S14, S16]

In [S14, S16] the CMWP fitting procedure is used for the evaluation of the X-ray diffraction patterns of Al-Mg alloys prepared by mechanical alloying. The microstructural parameters determined by the CMWP method were compared to the results obtained by the MWP fitting procedure. The aluminium-magnesium samples were prepared and measured as described in section 4.3 and in [S13]. In [S14] three samples were investigated, each after 3h ball-milling with nominal Mg concentrations 0, 3 and 6 at. %. The lattice constants of the ball milled samples were determined by the standard Nelson-Riley method (1945). The Mg concentration in the solid solution was determined by using the slope in Vegard's law (Pool & Axon, 1952). The true Mg concentrations were 0, 2.26 and 5.52 at. % for the samples with nominal Mg concentrations 0, 3 and 6 at. %, respectively.

Figs. 5.12 and 5.13 show the X-ray diffraction pattern obtained on the Al-3 wt.% Mg powder after 3 h ball milling in linear and logarithmic intensity scales, respectively. The open circles represent the experimental data. As it can be seen from the figure the main phase is the Al-Mg solid solution, however, traces of Mg around the first reflection of Al-Mg can be observed in the logarithmic plot. The solid line in Figs. 5.12 and 5.13 represent the model based, theoretical pattern fitted by the CMWP procedure. The agreement between the the measured and the fitted patterns is satisfactory. The severe plastic deformation during milling resulted in the formation of ultrafine-grained structure ( $\langle x \rangle_{vol}=39$  nm) with very high dislocation density ( $\rho = 44 \cdot 10^{14} \text{m}^{-2}$ ).

The microstructural parameters were determined for each sample by applying both the CMWP and MWP fitting methods. It was found that the microstructural parameters obtained by the MWP fitting method are in reasonable agreement with those determined by the CMWP fitting procedure, as it is shown in Table 5.3. The observed differences are due to the different weightings used in the MWP and CMWP procedures.

Table 5.3: Microstructural parameters obtained by the MWP and CMWP procedures for ball milled Al-xMg (x=0, 3, 6 wt.%) specimens

x [wt.%]	Method	$m$ [nm]	$\sigma$	$\rho$ [ $10^{14} \text{m}^{-2}$ ]	$M$	$q$
0	MWP	60 (6)	0.18 (2)	19 (2)	1.0 (2)	0.7 (1)
3	MWP	33 (3)	0.21 (3)	40 (4)	1.2 (2)	0.5 (1)
6	MWP	19 (2)	0.40 (3)	72 (6)	1.0 (2)	0.4 (1)
0	CMWP	73 (7)	0.10 (2)	12 (2)	1.1 (2)	1.3 (1)
3	CMWP	29 (3)	0.29 (3)	44 (4)	1.2 (2)	1.1 (1)
6	CMWP	26 (3)	0.13 (3)	100 (15)	1.3 (2)	0.7 (1)

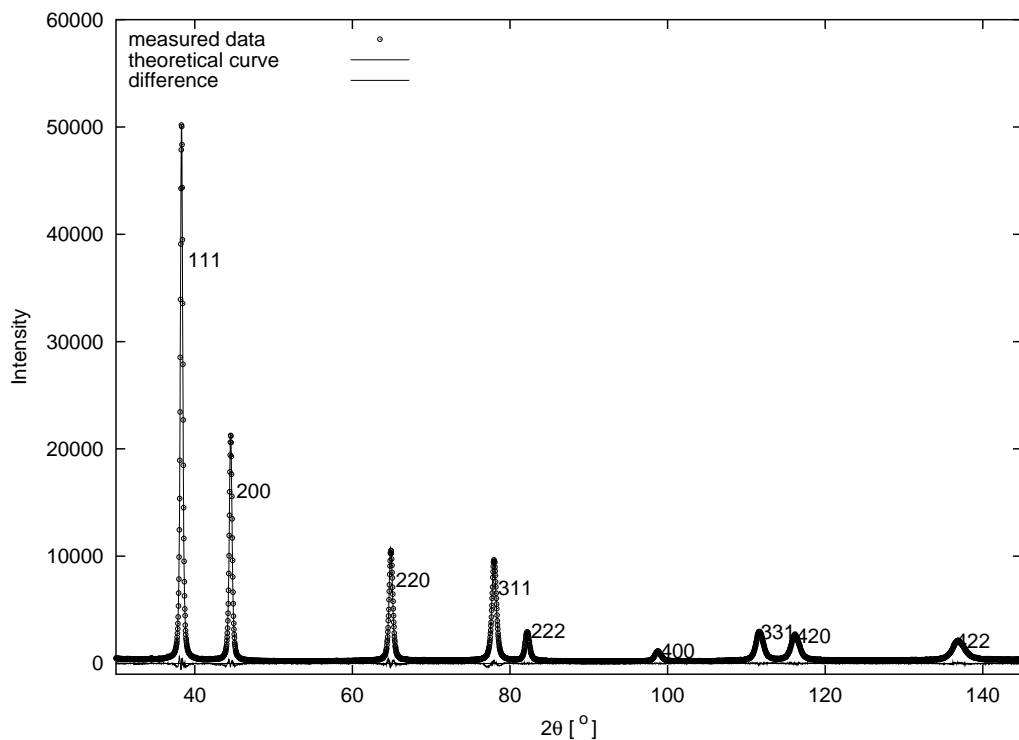


Figure 5.12: The measured and fitted patterns (fitted by the CMWP method) of the Al-3 wt.% Mg alloy. In this figure the intensity values are plotted as a function of  $2\theta$ . The indices of reflections are also indicated. The differences between the measured and fitted intensity values are plotted at the bottom of the figure.

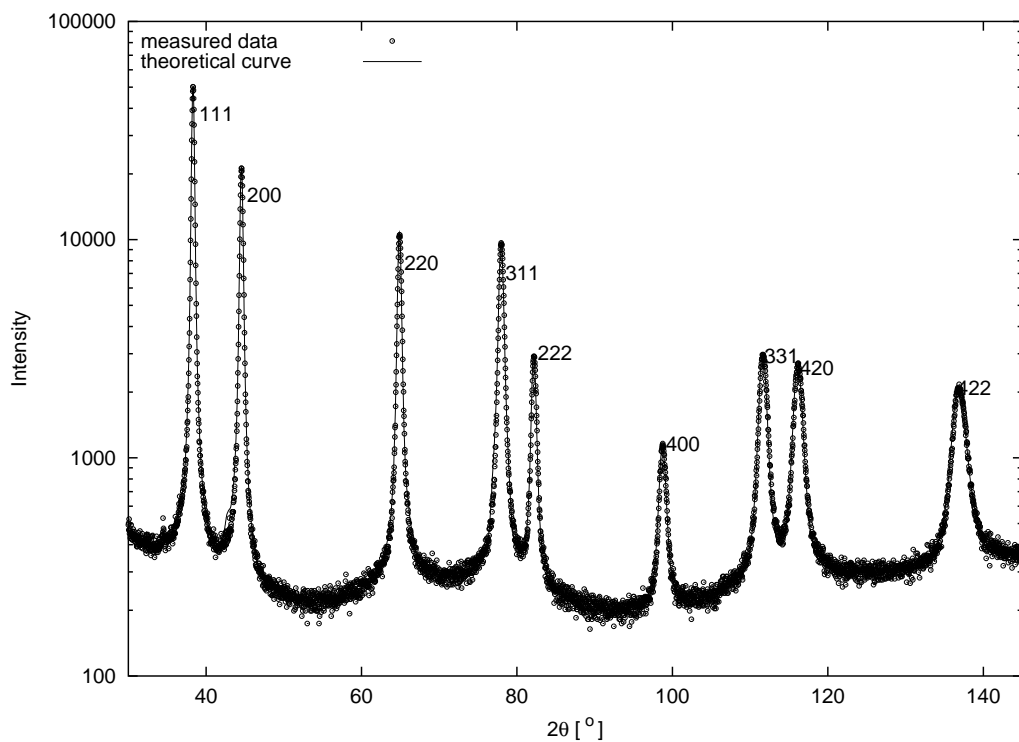


Figure 5.13: The measured and fitted patterns (fitted by the CMWP method) of the Al-3 wt.% Mg alloy (logarithmic intensity scale). In this figure the logarithm of the intensity values are plotted as a function of  $2\theta$ . The indices of reflections are also indicated.

## 5.4 CMWP application to nanocrystalline Cu containing planar faults [S18]

The effect of stacking faults and twins on X-ray diffraction patterns has been calculated numerically by using the DIFFaX software (Treacy et al., 1991) for the first 15 Bragg reflections in fcc crystals up to 20 % fault densities by Mr. Levente Balogh [S18]. It was found that the Bragg reflections consist of up to 5 sub-reflections which are broadened and shifted to different extent according to particular  $hkl$  conditions, for more details see section 2.4 and [S18]. Balogh has also shown that the sub-reflections can be well described by Lorentzian profile functions over an intensity range of about 4 to 5 orders of magnitude. It was further shown that this feature is in good correlation with the fact that stacking faults or twin boundaries act as boundaries of coherently scattering domains and that they cause homogeneous strain. In that sense faulting or twinning causes a kind of size broadening associated with homogeneous strain. About 15000 sub-reflections were evaluated and parametrized according to their FWHM and positions relative to the exact Bragg angles. The stacking faults profile function defined by eq. (2.78) and the calculated parameter files were incorporated into the CMWP software for evaluating planar faults together with dislocations and crystallite or subgrain size distributions [S18]. Bulk nanocrystalline copper specimens were prepared by inert gas condensation and hot compaction at Argonne National Laboratory (Ungár et al., 1998). They are denoted as  $O_2 - IS$ ,  $P_2 - IS$ , and  $N_2 - IS$  in the as-prepared state and  $P_2 - T$  and  $N_2 - C$  after tensile and compression tests, respectively. By applying the CMWP procedure with the inclusion of the stacking or twin faults effect the microstructure of these nanocrystalline copper samples were evaluated. The twin density obtained by the CMWP procedure is increasing up to a few percents as the grain size decreases. Fig. 5.14 shows the twin density as a function of the area averaged mean crystallite or subgrain size for the different specimens. It can be seen that when the subgrain size is larger than about 40 nm the twin density is close to zero, within experimental error. At subgrain-size values smaller than about 40 nm the twin density increases sharply and reaches values up to 6%. This means that in nanocrystalline Cu twinning becomes a substantial mode of deformation when the subgrain size becomes smaller than about 40 nm.

## 5.5 CMWP application to ball milled fluorides [S17]

Nanocrystalline fluorides are important because of their usage as sensor materials. Homogeneous nanocrystalline materials can be produced by ball milling and at the same time, the milling procedure also introduces several types of strains. In [S17] 4 different types of fluorides produced by ball milling for different milling periods were investigated by X-ray diffraction. About 20 diffraction patterns of  $CaF_2$ ,  $SrF_2$ ,  $BaF_2$  and  $CdF_2$  fluorides produced by ball milling were measured by a D500 Siemens high resolution powder diffractometer with incident monochromator. By applying the CMWP procedure, the microstructural parameters for size and strain broadening were determined. In about half of the cases, the measured and fitted diffraction patterns were in perfect agreement throughout the entire

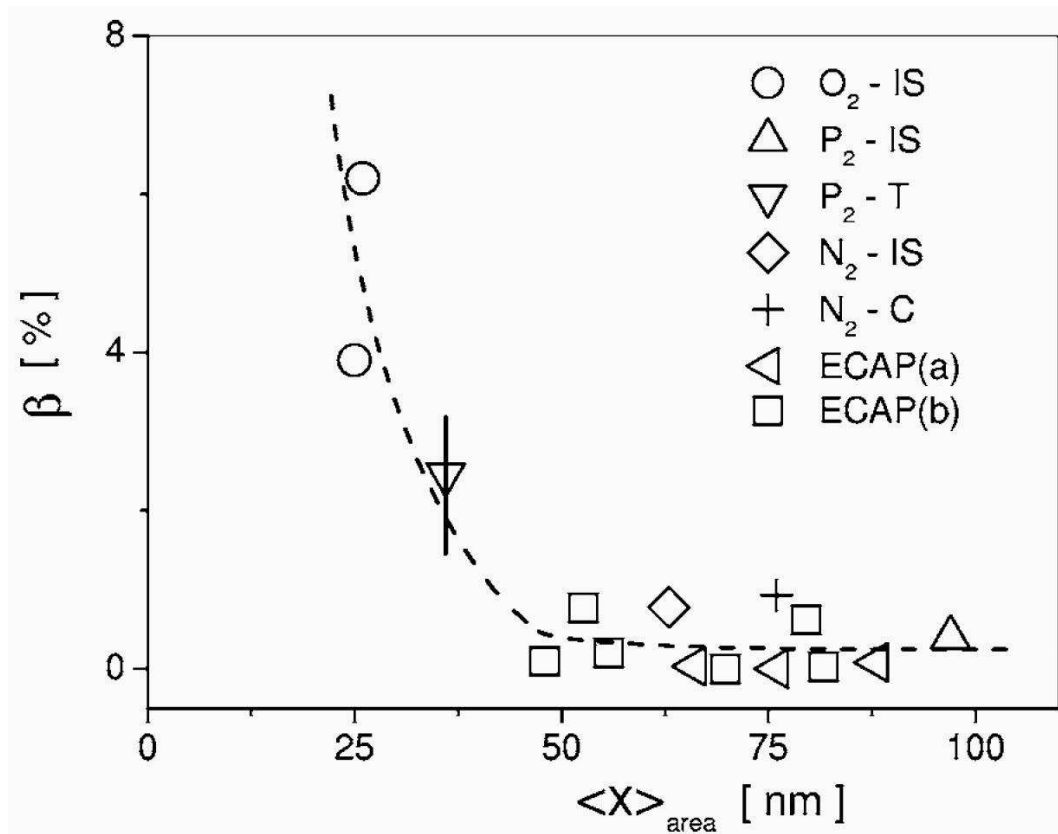


Figure 5.14: The twin density  $\beta$  as a function of the area averaged mean crystallite or subgrain size  $\langle x \rangle_{\text{area}}$  for the different specimens. Inert gas condensed and compacted specimens: O<sub>2</sub>-IS, P<sub>2</sub>-IS, P<sub>2</sub>-T, N<sub>2</sub>-IS, and N<sub>2</sub>-C. Submicron grain-size samples deformed by ECAP: ECAP(a) open left triangles and ECAP(b) open squares, respectively. The dashed line is to guide the eye. The solid vertical line indicates the experimental uncertainty.

$2\theta$  range. However, in the rest of the cases the first few reflections of the measured patterns were significantly narrower than the fitted ones, calculated on theoretical basis. At the same time, also in these latter cases, the rest of the reflections were in good agreement for the higher angular part of the patterns consisting of about 15 profiles. It is worth to note, that in the cases when the above mentioned differences between the measured and calculated patterns were observed, it was almost impossible to obtain a physically realistic solution for the microstructural parameters, i.e. it was not possible to determine the parameters of the strain effect: the solution for  $\rho$ , the dislocation density and  $R_e$ , the effective outer cut-off radius of dislocations was asymptotic as described in section 5.1.12. In the cases when the first few measured profiles were narrower than the calculated ones, this discrepancy were interpreted by an X-ray optical interference effect [S17] similar to what was observed by Rafaja et al. (2004) in nanocrystalline thin layers. The interference effect has been corrected successfully, either by (i) excluding the affected profiles from the evaluation procedure or by (ii) assuming a diffraction angle dependent apparent bimodal size distribution of crystallites [S17].

### 5.5.1 The interference effect

Rafaja et al. (2004) have observed recently an X-ray optical interference effect in nanocrystalline thin film of  $\text{Ti}_{0.38}\text{Al}_{0.62}\text{N}$ . As it can be clearly seen in the Williamson-Hall plot in Figure 6 of Rafaja et al. (2004), the broadening of the first few reflections (corresponding to the smallest  $g$  values) is significantly smaller than the broadening of the other reflections. This means that the apparent domain size corresponding to these peaks is increased due to an interference phenomenon, consequently these peaks are narrowed. The other peaks corresponding to larger  $g$  values are not affected by this interference effect, so their broadening corresponds to the real physical coherently scattering domain size. As pointed out by the authors, the effect was present in the cases when the following conditions were simultaneously present: (i) the coherently scattering domain size was less than about 5 nm, (ii) a texture was present in the sample and (iii) the absolute value of the diffraction vector was small. In the following a simple interpretation of the interference effect is presented. Fig. 5.15 shows the reciprocal lattice spots of two adjacent crystallites rotated to each other by a relatively small angle. The difference in their orientation also means that their reciprocal lattices are also rotated to each other by this small angle. Due to the small size of crystallites, the reciprocal lattice points are broadened (in the case of isotropic crystallite shape the extent of broadening is the same in each point). If the crystallite size is small, the broadening becomes large and if the difference in orientation is also small, the reciprocal lattice spots corresponding to small  $g$  vectors can overlap. Due to the increase of the coherently scattering region in the reciprocal lattice, the peaks corresponding to these points are narrowed. In Fig. 5.15 the encircled reciprocal lattice-spot pairs #1 and #2 are overlapping, so their peak profiles are narrowed and the others corresponding to larger  $g$  values (like spot pair #3) do not overlap anymore, so their peak profiles are not influenced by this interference effect. Consequently the coherently scattering domain size determined from these latter peaks corresponds to the appropriate crystallite size. This is the simple and direct reason why this effect influences only the first few reflections in a diffraction pattern, as can be seen in a direct way in Figure 6 of Rafaja et al. (2004).

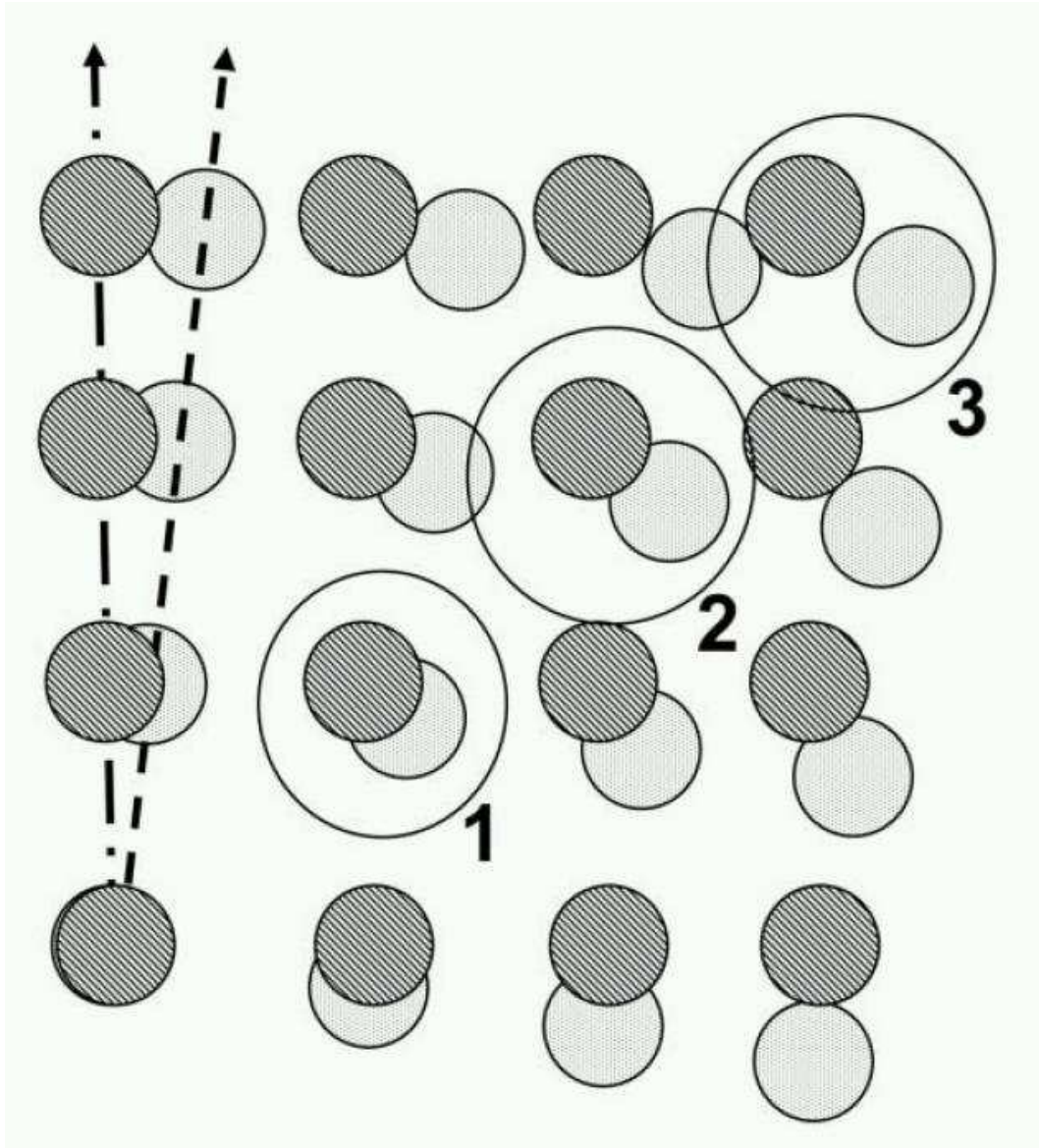


Figure 5.15: Schematic drawing for the interpretation of the interference effect. The dashed and the dotted spots are the blown up reciprocal lattice nodes corresponding to two adjacent crystallites rotated in orientation with respect to each other by a small angle. The orientations of the two crystallites are indicated schematically by the dashed and dash-dotted arrows. The pairs of encircled diffraction spots numbered #1 and #2 overlap, whereas those numbered #3 are well separated.

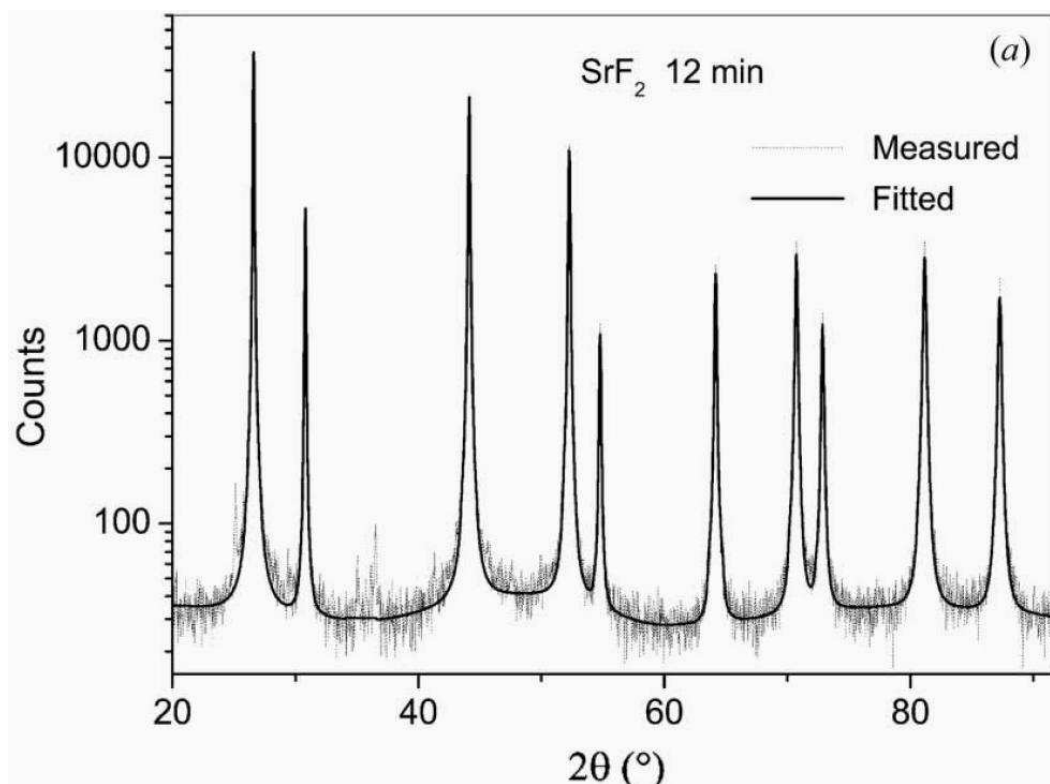


Figure 5.16: Observed and fitted patterns of  $SrF_2$  after 12 min of ball milling.

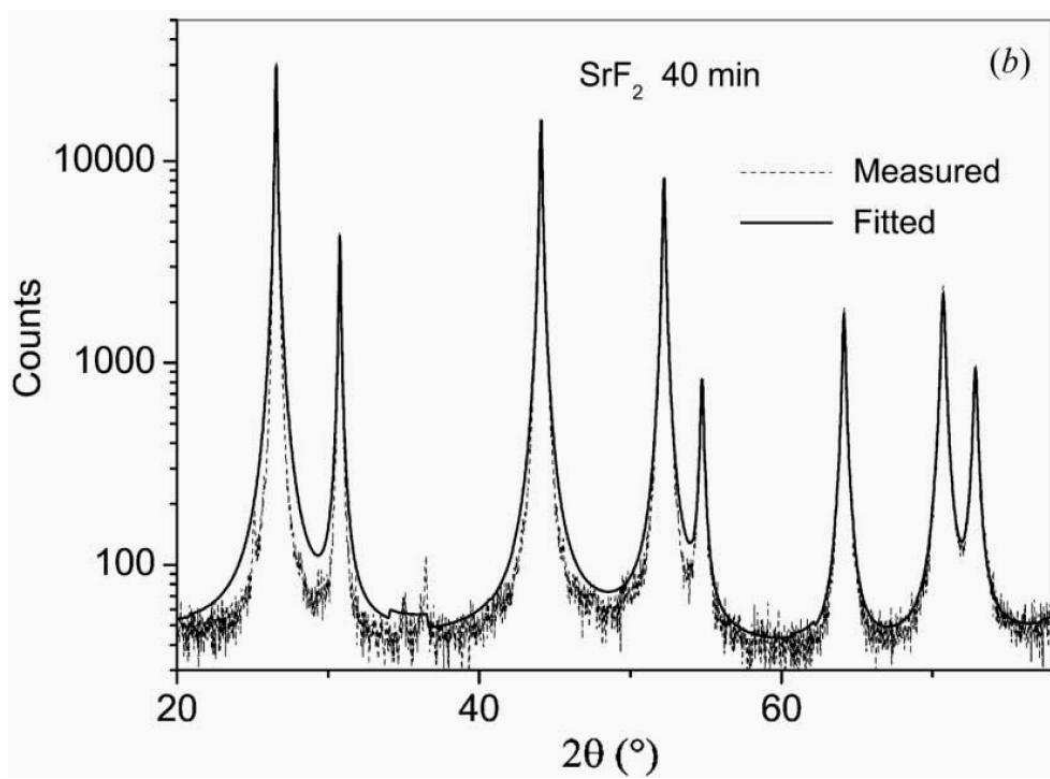


Figure 5.17: Observed and fitted patterns of  $SrF_2$  after 40 min of ball milling.

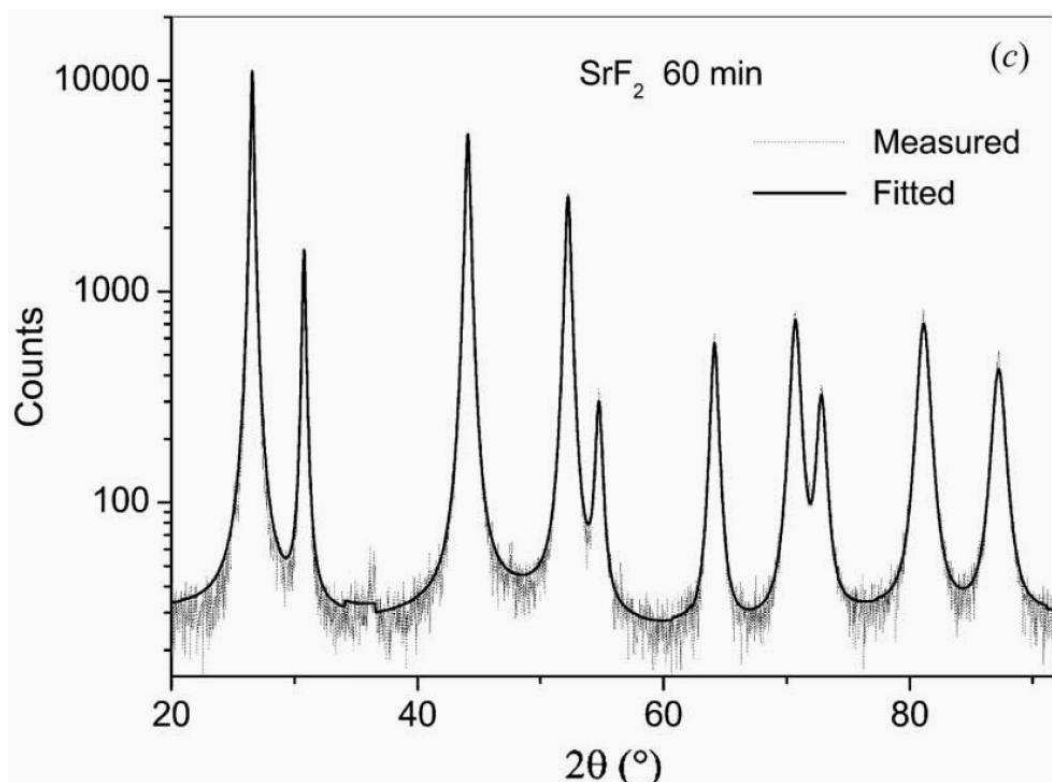


Figure 5.18: Observed and fitted patterns of  $SrF_2$  after 60 min of ball milling.

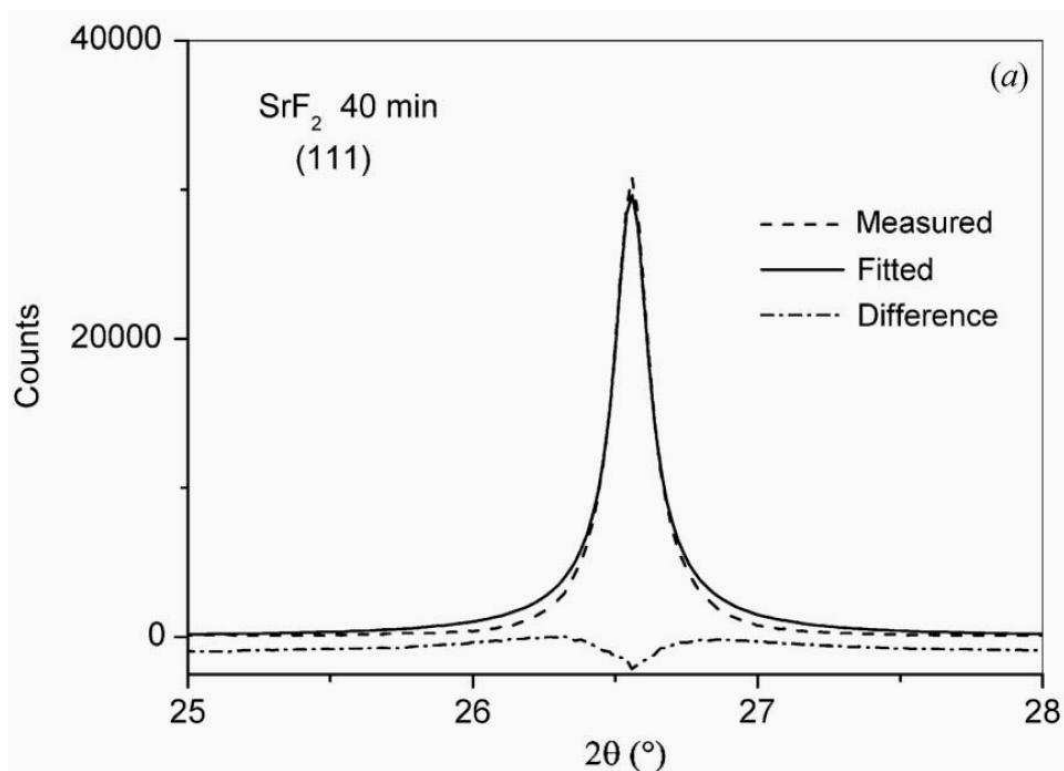


Figure 5.19: Observed and fitted profiles of the 111 reflection of  $SrF_2$  after 40 min of ball milling.

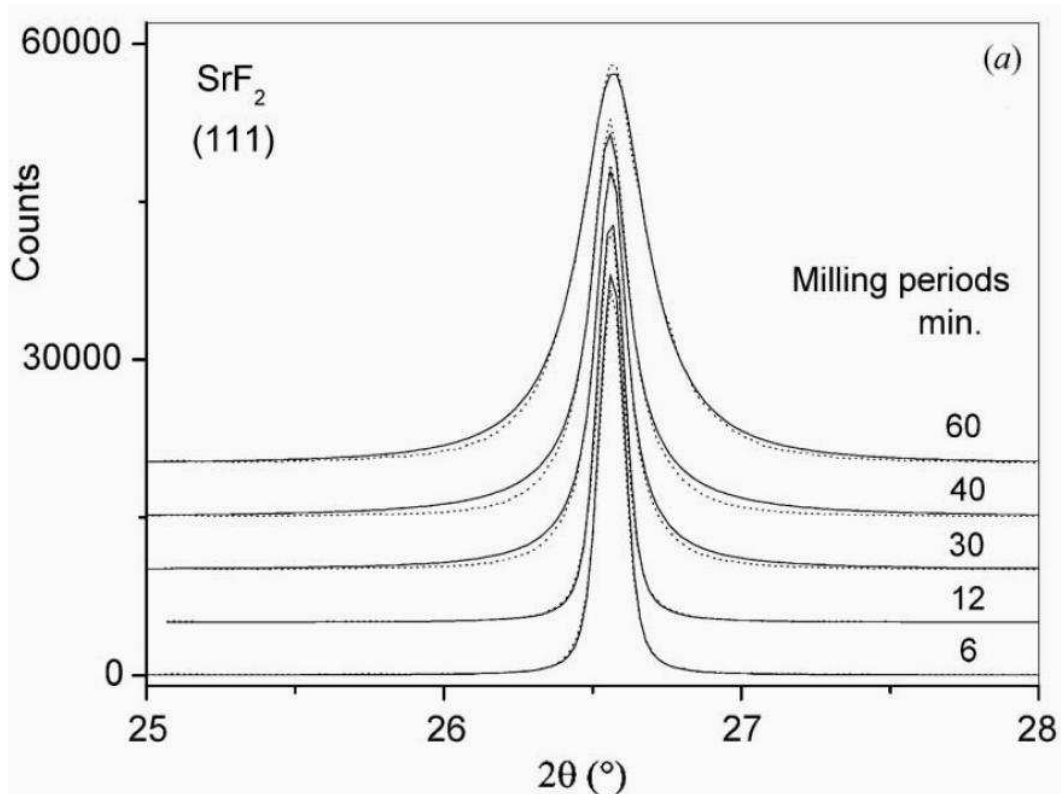


Figure 5.20: Evolution of the interference effect with milling periods for the 111 diffraction line of  $SrF_2$  samples.

The measured and fitted patterns of  $SrF_2$  samples corresponding to 12, 40 and 60 minutes of ball milling periods are plotted in Figs. 5.16, 5.17 and 5.18, respectively. As it can be seen in Fig. 5.16, the measured and the model based, theoretical patterns of  $SrF_2$  ball milled for 12 minutes are in perfect agreement throughout the entire  $2\theta$  range of the measurement. On the other hand, according to Fig. 5.17, there is significant difference between the measured and fitted curves of  $SrF_2$  ball milled for 40 minutes at lower  $2\theta$  angles, the first few measured profiles are significantly narrower than the fitted ones. Nevertheless, also in this case the agreement between the measured and fitted profiles for  $2\theta$  angles larger than about  $60^\circ$  is satisfactory. After even longer milling periods, e.g. after 60 min ball milling, as can be seen in Fig. 5.18, a similar discrepancy can be observed between the measured and fitted patterns as in the case of the 40 min ball milled sample, however, the differences are definitely smaller, meaning that the effect is less pronounced in this case. As can be seen in Fig. 5.19 showing the measured and fitted profiles of the 111 reflection of  $SrF_2$  ball milled for 40 minutes, far enough from the peak center the measured and fitted profiles coincide, so the problem cannot be related to the incorrect determination of the background level. This suggests that either the shape of the peak or the extent of broadening is incorrect. The evolution of the interference effect with milling periods is shown in Fig. 5.20. It can be seen that the differences are increasing up to 40 min and start decreasing at longer milling periods. The microstructural parameters obtained by the CMWP fitting procedure also show a discrepancy for the samples for which differences were observed. Instead of a well defined solution for the parameters of the microstructure, the solution for the dislocation density

and the effective outer cut-off radius of dislocations approaches asymptotically infinity and zero, respectively, so without applying some artificial restraints (e.g. by fixing the value of  $M$ ) one can get only a physically unrealistic solution. By omitting the first few reflections, the fitting procedure works well for the rest of the profiles and gives a reasonable solution. The observed differences between the measured and the model based, fitted patterns suggest the presence of a similar interference effect as observed by Rafaja et al. (2004) in  $\text{Ti}_{0.38}\text{Al}_{0.62}\text{N}$  thin films. However, in the case of these fine loose powder samples, there can't be a strong orientational correlation (real texture) between the particles, but a local orientational correlation (local texture) is possible between adjacent crystallites. If the ratio of these locally textured particles is large enough, it is producing a similar interference effect as the one observed by Rafaja et al. (2004). From this we can conclude that two main conditions make the existence of this kind of interference plausible. (i) A fraction of the fluoride powder consists of nanocrystalline particles. This condition is produced by ball milling. (ii) In this fraction of the powder the orientation of adjacent particles is crystallographically not too far from each other, in other words, there is a local texture in the powder. Since the lattice parameters of these fluorides are relatively large, the first few diffraction spots are relatively close to the origin of reciprocal space, meaning that this orientational correlation condition is not too strict. The orientational correlation between adjacent crystallites can be caused by the Coulomb interaction present in these ionic crystals. This can produce some kind of epitaxial interaction between adjacent crystallites resulting in a local orientation correlation between them. In ball milled cobalt, for example, epitaxially touching particles were observed by HRTEM (Yao & Thölén, 2000). For longer milling periods the milling procedure enables coagulation and/or coalescence of smaller particles thus increasing the average crystallite size and diminishing the magnitude of the interference effect.

### 5.5.2 Correcting for the interference effect

The angular dependence of the apparent size distribution in the case of the  $\text{SrF}_2$  sample ball milled for 40 min (where the interference effect is the most pronouncedly present) was examined as follows: with fixed strain parameter values, the peaks were fitted individually and the lognormal size distribution parameters were determined for each profile. The  $m$  and  $\sigma$  values obtained this way are shown in Fig. 5.21 as a function of  $g$ . It can be seen that  $m$  decreases strongly whereas  $\sigma$  is slightly increasing in good correlation with the model in section 5.5.1.

The interference effect was corrected for by the following two fundamentally different approaches. (i) The first two reflections were omitted from the fitting, thus the remaining peaks, which were practically not affected by the interference effect provided the correct microstructural parameters. (ii) In accordance with the model of the effect of interference on the diffraction patterns, it is assumed that a fraction of the powder has an apparent crystallite size larger than the true value. Furthermore it is assumed that the fraction of the crystallites affected by the interference effect and the rest of the powder, both can be described by separate size distributions. Latter are denoted by  $f_1(x)$  and  $f_2(x)$ , respectively. A decaying mixing parameter  $\xi$  is introduced in order to describe the angular dependence of the interference effect. The effective size distribution function,  $f_{eff}$  is obtained as the

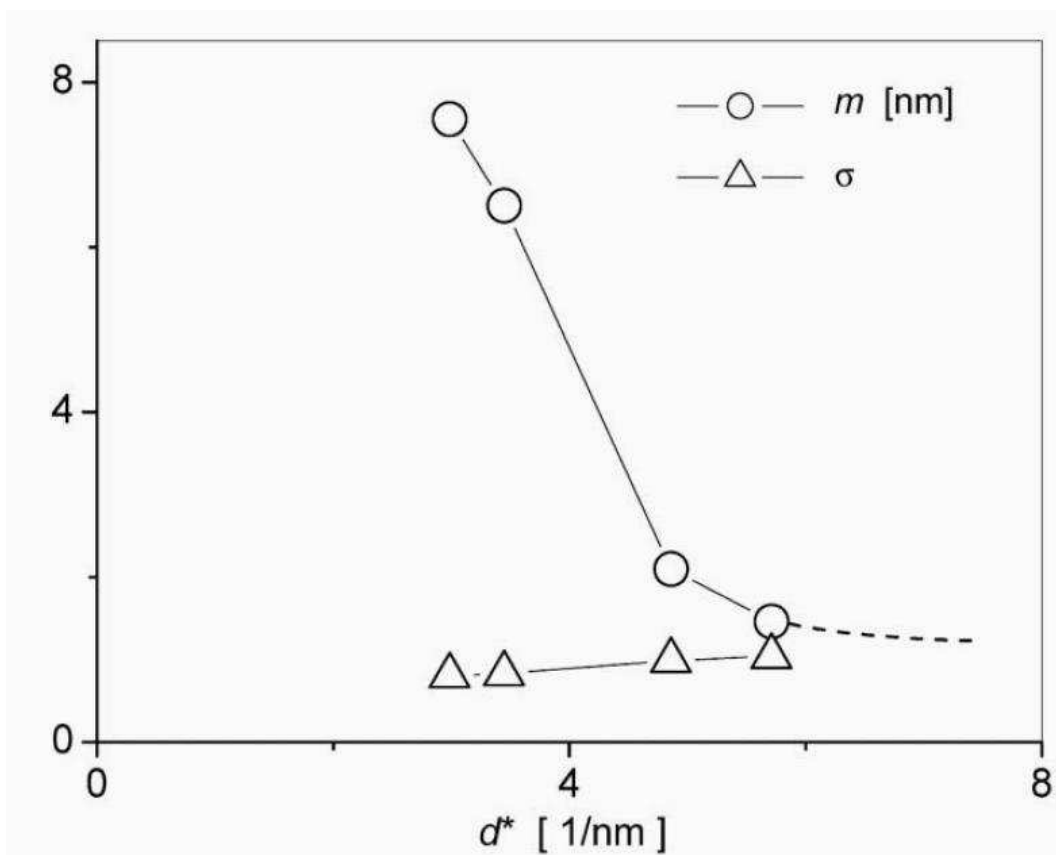


Figure 5.21: The  $m$  and  $\sigma$  size parameters, determined individually for the first few profiles in the diffraction pattern of  $SrF_2$  ball milled for 40 min, as a function of  $g$  ( $g = 2\frac{\sin\theta}{\lambda}$ ).

weighted sum of  $f_1(x)$  and  $f_2(x)$ :

$$f_{eff}(x) = \xi f_1(x) + (1 - \xi) f_2(x) \quad (5.13)$$

The simplest and most plausible selection for the size distribution functions is the lognormal function, so  $f_1(x)$  and  $f_2(x)$  are described by lognormal size distribution functions with the median and variance parameters:  $m_1, \sigma_1$  and  $m_2, \sigma_2$  respectively. Eq. (5.13) shows that the effective size distribution is a  $g$  dependent bimodal size distribution function in which the apparent part disappears with  $g$ . The numerical analysis was shown that the  $g$  dependence of the mixing parameter  $\xi$  was well described by a simple Lorentzian function of  $\frac{g-g_0}{g}$ :  $\xi = \frac{1}{1+As^2}$ , where  $s = \frac{g-g_0}{g}$ ,  $g_0 = 2 \sin(\theta_{111})/\lambda$  and  $2\theta_{111}$  is the Bragg angle of the 111 reflection. By using this correction considerable improvement of the quality of the fitting was achieved. A typical example of the fitting with this correction, corresponding to  $SrF_2$  ball milled for 40 min is shown in Fig. 5.22 which has to be compared to the uncorrected fit plotted in Fig. 5.17.

It is also noted that by using this correction the fitting was stable and gave reasonable values for the microstructural parameters without applying any restraints or omitting any part of the patterns. In the following the microstructural parameters obtained by using this correction are analyzed.

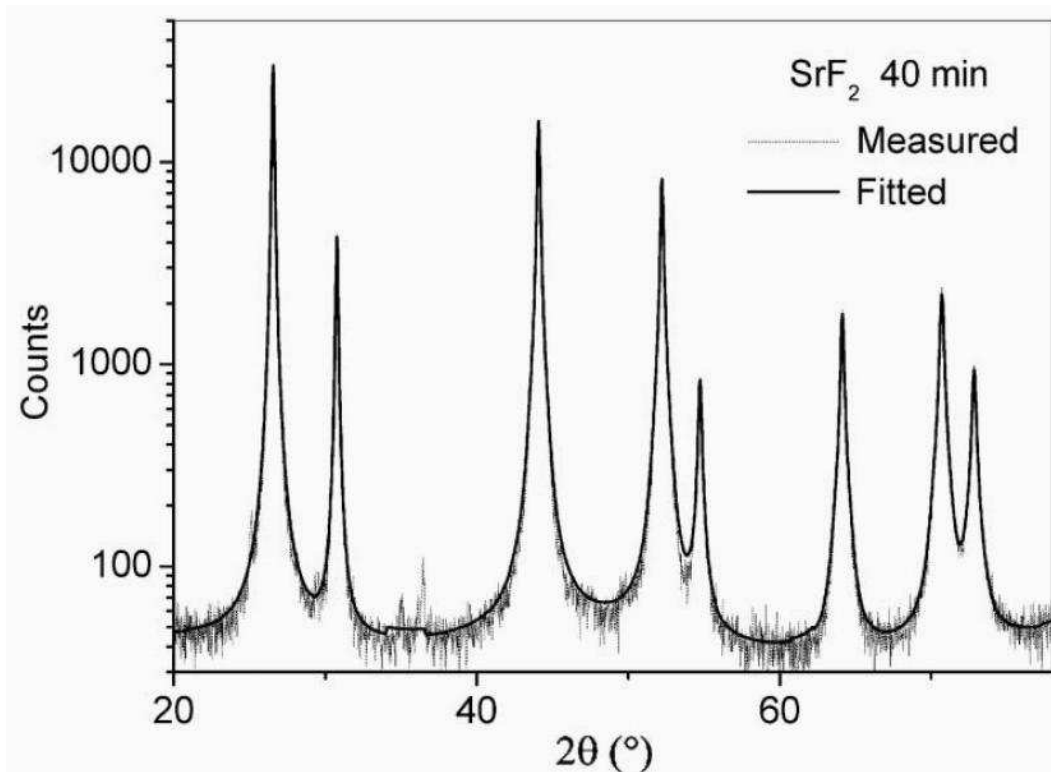


Figure 5.22: Fitting with correction for the interference effect for  $SrF_2$  ball milled for 40 min.

### 5.5.3 The microstructure of the fluorides

Figs. 5.23 and 5.24 show typical lognormal distribution functions for the ball milled  $SrF_2$  specimens according to the parameters  $m$  and  $\sigma$  given by the CMWP procedure. The figures show that after shorter ball milling periods, i.e. about 6 and 12 min, the specimens consist of almost monodisperse and relatively large crystallites. At longer ball milling periods the size distributions indicate that the size of crystallites collapses dramatically. At the longest ball milling periods a slight re-increase of the crystallite size can be observed, see Fig. 5.24. This small but definite re-increase has been observed in three fluorides:  $SrF_2$ ,  $BaF_2$  and  $CaF_2$ . It means that during the ball milling of these fluorides the particles are first fragmented and subsequently become welded again. Similar behaviour during ball milling has been observed frequently in the literature. Guerrero-Paz & Jaramillo-Vigueras (1999) ball milled ductile materials such as Cu, Ni and Cu-Ni alloys and observed coalescence of grains after longer milling periods by TEM investigations. Rác and coworkers (2005) ball milled dodecaphosphoric acid (HPW) and Nafion-H for catalytic purposes. Authors claim that because of coalescence catalysts with high catalytic performance require the use of optimal milling time. Coalescence during ball milling was also observed by Pál et al. (1986). Janot & Guerard (2005) also observed coalescence during ball milling of anodic materials for lithium-ion batteries. They state the importance of surface energy in the procedure of coalescence. The importance of coalescence is well known in the process of sintering, where surface energy is one of the controlling parameters (Wakai & Aldinger, 2003). The area weighted mean crystallite size values,  $\langle x \rangle_{area}$ , as a function of the milling period are shown in Fig. 5.25 for the different fluorides. The figure shows that  $\langle x \rangle_{area}$  decreases first with the milling period and after a minimum value it re-increases slightly in accordance with the size distribution functions. The absence of the slight re-increase of the crystallite size in  $CdF_2$  might be due to the rather long incubation period observed in the evolution of the dislocation density discussed in detail below. The evolution of the dislocation density,  $\rho$ , with milling period is shown in Fig. 5.26. In the initial state of the as-grown crystals the dislocation density is practically zero, i.e.  $\rho < 10^{14}m^{-2}$ , this value is marked schematically in the lower left corner of the figure. The figure indicates that the investigated fluorides fall into two different groups. (i) In the case of  $BaF_2$  and  $SrF_2$  the dislocation densities increase almost monotonously up to about  $7 \cdot 10^{15}m^{-2}$  during the first 30 min milling period and saturate for the rest of the milling procedure. (ii) In the other group,  $CaF_2$  and  $CdF_2$ , during the first 6 to 12 min ball milling  $\rho$  increases to about  $2.5 \cdot 10^{15}m^{-2}$  where it saturates for about 20 and 30 min in the case of  $CaF_2$  and  $CdF_2$ , respectively. After this intermediate plateau the dislocation density increases again during further ball milling and reaches the same large values of  $\rho$  as in the case of the other two fluorides. The figure suggests that after even longer milling periods also in these two fluorides, i.e. in  $CaF_2$  and  $CdF_2$ , the dislocation densities would saturate at around values of  $7 \cdot 10^{15}m^{-2}$ . The presence of an incubation period in the milling procedure of  $CaF_2$  and  $CdF_2$  is unequivocally present. A much weaker, however, existing short incubation-like stage in the case of  $BaF_2$  and  $SrF_2$  can also be observed, as shown in Fig. 5.26. The latter lasts up to about 12 minutes. The incubation periods in the evolution of the dislocation densities can be correlated to the homologous temperatures of the fluorides,  $T_{hom} = \frac{T_{RT}}{T_m}$  (where  $T_{RT}$  and  $T_m$  are room

temperature,  $T_{RT} = 300K$ , and melting temperature, respectively). In Fig. 5.27 the incubation periods are plotted versus the homologous temperatures. A good correlation between the two parameters can be seen. The rapid increase of  $\rho$ , without longer incubation periods can be observed in the case of  $BaF_2$  and  $SrF_2$  with the lowest  $T_{hom}$  values. On the other hand, the lengths of the incubation periods increase monotonously with  $T_{hom}$ . Based on these observations the development of the dislocation density can be discussed as follows. At the very beginning of ball milling a rapid production of dislocations is necessary in order to enable plastic deformation. In the case of  $CaF_2$  and  $CdF_2$ , once a relatively large number of dislocations (about  $2.5 \cdot 10^{15}m^{-2}$ ) are present, due to the higher  $T_{hom}$  and lower  $T_m$ , it can be assumed that the existing dislocations are mobile and plastic deformation can proceed relatively easily without further increase of  $\rho$ . However, at the end of the incubation period, further plastic deformation needs even more dislocations, therefore  $\rho$  increases rapidly again up to values of about  $7 \cdot 10^{15}m^{-2}$ . In the case of  $BaF_2$  and  $SrF_2$ , where  $T_{hom}$  is lower and  $T_m$  higher, the mobility of dislocations is considerably restricted as compared to the other two fluorides. Therefore, plastic deformation can only be enabled by intensive dislocation production resulting in a rather short incubation-like stage followed immediately by further rapid increase of  $\rho$ . Finally, this rapid increase is followed by the saturation of  $\rho$  at about  $7 \cdot 10^{15}m^{-2}$  which is close to the theoretical maximum value of average dislocation densities (Essmann et al., 1981).

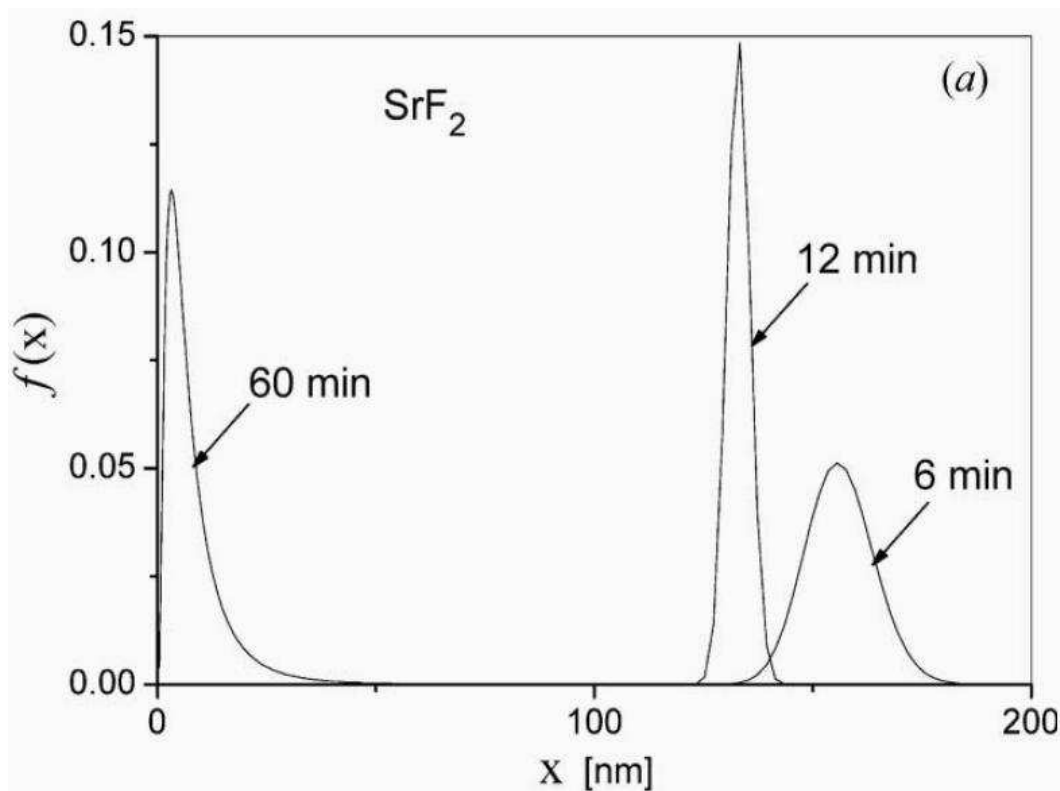


Figure 5.23: Size distribution functions of  $SrF_2$  samples ball milled for 6, 12 and 60 min.

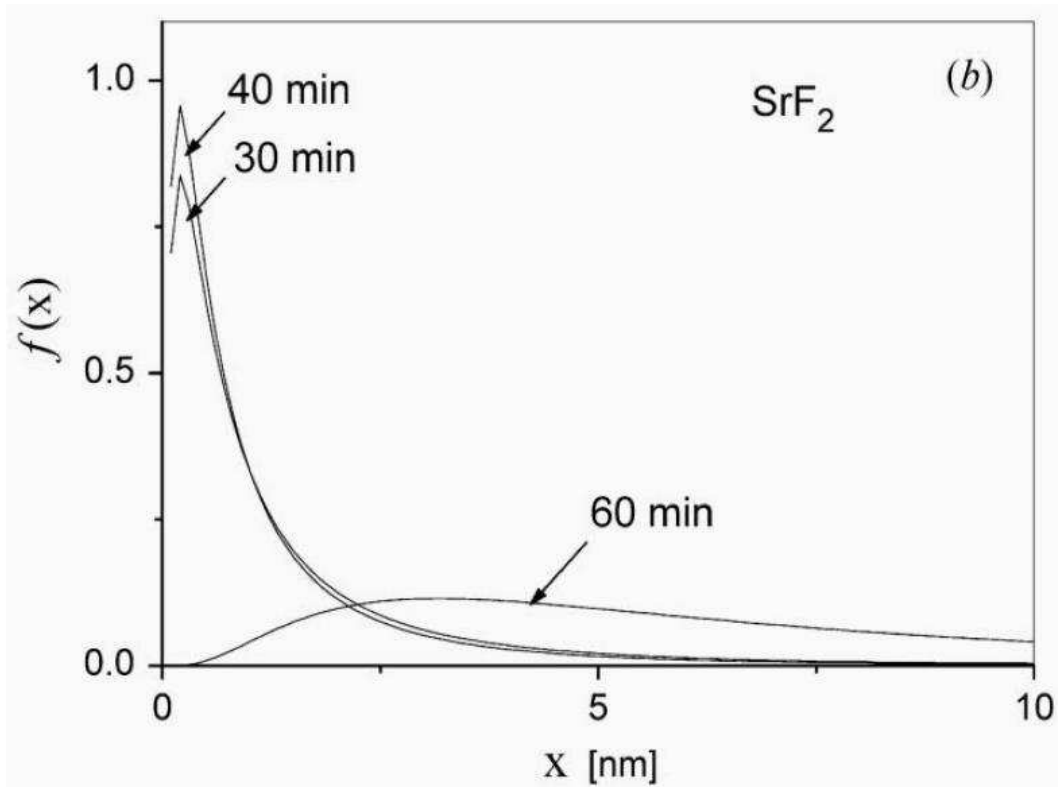


Figure 5.24: Size distribution functions of  $SrF_2$  samples ball milled for 30, 40 and 60 min.

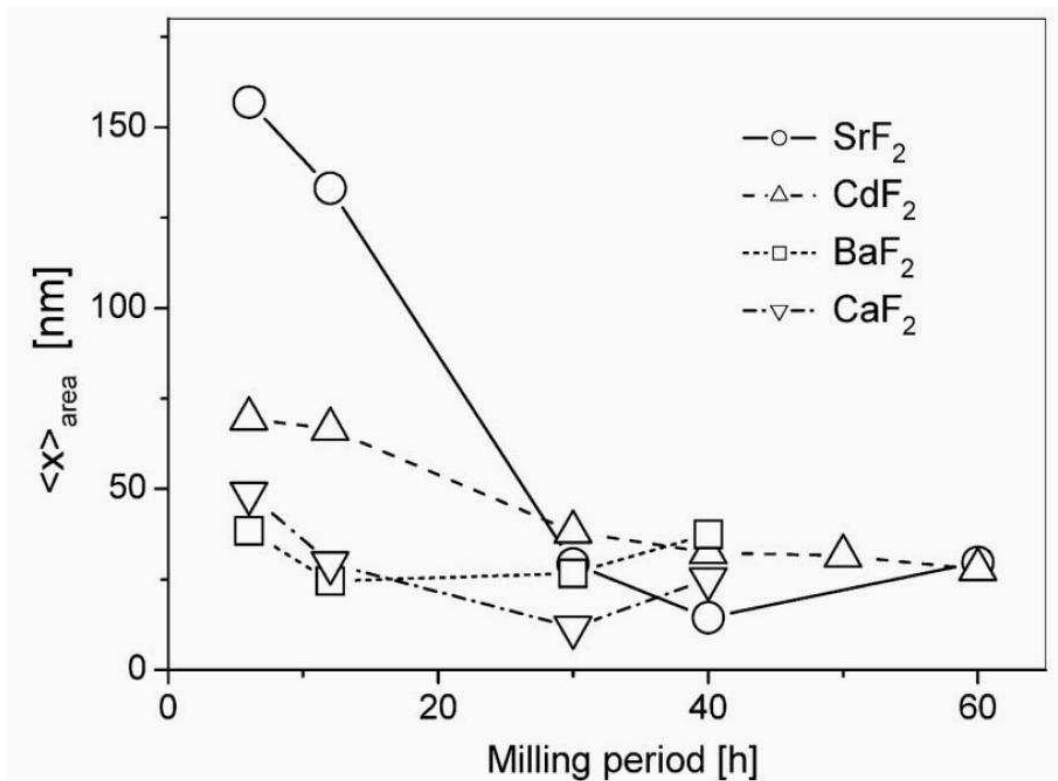


Figure 5.25: The area averaged mean crystallite size as a function of milling period for the different specimens.

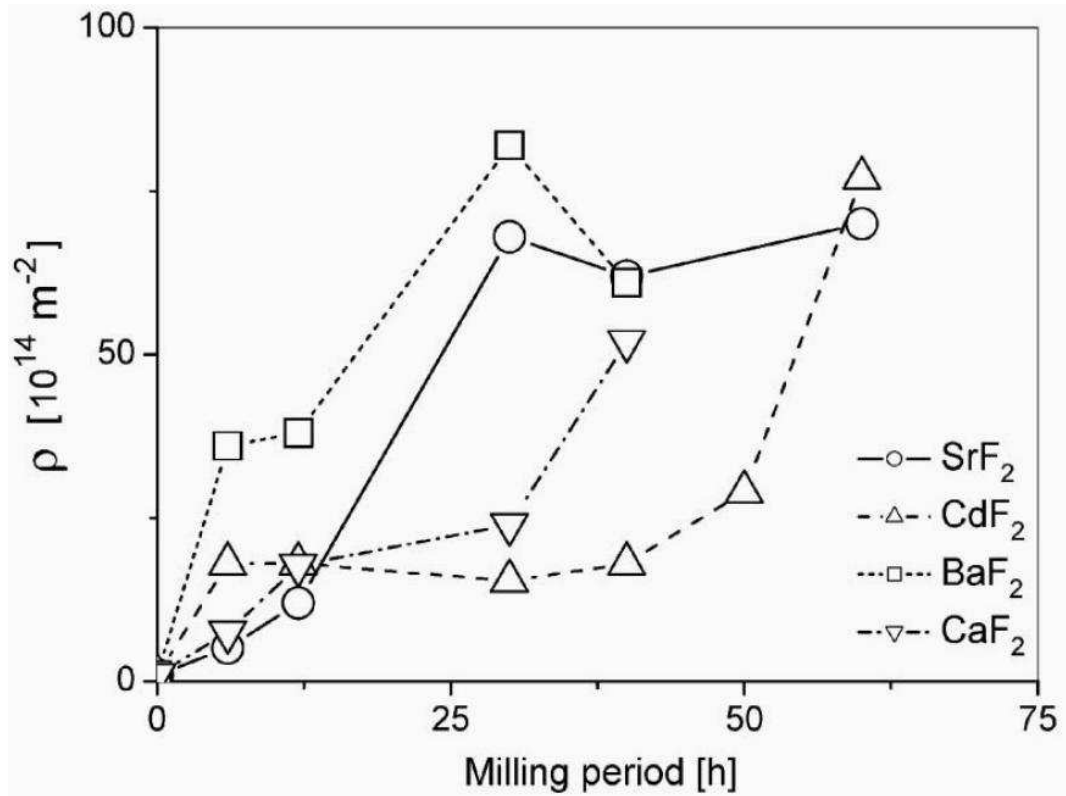


Figure 5.26: The dislocation density as a function of milling period for the different specimens.

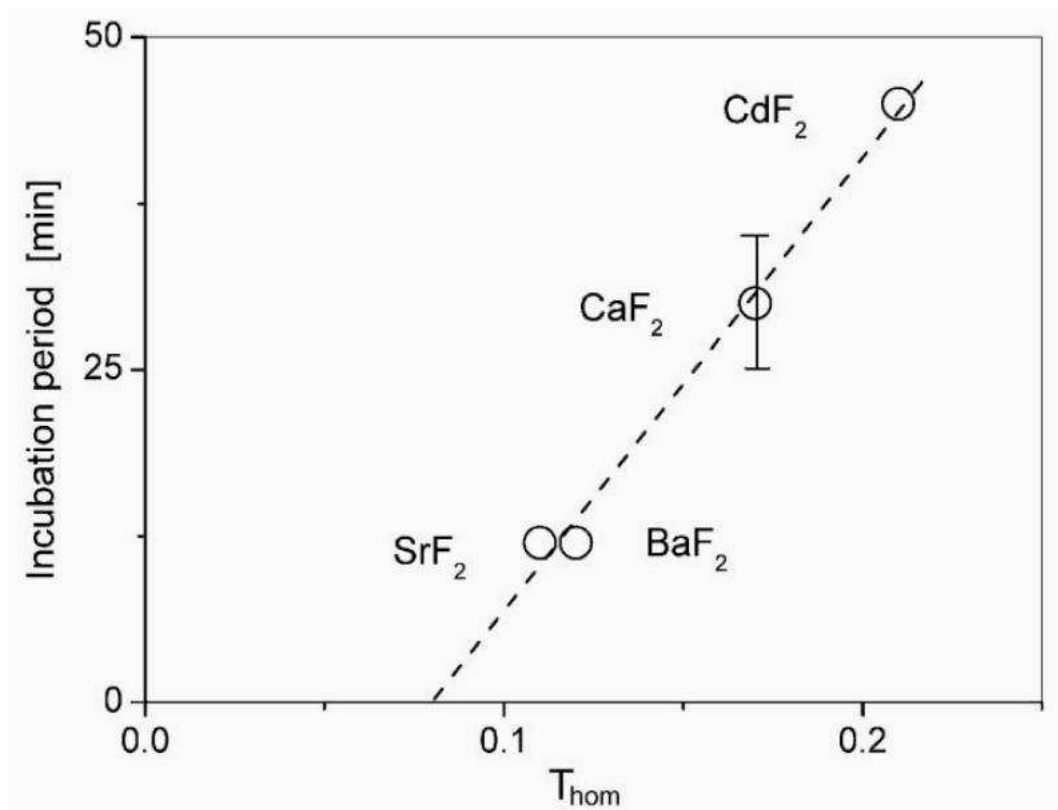


Figure 5.27: The incubation period as a function of homologous temperature.

# Chapter 6

## Summary and Conclusions

Most of the physical properties of crystalline materials are fundamentally determined by the microstructure. The most important fundamental microstructural properties are the type, density and distribution of crystal defects and the grain or crystallite structure. X-ray line profile analysis (XLPA) is one of the most important and powerful alternative methods besides electron microscopy for the characterization of microstructures.

This dissertation presents the theoretical models of the microstructure, the classical methods of XLPA and my newly developed methods, the MWP and CMWP procedures, which are based on the modeling of the physical properties of the different crystal defects. Several applications are presented in order to show the efficiency of the MWP and CMWP methods.

- The theoretical models of the microstructure are presented in Chapter 2: the size broadening of the profiles is calculated for the most important crystallite shapes and lognormal crystallite size distribution. The Fourier transform of the size profile is also given. The Wilkens model of dislocations is a sophisticated model for the description of the strain profile corresponding to a physically realistic dislocation configuration. By linking it with the theory of strain anisotropy, the model can be applied for a general description of strain broadening of diffraction peaks. The broadening caused by planar faults is also discussed.
- Chapter 3 gives a review of the classical methods of XLPA. The basic breadth and Fourier methods: the classical and modified Williamson-Hall methods and the classical and modified Warren-Averbach procedures are presented. The recently developed full profile and whole pattern fitting methods and the moment methods are also presented.
- Chapter 4 describes the MWP method, which is a Fourier method, based on the modeling of the physical properties of the X-ray diffraction profiles for the different crystal defects. By comparing the so obtained model based line profiles with the measured ones the method gives the microstructural parameters of the investigated materials. The steps of the data preparation and the steps of the MWP evaluation procedure are presented. Several applications of the

method have been selected and the results provided by MWP have been compared to the results of other microstructural methods, e.g. electron microscopy.

- In Chapter 5, the CMWP method is presented, which is also based on the modeling of the physical properties of the different crystal defects, but instead of fitting the separated peak profiles, it works directly on the measured intensity pattern. By comparing the model based pattern to the measured one the microstructural parameters are determined. The principles of the method, the steps of the evaluation procedure and the several available frontends of the CMWP program are presented. The details of the numerical procedure, e.g. the determination of the background, the usage of the instrumental profiles, the weighting algorithms and the different aspects of the sampling of the intensity pattern and the Fourier transforms are also given. The convergence and numerical stability of the procedure are also examined. By applying both the MWP and CMWP procedures for the determination of the microstructural parameters of ball milled Al-Mg alloys, the results obtained by the two different procedures were compared. The method was applied to nanocrystalline Cu and the planar fault density was determined. A special application of the CMWP procedure for systematically prepared ball milled fluorides is presented: for some of the samples an unusual X-ray optical interference effect was observed and the microstructural parameters have been determined by correcting for this effect.

By applying the MWP and CMWP methods, the microstructural properties of several different materials or groups of materials are determined and these properties are examined as a function of several mechanical or thermal treatments.

The most important results of my work are:

- The size profile [S1] and the size Fourier transform of coherently scattering domains with spherical or ellipsoidal crystallite shape and lognormal size distribution have been determined [S4, S5, S6, S8]. The expression of the Fourier transform supports the fast numerical evaluation.
- The method for applying the strain profile for XLPA based on the Wilkens model of dislocations and the model of average contrast factors have been worked out [S4, S6, S14].
- By using the theoretical size and strain profiles new methods have been developed for the extraction of microstructural parameters from X-ray measurements:
  - by fitting simultaneously the whole Fourier transforms or intensity profiles obtained by separation and instrumental deconvolution, (the method Multiple Whole Profile Fitting: MWP) [S4, S6], and
  - by the convolutional fitting (with the inclusion of the instrumental effect) of the whole diffraction spectrum, (the method of Convolutional Multiple Whole Profile Fitting: CMWP) [S14].

- A software package has been developed implementing the methods described in sections 4 and 5, which is available to the public [S4, S6, S14] through the web: <http://www.renyi.hu/mwp> and <http://www.renyi.hu/cmwp>.
- By using the MWP method I have shown that:
  - the dislocation density has the average value of  $10^{16}m^{-2}$  in severely deformed Ti, which is in accordance with electron microscopy investigations; and in this deformation stage mainly the slip systems  $\langle a \rangle$  and  $\langle c+a \rangle$  are activated [S11, S12, S22],
  - by applying ball milling and heat treatment of PbS (galena) samples, a systematic set of samples was produced and by evaluating the X-ray line profiles of these samples using the MWP method a map of microstructure was obtained. By comparing the microstructural parameters of samples from ancient cosmetics fabricated in the Egyptian Kingdom 3500 b.c. with the parameters of the systematically prepared samples I have shown that only gentle crushing and no heat treatment or heat treatment at a temperature of less than 300 °C was applied [S9] for the fabrication of the archaeological cosmetics.
- By using the CMWP method I have shown that:
  - in ball milled Al-Mg alloys the dislocation density as well as the average crystallite size shows a saturation after 2h of ball milling and the results obtained by the MWP and CMWP methods have been compared [S13, S16, S14],
  - in ball milled fluorides ( $MF_2$ , M=Ca,Ba,Cd,Sr) the presence of an X-ray optical interference effect can be observed which is present primarily if the average crystallite size of a larger portion of crystallites is about 5-10 nm or smaller [S17]. The X-ray optical interference effect means that the first few peak profiles become narrower than what would correspond to the domain size.
- I have shown that if the method of XLPA is carried out correctly, which means that the experiments are done with an angular resolution high enough and that the evaluation is based on correct microstructural models, then good correlation is observed between TEM and XLPA parameters. For example, in the case of nanocrystalline  $Si_3N_4$  particles the size distribution determined either by TEM or XLPA are in excellent agreement, cf. [S1]. In a large number of cases very good correlation was found between the microstructural parameters, especially the subgrain size, and size distribution, the dislocation density and dislocation types determined either by TEM or XLPA [S1–S22].

As the results of this work, a coherent set of methods has been developed which is suitable for the characterization of the microstructure of most different crystalline materials, e.g. metals, alloys, ceramic materials, minerals or polymers, in terms of the size and size distribution of crystallites or grains, the density, the distribution and character of dislocations and the density and type of planar defects.

## Own Publications

- [S1] Gubicza, J., Szépvölgyi, J., Mohai, I., Ribárik, G. and Ungár, T., The effect of heat-treatment on the grain-size of nanodisperse plasmathermal silicon nitride powder, *J. of Materials Science*, **35**, 3711 (2000)
- [S2] Gubicza, J., Ribárik, G., Bakonyi, I. and Ungár, T., Crystallite-size distribution and dislocation structure in nanocrystalline HfNi<sub>5</sub> determined by X-ray diffraction profile analysis, *J. Nanoscience & Nanotechnology*, **1**, 343–348, (2001)
- [S3] Gubicza, J., Ribárik, G., Goren-Muginstein, G. R., Rosen, A. R. and Ungár, T., The density and the character of dislocations in cubic and hexagonal polycrystals determined by X-ray diffraction, *Mat. Sci. and Eng. A*, **309–310**, 60–63 (2001)
- [S4] Ribárik, G., Ungár, T. and Gubicza, J., MWP-fit: a program for multiple whole-profile fitting of diffraction peak profiles by ab initio theoretical functions, *J. Appl. Cryst.*, **34**, 669–676 (2001)
- [S5] Ungár, T., Gubicza, J., Ribárik, G., Microstructure of carbon blacks determined by X-ray diffraction profile analysis, *Carbon*, **40**, 929–937, (2001)
- [S6] Ungár, T., Gubicza, J., Ribárik, G. and Borbély, A., Crystallite size-distribution and dislocation structure determined by diffraction profile analysis: Principles and practical application to cubic and hexagonal crystals, *J. Appl. Cryst.*, **34**, 298–310 (2001)
- [S7] Ungár, T., Gubicza, J., Ribárik, G. and Hanák, P., Dislocation structure and crystallite size distribution in plastically deformed metals determined by diffraction peak profile analysis, *J. Eng. Mat. and Technology (ASME)*, **124**, 2–6 (2002)
- [S8] Ungár, T., Gubicza, J., Ribárik, G., Pantea, C. and Zerda, T. W., Microstructure of carbon blacks determined by X-ray diffraction profile analysis, *Carbon*, **40**, 929–937 (2002)
- [S9] Ungár, T., Martinetto, P., Ribárik, G., Dooryhee, E., Walter, Ph. and Anne, M., Revealing the powdering methods of black makeup in Ancient Egypt by fitting microstructure based Fourier coefficients to the whole X-ray diffraction profiles of galena, *J. Appl. Phys.*, **91**, 2455–2465 (2002)

- [S10] Borbély, A., Dragomir, I. C., Ribárik, G., Ungár, T., Computer program ANIZC for the calculation of diffraction contrast factors of dislocations in elastically anisotropic cubic, hexagonal and trigonal crystals, *J. Appl. Cryst.*, **36**, 160–162, (2003)
- [S11] Gubicza, J., Dragomir, I. C., Ribárik, G., Baik, S. C., Zhu, Y. T., Valiev, R. Z. and Ungár, T., Dislocation structure and crystallite size-distribution in plastically deformed Ti determined by X-ray peak profile analysis, *Z. Metallkunde*, **94**, 1185–1188 (2003)
- [S12] Gubicza, J., Dragomir, I. C., Ribárik, G., Zhu, Y. T., Valiev, R. Z. and Ungár, T., Microstructure of severely deformed titanium from X-ray diffraction profile analysis, *Mat. Sci. Forum*, **414–415**, 229–234 (2003)
- [S13] Gubicza, J., Kassem, M., Ribárik, G. and Ungár, T., The evolution of the microstructure in mechanically alloyed Al-Mg studied by X-ray diffraction, *Mat. Sci. Eng. A*, **A372**, 115–122 (2004)
- [S14] Ribárik, G., Gubicza, J. and Ungár, T., Correlation between strength and microstructure of ball milled Al-Mg alloys determined by X-ray diffraction, *Mat. Sci. Eng. A*, **A387–389**, 343–347 (2004)
- [S15] Dragomir, I. C., Li, D. S., Castello-Branco, G. A., Garmestani, H., Snyder, R. L., Ribárik, G., Ungár, T., Evolution of dislocation density and character in hot rolled titanium determined by X-ray diffraction, *Materials Characterization*, **55**, 66–74 (2005)
- [S16] Révész, Á., Nagy, L., Ribárik, G., Kovács, Zs., Ungár, T., Lendvai, J., Microstructural evolution in mechanically alloyed nanocrystalline Al-20at.% Mg alloy, *J. of Metastable and Nanocrystalline Materials*, **24-25**, 149–152 (2005)
- [S17] Ribárik, G., Audebrand, N., Palancher, H., Ungár, T., Louër, D., Dislocations and crystallite size distributions in ball-milled nanocrystalline fluorides MF<sub>2</sub> (M = Ca, Sr, Ba, Cd) determined by X-ray diffraction-line-profile analysis, *J. Appl. Cryst.*, **38**, 912–926, (2005)
- [S18] Balogh, L., Ribárik, G. and Ungár, T., Stacking Faults and Twin Boundaries in fcc Crystals Determined by X-ray Diffraction Profile Analysis, *J. Appl. Phys.*, **100**, 023512 (2006)
- [S19] Dragomir, I. C., Li, D. S., Castello-Branco, G. A., Garmestani, H., Snyder, R. L., Ribárik, G. and Ungár, T., Microstructure evolution in hot rolled titanium determined by X-ray diffraction peak profile analysis, *Z. Kristallogr. Suppl.*, **23**, 99–104 (2006)
- [S20] Fátay, D., Spassov, T., Delchev, P., Ribárik, G., Révész, Á., Microstructural development in nanocrystalline MgH<sub>2</sub> during H-absorption/desorption cycling, *International Journal of Hydrogen Energy*, in press (2007)
- [S21] Ungár, T., Castelnau, O., Ribárik, G., Drakopoulos, M., Béchade, J. L., Chauveau, T., Snigirev, A., Snigireva, I., Schroer, C. and Bacroix, B., Grain to grain slip activity in plastically deformed

Zr determined by X-ray microdiffraction line profile analysis, *Acta Materialia*, **55**, 1117–1127 (2007)

[S22] Ungár, T., Glavicic, M. G., Balogh, L., Nyilas, K., Salem, A. A., Ribárik, G., Semiatin, S. L., The Use of X-Ray Diffraction to Determine Slip and Twinning Activity in Commercial-Purity (CP) Titanium, *Mat. Sci. Eng. A*, in press (2007)

[S23] Ribárik, G, Aifantis, E. C., Konstantinidis, A. and Ungár, T., *in preparation* (2007)

# Bibliography

- [1] Aitchinson, J. and Brown, J., *The Lognormal Distribution*, Cambridge University Press, Cambridge (1957)
- [2] Arley, N. and Buch, K. R., *Introduction to the Theory of Probability and Statistics*, New York - Wiley, (1950)
- [3] Balogh, L., Ribárik, G. and Ungár, T., *J. Appl. Phys.*, **100**, 023512 (2006)
- [4] Balogh et al., *in preparation* (2008)
- [5] Balzar, D., *J. Res. Natl. Inst. Stand. Technol.*, **98**, 321 (1993)
- [6] Berkum, J. G. M. van, *PhD thesis*, Delft University of Technology, The Netherlands (1994)
- [7] Bertaut, F. C. R., *Acad. Sci., Paris*, **228**, 187 (1949)
- [8] Borbély, A., Dragomir, I. C., Ribárik, G. and Ungár, T., *J. Appl. Cryst.*, **36**, 160–162 (2003)
- [9] Borbély, A., Driver, J. H. and Ungár, T., *Acta Mat.*, **48**, 2005–2016 (2000)
- [10] Borbély, A. and Groma, I., *Appl. Phys. Lett.*, **79**, 1772–1774 (2001)
- [11] Caglioti, G., Paoletti, A. and Ricci, F. P., *Nucl. Instrum.*, **3**, 223–234 (1958)
- [12] Cordier, P., Ungár, T., Zsoldos, L., Tichy, G., *Nature*, **428**, 837–840 (2004)
- [13] Csikor, F. F. and Groma, I., *Phys. Rev. B*, **70**, 064106 (2004)
- [14] Dong, Y. H. and Scardi, P., *J. Appl. Crystallogr.*, **33** (1999)
- [15] Dragomir, I. C., Li, D. S., Castello-Branco, G. A., Garmestani, H., Snyder, R. L., Ribárik, G., Ungár, T., *Materials Characterization*, **55**, 66–74 (2005)
- [16] Dragomir, I. C., Li, D. S., Castello-Branco, G. A., Garmestani, H., Snyder, R. L., Ribárik, G. and Ungár, T., *Z. Kristallogr. Suppl.*, **23**, 99–104 (2006)
- [17] Dragomir, I. C. and Ungár, T., *Powder Diffr. Journ.*, **17**, 104–111 (2002)
- [18] Essmann, U., Gösele, U. and Mughrabi, H., *Philos. Mag. A*, **44**, 405–426 (1981)

- [19] Fátay, D., Spassov, T., Delchev, P., Ribárik, G., Révész, Á., *International Journal of Hydrogen Energy*, in press (2007)
- [20] Gaál, I., *Acta Phys. Acad. Sci. Hung.* **33**, 411–418 (1973)
- [21] Gaál, I., *Dissertation to the Hungarian Academy of Sciences*, Budapest, Hungary (1976)
- [22] Gaál, I., *Proc. 5th Riso Int. Symp. Metall. Mater. Sci.*, edited by N. H. ANDERSEN, M. ELDRUP, N. HANSEN, D. JUUL JENSEN, T. LEFFERS, H. LIFHOLT, O. B. PEDERSEN B. N. SINGH, pp. 249-254. Riso Natl Lab., Roskilde, Denmark (1984)
- [23] Groma, I., *Phys. Rev. B*, **57**, 7535–7542 (1998)
- [24] Groma, I. and Monnet, G., *Journal of Applied Cryst.*, **35**, 589-593 (2002)
- [25] Groma, I., *DSc thesis*, Eötvös Loránd University, Budapest, Hungary (2003)
- [26] Gubicza, J., Dragomir, I. C., Ribárik, G., Baik, S. C., Zhu, Y. T., Valiev, R. Z. and Ungár, T., *Z. Metallkunde*, **94**, 1185–1188 (2003)
- [27] Gubicza, J., Dragomir, I. C., Ribárik, G., Zhu, Y. T., Valiev, R. Z. and Ungár, T., *Mat. Sci. Forum*, **414–415**, 229–234 (2003)
- [28] Gubicza, J., Juhász, A., Lendvai, J., *J. Mater. Res.*, **11**, 2964 (1996)
- [29] Gubicza, J., Kassem, M., Ribárik, G. and Ungár, T., *Mat. Sci. Eng. A*, **A372**, 115–122 (2004)
- [30] Gubicza, J., Ribárik, G., Bakonyi, I. and Ungár, T., *J. Nanoscience & Nanotechnology*, **1**, 343–348, (2001)
- [31] Gubicza, J., Ribárik, G., Goren-Muginstein, G. R., Rosen, A. R. and Ungár, T., *Mat. Sci. and Eng. A*, **309–310**, 60–63 (2001)
- [32] Gubicza, J., Rozlosnik, N., Juhász, A., *J. Mater. Sci. Lett.*, **16**, 1904 (1997)
- [33] Gubicza, J., Szépvölgyi, J., Mohai, I., Ribárik, G. and Ungár, T., *J. of Materials Science*, **35**, 3711 (2000)
- [34] Guerrero-Paz, J. and Jaramillo-Vigueras, D., *Nanostruct. Mater.*, **11**, 1123–1132 (1999)
- [35] Guinier, A., *X-ray diffraction*, Freeman and Co., San Francisco, CA (1963)
- [36] Hall, E. O., *Proc. Phys. Soc., Ser. B*, **Vol. 64**, 747–753, (1951)
- [37] Hecker, M., Thiele, E. and Holste, C., *Mat. Sci. Eng. A*, **234–236**, 806–809 (1997)
- [38] Hinds, W. C., *Aerosol Technology: Properties, Behavior and Measurement of Airborne Particles*, Wiley, New York (1982)

- [39] Janot, R. and Guerard, D., *Prog. Mater. Sci.*, **50**, 1–92 (2005)
- [40] Kamminga, J. D. and Delhez, R., *J. Appl. Cryst.*, **33**, 1122–1127 (2000)
- [41] Krill, C. E. and Birringer, R., *Philos. Mag. A*, **77**, 621–640 (1998)
- [42] Krivoglaz, M. A., *Theory of X-ray and Thermal Neutron Scattering by Real Crystals*, Plenum Press New York (1969)
- [43] Krivoglaz, M. A. and Ryaboshapka, K. P., *Fizika Metall.*, **15**, No. 1, 18 (1963)
- [44] Langford, J. I. and Wilson, A. J. C., *J. Appl. Cryst.*, **11**, 102–113 (1978)
- [45] Langford, J. I., Louër, D. and Scardi, P., *J. Appl. Cryst.*, **33**, 964–974 (2000)
- [46] Leoni, M. and Scardi, P., *J. Appl. Cryst.*, **37**, 629–634 (2004)
- [47] Levenberg, K., *Quart. Appl. Math.*, **2**, 164–168 (1944)
- [48] Louër, D. and Audebrand, N., *Adv. X-ray Anal.*, **41**, 556–565 (1999)
- [49] Marquardt, D. W., *SIAM J. Appl. Math.*, **11**, 431–441 (1963)
- [50] Martinetto, P., Anne, M., Dooryhée, E., Tsoucaris, G. and Walter, Ph., *Radiation in Art and Archeometry*, edited by D. Creagh and D. Bradley, Elsevier Science BV, Prague (2000)
- [51] Martinetto, P., Castaing, J., Walter, P., Penhoud, P. and Veysiere, P., *J. Mater. Res.*, **17**, 1601–1611 (2002)
- [52] Mughrabi H., Ungar T., Kienle W., Wilkens M., *Phil. Mag.*, **53**, 793 (1986)
- [53] Nelson, J. B., Riley, D. P., *Proc. Phys. Soc. London*, **57**, 160 (1945)
- [54] Nusinovici, J. and Rehfeldt-Osierski, A., *Collected Abstracts, IUCr Powder Diffraction Satellite Meeting, Toulouse, France*, 315–316 (1990)
- [55] Pál, F., Tóth, K., Pungor, E., Farkas-Jahnke, M., Ebel, H. and Ebel, M. F., *Anal. Chim Acta*, **180**, 313–321 (1986)
- [56] Paton, N. E. and Backofen, W. A., *Metallurgical Trans.*, **1**, 2839–2847 (1970)
- [57] Pederson, D. O. and Brewer, J. A., *Phys. Rev. B*, **16**, 4546–4550 (1977)
- [58] Petch, N.J., *J. Iron and Steel Institute*, **May**, 25–28 (1953)
- [59] Pool, D. M. and Axon, H. J., *J. Inst. Met.*, **80**, 599 (1952)
- [60] Rác, B., Mulas, G., Csongrádi, A., Loki, K. and Molnár, A., *Appl. Catal. A*, **282**, 255–265 (2005)

- [61] Rafaja, D., Klemm, V., Schreiber, G., Knapp, M. and Kužel, R., *J. Appl. Cryst.*, **37**, 613–620 (2004)
- [62] Révész, Á., Nagy, L., Ribárik, G., Kovács, Zs., Ungár, T., Lendvai, J., *J. of Metastable and Nanocrystalline Materials*, **24-25**, 149–152 (2005)
- [63] Ribárik, G., Aifantis, E. C., Konstantinidis, A. and Ungár, T., *in preparation* (2007)
- [64] Ribárik, G., Audebrand, N., Palancher, H., Ungár, T., Louër, D., *J. Appl. Cryst.*, **38**, 912–926, (2005)
- [65] Ribárik, G., Gubicza, J. and Ungár, T., *Mat. Sci. Eng. A*, **A387–389**, 343–347 (2004)
- [66] Ribárik, G., Ungár, T. and Gubicza, J., *J. Appl. Cryst.*, **34**, 669–676 (2001)
- [67] Scardi, P. and Leoni, M., *J. Appl. Cryst.*, **32**, 671–682 (1999)
- [68] Scardi, P. and Leoni, M., *Acta Cryst.*, **A58**, 190–200 (2002)
- [69] Scherrer, P., *Göttinger Nachrichten*; R. Zsigmondy, *Kolloidchemie* (3rd Ed. 1920), pp. 394 (1918)
- [70] Somogyvári Z., Sváb, E., Mészáros, Gy., Krezhov, K., Konstantinov, P., Ungár, T. and Gubicza, J., *Mat. Sci. Forum*, **378-381**, 771-776 (2001)
- [71] Sprackling, M. T., *The Plastic Deformation of Simple Ionic Crystals*, Academic Press, London (1976)
- [72] Stokes, A. R., *Proc. Phys. Soc.*, **61**, 382–393 (1948)
- [73] Stokes, A. R. and Wilson, A. J. C., *Proc. Phys. Soc.*, **56**, 174–180 (1944)
- [74] Terwilliger, Ch. D. and Chiang, Y. M., *Acta Metall. Mater.*, **43**, 319–328 (1995)
- [75] Treacy, M. M. J., Newsam J. M., and Deem, M. W., *Proc. R. Soc. London*, Ser. A **433**, 499 (1991)
- [76] Ungár, T., Alexandrov, I. and Hanák, P., *Proc. Int. Conf. Severe Plastic Deformation*, Moscow, 1999, KLUWER A. P. (2000)
- [77] Ungár, T. and Borbély, A., *Appl. Phys. Lett.*, **69**, 3173–3175 (1996)
- [78] Ungár, T., Castelnau, O., Ribárik, G., Drakopoulos, M., Béchade, J. L., Chauveau, T., Snigirev, A., Snigireva, I., Schroer, C. and Bacroix, B., *Acta Materialia*, **55**, 1117–1127 (2007)
- [79] Ungár, T., Dragomir, I. C., Louër, D. and Audebrand, N., *J. Phys. Chem. Solids*, **62**, 1935–1941 (2001)

- [80] Ungár, T., Dragomir, I. C., Révész, Á. and Borbély, A., *J. Appl. Cryst.*, **32**, 992–1002 (1999)
- [81] Ungár, T., Glavicic, M. G., Balogh, L., Nyilas, K., Salem, A. A., Ribárik, G., Semiatin, S. L., *Mat. Sci. Eng. A*, in press (2007)
- [82] Ungár, T., Gubicza, J., Ribárik, G., *Carbon*, **40**, 929–937, (2001)
- [83] Ungár, T., Gubicza, J., Ribárik, G. and Borbély, A., *J. Appl. Cryst.*, **34**, 298–310 (2001)
- [84] Ungár, T., Gubicza, J., Ribárik, G. and Hanák, P., *J. Eng. Mat. and Technology (ASME)*, **124**, 2–6 (2002)
- [85] Ungár, T., Gubicza, J., Ribárik, G., Pantea, C. and Zerda, T. W., *Carbon*, **40**, 929–937 (2002)
- [86] Ungár, T., Martinetto, P., Ribárik, G., Dooryhee, E., Walter, Ph. and Anne, M., *J. Appl. Phys.*, **91**, 2455–2465 (2002)
- [87] Ungár, T., Mughrabi, H., Rönnpagel, D. and Wilkens, M., *Acta Met.*, **32**, 333–341 (1984)
- [88] Ungár, T., Ott, S., Sanders, P. G., Borbély, A. and Weertman, J. R., *Acta Mater.*, **10**, 3693 (1998)
- [89] Ungár, T. and Tichy, G., *Phys. Status Solidi. A*, **171**, 425–434 (1999)
- [90] Ungár, T., Tichy, G., Gubicza, J., Hellmig, R. J., *J. Powder Diffr.*, **20**, 366 (2005)
- [91] Valiev, R. Z., Kozlov, E. V., Ivanov, Yu., F., Lian, J., Nazarov, A. A. and Baudalet, B., *Acta Metall. Mater.*, **42**, 2467–2476 (1994)
- [92] Wakai, F. and Aldinger, F., *Acta Mater.*, **51**, 641–652 (2003)
- [93] Walter, Ph., Martinetto, P., Tsoucaris, G., Bréniaux, R., Lefebvre, M-A., Richard, G., Talabot, J. and Dooryhée, E., *Nature*, **397**, 483–484 (1999)
- [94] Warren, B. E., *Progr. Metal Phys.*, **8**, 147–202 (1959)
- [95] Warren, B. E., *X-ray Diffraction*, Reading, Addison-Wesley, MA (1969)
- [96] Warren, B. E. and Averbach, B. L., *J. Appl. Phys.*, **23**, 497 (1952)
- [97] Warren, B. E. and Bodenstein, P., *Acta Cryst.*, **18**, 282 (1965)
- [98] Wilkens, M., *Theoretical aspects of kinematical X-ray diffraction profiles from crystals containing dislocation distributions*, Fundamental Aspects of Dislocation Theory, edited by J. A. Simmons, R. de Wit and R. Bullough., Vol. II, pp. 1195-1221, Nat. Bur. Stand. (US) Spec. Publ. No. 317., Washington, DC, USA (1970)
- [99] Wilkens, M., *Proc. Int. Conf. Strength Met. Alloys (ICSMA 8)*, Tampere, Finland, 1988, eds. Kettunen, P. O., Lepistö, T. K., Lehtonen, M. E., Pergamon Press, 47–152 (1988)

- [100] Williamson, G. K. and Hall, W. H., *Acta metall.*, **1**, 22–31 (1953)
- [101] Wilson, A. J. C., *X-ray Optics*, Methuen, London (1962)
- [102] Winther, G., Huang, X., Godfrey A. and Hansen N., *Acta Materialia*, **52**, 4437–4446 (2004)
- [103] Yao, Y. and Thölén, A., *Mater. Charact.*, **44**, 441–452 (2000)
- [104] York, B. R., *Adv. X-ray Anal.*, **41**, 544–555 (1999)
- [105] Zhu, Y. T., Huang, J. Y., Gubicza, J., Ungár, T., Wang, Y. M., Ma, E., Valiev, R. Z., *J. Mat. Res.*, **18**, 1908–1917 (2003)

# Acknowledgements

I express my deep gratitude to my supervisor, *Prof. Tamás Ungár* for introducing, encouraging and guiding me in the field of materials science. I am in his debt for his care and boundless patience in revising this manuscript.

I'm grateful to my family, first of all to my wife, Orsolya Ribárik for her help in typography and to my son, Balázs Ribárik for his patience and letting me work.

I would like to thank for the fruitful cooperation to the co-authors of our common papers, especially to Prof. Tamás Ungár, Dr. Jenő Gubicza, Dr. Ádám Révész, Dr. Iulianna Dragomir and Mr. Levente Balogh.

Thanks are due to my colleagues, especially to Prof. István Groma, Dr. András Borbély, Dr. Erhard Schafler, Mr. Michael Kerber, Dr. Avraam Konstantinidis and Prof. E.C. Aifantis for the inspiring discussions.

I would like to thank for the careful reading of the thesis to Dr. Jenő Gubicza and Mr. Michael Kerber.

I am especially grateful to Prof. János Lendvai for the opportunity to have been able to work at the Department of Materials Physics of the Eötvös Loránd University.

## Short summary

Most of the physical properties of crystalline materials are fundamentally determined by the microstructure. Electron microscopy is an important method for the visualization of the microstructure. The most important fundamental microstructural properties are the type, density and distribution of crystal defects and the grain or crystallite structure. X-ray line profile analysis (XLPA) is one of the most important and powerful alternative methods besides electron microscopy for the characterization of microstructures. This method gives information about the following basic microstructural properties: (i) the size and distribution of crystallites, (ii) the shape anisotropy of crystallites, (iii) the density, character and distribution of dislocations and (iv) the density and type of stacking faults and twin boundaries. This dissertation presents the most important theoretical models of the microstructure according to the literature, my results related to the development of these models, the most important methods of XLPA: the classical ones and some of the most recent methods of literature. The most important part of my work is the development and implementation of new XLPA methods, which are based on the modeling of the physical properties of the different crystal defects. By comparing the so obtained model based line profiles with the measured ones the methods give the microstructural parameters of the investigated materials. By applying these methods the microstructural properties of several different materials or groups of materials are determined and these properties are examined as a function of several mechanical or thermal treatments.

The most important new scientific results of my work are: (i) I have determined the size profile [S1] and the size Fourier transform of coherently scattering domains with spherical or ellipsoidal crystallite shape and lognormal size distribution [S4, S5, S6, S8]. (ii) I elaborated the method for applying the strain profile for XLPA based on the Wilkens model of dislocations and the model of average contrast factors [S4, S6, S14]. (iii) I developed two new methods by using the theoretical size and strain profiles for the extraction of microstructural parameters from X-ray measurements: (a) by fitting simultaneously the whole Fourier transforms or intensity profiles, (the method Multiple Whole Profile Fitting: MWP) [S4, S6], and (b) by the convolutional fitting of the whole diffraction spectrum, (the method of Convolutional Multiple Whole Profile Fitting: CMWP) [S14]. (iv) I worked out a software package for these methods described which is publicly available [S4, S6, S14]. (v) By using the MWP method I have shown that: (a) the dislocation density has the average value of  $10^{16}m^{-2}$  in severely deformed Ti, which is in accordance with electron microscopy investigations; and in this deformation stage mainly the slip systems  $\langle a \rangle$  and  $\langle c+a \rangle$  are activated [S11, S12, S22], (b) by applying ball milling and heat treatment of PbS (galena) samples, a systematic set of samples has been produced and by evaluating the X-ray line profiles of these samples using the MWP method a map of microstructure has been obtained. By comparing the microstructural parameters of samples from ancient cosmetics fabricated in the Egyptian Kingdom 3500 b.c. with the parameters of the systematically prepared samples I have shown that only gentle crushing and no heat treatment or heat treatment at a temperature of less than 300 °C was applied [S9] for the fabrication of the archaeological cosmetics. (vi) By using the CMWP method I have shown that: (a) in ball milled Al-Mg alloys the dislocation density as well as the average crystallite size shows a saturation after 2h of ball milling and the results obtained by the MWP and CMWP methods have been compared [S13, S16, S14], (b) in ball milled fluorides ( $MF_2$ , M=Ca,Ba,Cd,Sr) the presence of an X-ray optical interference effect can be observed which is present primarily if the average crystallite size of a larger portion of crystallites is about 5-10 nm or smaller [S17]. (vii) I have shown that in nanocrystalline  $Si_3N_4$  particles the size distribution determined either by TEM or XLPA are in excellent agreement, cf. [S1]. In a large number of cases very good correlation was found between the microstructural parameters, especially the subgrain size, and size distribution, the dislocation density and dislocation types determined either by TEM or XLPA [S1–S22].

As the results of this work, a coherent set of methods has been developed which is suitable for the characterization of the microstructure of most different crystalline materials.

## Rövid összefoglalás

Kristályos anyagok számos fizikai tulajdonságát alapvetően meghatározza a mikroszerkezet. A mikroszerkezet szemléltetésének fontos módszere az elektronmikroszkópia. A legalapvetőbb mikroszerkezeti tulajdonságok a kristályhibák típusa, sűrűsége és eloszlása valamint a szemcse-, illetve krisztallit szerkezet. Az elektronmikroszkópia mellett az egyik legfontosabb alternatív módszer a röntgen vonalprofil analízis (RVPA). Ez a módszer alapvetően a következő mikroszerkezeti tulajdonságokról ad felvilágosítást: (i) krisztallitok méretéről és méreteloszlásáról, (ii) krisztallitok alak anizotrópiájáról, (iii) diszlokációk sűrűségéről, típusáról és eloszlásáról, valamint (iv) rétegződési hibák illetve iker határok sűrűségéről és típusáról. A disszertációban bemutatom a mikroszerkezet legfontosabb irodalomban fellelhető modelljeit, illetve eredményeimet melyek ezek továbbfejlesztésével kapcsolatosak, ismertetem a RVPA fontosabb módszereit a klasszikusaktól kezdve a legújabb irodalomban fellelhető módszerekig. Munkám legjelentősebb része a RVPA olyan módszereinek a kifejlesztése, amelyek a különböző kristályhibák fizikai tulajdonságai alapján modellezik a röntgendiffrakciós vonalprofilokat. Ezeknek a modellezett vonalprofiloknak a mérésekkel való összevetéséből, a kifejlesztett módszerek segítségével megkaphatjuk a vizsgált anyag mikroszerkezeti paramétereit. A kidolgozott módszerek alkalmazásával meghatározom számos különböző anyag illetve anyagcsalád mikroszerkezeti tulajdonságait, valamint azt, hogy ezek hogyan változnak meg különböző mechanikai vagy termikus kezelések hatására.

Ennek a munkának a során kapott főbb új tudományos eredményeim a következők: (i) Meghatároztam gömb- [S1], illetve forgási ellipszoid alakú, lognormális méreteloszlású koherens domének méretprofil függvényeit és azok Fourier transzformáltját [S4, S5, S6, S8]. (ii) Kidolgoztam a deformációs profil felhasználásának módszerét a diszlokációk Wilkens-féle modellje és az átlagos kontraszt faktorok modellje alapján [S4, S6, S14]. (iii) Az elméleti méret- és deformációs profilok alapján módszereket dolgoztam ki a mikroszerkezet paramétereinek meghatározására röntgendiffrakciós mérésekből: (a) a teljes Fourier transzformáltak, illetve teljes intenzitásprofilok együttes illesztésével (Multiple Whole Profile Fitting: MWP) [S4, S6], illetve (b) a teljes intenzitás spektrum konvolúciós illesztésével (Convolutional Multiple Whole Profile Fitting: CMWP) [S14]. (iv) Bárki számára elérhető programcsomagot fejlesztettem ki ezekhez a módszerekhez [S4, S6, S14]. (v) Az MWP eljárás alapján megmutattam, hogy: (a) erőteljesen alakított Ti-ban a diszlokációsűrűség  $10^{16} m^{-2}$  átlagos értéket ér el, összhangban az elektronmikroszkópos vizsgálatokkal; továbbá, hogy ilyen deformált állapotban döntően a  $\langle a \rangle$  és  $\langle c+a \rangle$  típusú csúszási rendszerek dominálnak [S11, S12, S22], (b) a PbS (galenit) őrlésével és hőkezelésével készült mikroszerkezeti állapottérkép alapján megállapítottam, hogy az ie. 3500 Egyiptomi Királyságokban használt kozmetikumok készítésekor csupán rövid idejű őrlést és 300 °C-nál nem magasabb hőmérsékletű hőkezeléseket alkalmaztak [S9]. (vi) A CMWP eljárás alapján megmutattam, hogy: (a) golyós malomban őrlött Al-Mg ötvözetben mind a diszlokáció sűrűség, mind pedig a szemcseméret 2 óra őrlés után telítődést mutat, továbbá az MWP és CMWP módszerekkel kapott eredményeket összehasonlítottam [S13, S16, S14], (b) golyós malomban őrlött alkáliföldfém fluoridokban kimutattam egy újszerű röntgen optikai interferencia effektus fellépését, amely elsősorban akkor jelenik meg, ha a méreteloszlás jelentős hányadában a szemcseméret 5-10 nm, vagy annál kisebb [S17]. (vii) Nanokristályos  $Si_3N_4$  részecskéinek TEM és röntgen méreteloszlására igen jó egyezést kaptam [S1]. Számos esetben igazolódott, hogy az elektronmikroszkópos szubszemcse méret, diszlokációsűrűség, valamint diszlokáció típus kitűnően egyezik a vonalprofil analízis módszerével nyert értékekkel [S1–S22].

Munkám eredményeképpen előállt egy olyan koherens módszer együttes, amely alkalmas a legkülönbözőbb kristályos anyagok, nevezetesen, fémek, ötvözetek, kerámiák, kőzetek, illetve polimerek mikroszerkezetének jellemezésére a krisztallit és szemcseméret, a diszlokáció sűrűség, eloszlás és típus, illetve a rétegződési hibák alapján.